ulm university universität ulm

Annual Report 2006

Institute of Optoelectronics

Ulm University | Institute of Optoelectronics | Annual Report 2006

Cover photo:
Optoelectronic transceiver chip for bidirectional optical data transmission over a graded-index multimode fiber, see the article on p. 25.

Contents

1: Ferdinand Scholz
2: Peter Unger
3: Rudolf Rösch
4: Frank Demaria
5: Josef Theisz
6: Hendrik Roscher
7: Sükran Kilic
8: Andrea Kroner
9: Dietmar Wahl
10: Frank Lipski
11: Christine Bunk
12: Georgi Stareev
13: Hildegard Mack
14: Jürgen Mähnß
15: Gerlinde Meixner
16: Abdel-Sattar Gadallah
17: Martin Stach
18: Fernando Rinaldi
19: Thomas Wunderer
20: Rainer Michalzik
21: Ivan Safanov
22: Sarad B. Thapa
23: Michael C. Riedl
24: Wolfgang Schwarz
25: Peter Brückner
26: Ihab Kardosh
27: Steffen Lorch
28: Joachim Hertkorn
29: Rainer Blood

Missing in the picture:

Karl J. Ebeling, Susanne Menzel

Institute of Optoelectronics
Ulm University

Albert-Einstein-Allee 45, 89081 Ulm, Germany
URL: http://www.uni-ulm.de/opto
Fax: +49–731/50–260 49
Phone: +49–731/50–

Head of Department

Prof. Dr.	Peter Unger	–2 60 54	peter.unger@uni-ulm.de

Deputy Head

Prof. Dr.	Ferdinand Scholz	–2 60 52	ferdinand.scholz@uni-ulm.de

President of the University of Ulm

Prof. Dr.	Karl Joachim Ebeling	–2 60 51	karl.ebeling@uni-ulm.de

Senior Research Assistant

Dr.-Ing.	Rainer Michalzik	–2 60 48	rainer.michalzik@uni-ulm.de

Cleanroom Management

Dr.-Ing.	Jürgen Mähnß	–2 60 53	juergen.maehnss@uni-ulm.de

Secretaries

	Christine Bunk	–2 60 50	christine.bunk@uni-ulm.de
	Sükran Kilic	–2 60 59	suekran.kilic@uni-ulm.de
	Hildegard Mack	–2 60 59	hildegard.mack@uni-ulm.de

Guest Scientist

Dr.	Daniel Hofstetter	–2 60 51	daniel.hofstetter@uni-ulm.de
Electron. Eng.	Ivan M. Safanov	–2 60 39	ivan.safonov@uni-ulm.de

Research Staff

Dipl.-Ing.	Peter Brückner	–2 60 35	peter.brueckner@uni-ulm.de
Dipl.-Phys.	Frank Demaria	–2 60 46	frank.demaria@uni-ulm.de
M.Sc.	Abdel-Sattar Gadallah	–2 60 36	abdel-sattar.gadallah@uni-ulm.de
Dipl.-Ing.	Philipp Gerlach*	–2 60 37	philipp.gerlach@uni-ulm.de
Dipl.-Ing.	Joachim Hertkorn	–2 61 95	joachim.hertkorn@uni-ulm.de
Dipl.-Ing.	Ihab Kardosh	–2 60 36	ihab.kardosh@uni-ulm.de
Dipl.-Ing.	Andrea Kroner	–2 60 38	andrea.kroner@uni-ulm.de
Dipl.-Phys.	Frank Lipski	–2 60 35	frank.lipski@uni-ulm.de
Dr.-Ing.	Steffen Lorch	–2 60 39	steffen.lorch@uni-ulm.de
Dipl.-Ing.	Barbara Neubert*	–2 64 54	barbara.neubert@uni-ulm.de
Dipl.-Phys.	Johannes M. Ostermann*	–2 60 38	johannes-michael.ostermann@uni-ulm.de
Dipl.-Ing.	Michael C. Riedl	–2 60 36	michael.riedl@uni-ulm.de
Dipl.-Phys.	Fernando Rinaldi	–2 60 46	fernando.rinaldi@uni-ulm.de
Dipl.-Ing.	Hendrik Roscher	–2 60 44	hendrik.roscher@uni-ulm.de
Dipl.-Ing.	Wolfgang Schwarz	–2 60 38	wolfgang.schwarz@uni-ulm.de
Dipl.-Ing.	Martin Stach	–2 60 37	martin.stach@uni-ulm.de

Dr.-Ing.	Georgi Stareev	–2 64 53	georgi.stareev@uni-ulm.de
Dipl.-Ing.	Sarad Bahadur Thapa	–2 61 95	sarad.thapa@uni-ulm.de
Dipl.-Phys.	Dietmar Wahl	–2 60 37	dietmar.wahl@uni-ulm.de
Dipl.-Ing.	Thomas Wunderer	–2 64 54	thomas.wunderer@uni-ulm.de

Technical Staff

Rainer Blood	–2 60 44	rainer.blood@uni-ulm.de
Gerlinde Meixner	–2 60 41	gerlinde.meixner@uni-ulm.de
Susanne Menzel	–2 60 41	susanne.menzel@uni-ulm.de
Josef Theisz	–2 60 30	josef.theisz@uni-ulm.de

* Member has left the department meanwhile

Preface

During 2006, the research activities of the Institute of Optoelectronics have been continuing in the areas of optical interconnect systems, vertical-cavity surface-emitting lasers, GaN-based electronic and optoelectronic devices, optically pumped semiconductor disk lasers, and high-power semiconductor amplifiers. The VCSELs and Optical Interconnects Group headed by Rainer Michalzik has demonstrated, amongst others, AlGaAs-based VCSELs with emission wavelengths as low as 720 nm, high-performance 850 nm single-mode VCSELs, miniaturized transceiver chips for bidirectional optical data transmission over graded-index multimode fiber, as well as novel schemes for multilevel digital signal generation and optical trap-based particle sorting, both using densely spaced VCSEL configurations. In the GaN Group headed by Ferdinand Scholz, the work on semipolar LEDs has attracted much attention, as bright light generation from facet quantum well LEDs could be demonstrated. Moreover, a new project pushed the research activities on free-standing GaN wafers: Nearly full 2-inch GaN wafers with thicknesses of about 1 mm could be grown by hydride vapor phase epitaxy. In the High-Power Semiconductor Laser Group headed by Peter Unger, a continuous output power of 13.2 W has been achieved with a semiconductor disk laser having an optical-to-optical conversion efficiency of more than 50 %.

A major event of the last year was the DGKK workshop on III-V epitaxy where about 130 scientists shared their latest results, presented in more than 40 talks. The participation of 24 companies in the accompanying industrial exhibition underlined once more the strong importance of research of the Institute for the development of future daily life optoelectronic devices. Thanks to the cooperation of our faculty, the scientific parts of the workshop could make use of the convenient lecture halls of the Universität West, complemented by a workshop dinner in the Stadthaus near the Ulmer Münster cathedral, generously sponsored by the participating companies.

Four members of the Institute, namely Martin Peschke, Brem Kumar Saravanan, Frank Habel, and Steffen Lorch received their Ph.D. degrees. Furthermore, 4 Diploma or Master Theses and 3 Semester Projects have been carried out in 2006. The Institute further intensified the close collaboration with industrial partners. We also appreciate the financial support of national and European research organizations, which contribute the major part of our funding. Numerous publications at international conferences and a large number of articles in respected journals document the strong research activities of the Institute. A detailed list can be found at the end of this report.

Peter Unger Ulm, March 2007

High-Radiance Optically Pumped Semiconductor Disk Lasers

Frank Demaria and Michael Riedl

We report on high-power operation of an optically pumped external-cavity semiconductor disk laser. 13.2 W optical output power at 970 nm has been achieved in a double-pass pump configuration. The laser Bragg mirror was designed to provide not only high reflectivity for the laser wavelenth but also for the pumping beam. A proper layer structure which supports standing-wave patterns with a node near the semiconductor surface reduces cavity losses and degradation. Compensation of the compressive strain, introduced by the six InGaAs quantum wells is achieved by GaAsP layers. The influence of the cavity geometry and the pump spot size on the laser beam quality and optical output power is investigated. An extention of the well-known equation is presented and compared to experimental results.

1. Introduction

Optically pumped semiconductor disk lasers with external cavities are devices with outstanding properties. Unlike commonly used semiconductor lasers, good lateral mode control is achieved by the external resonator, which can be built up with a geometry that supports fundamental mode operation. In comparison with compact single-mode electrically pumped diode lasers having integrated plane mirrors like vertical-cavity surface-emitting lasers or edge emitters, the need for good spatial beam quality is no stringent limitation of the active emission area and the corresponding maximum output power. Hence, the diameter of the pumped area can be scaled up to several hundreds of micrometers and multi-watt diffraction-limited operation becomes possible. For pump-spot sizes ranging between 500 and 900 µm diameter, 30 W of optical output power at 980 nm already has been demonstrated [1]. Of course, the pump-spot diameter has to be considered in the external cavity setup, with respect to its length, mirror curvature, and the expected beam quality. In Section 2, a simplified model and an analytic equation, that describes the functional dependency between these values, will be given as well as the results of an experimental investigation.

For large emission areas, cooling becomes more and more deteriorated, due to the reduced heat-spreading effect. This plays an important role, because the optical output power of semiconductor disk lasers usually is limited by thermal roll-over. Thus, high conversion efficiencies in order to minimize heat generation as well as a sophisticated thermal management becomes crucial. For that, CVD-diamond heat spreaders can be utilized [1]. Other approaches base upon relatively expensive transparent mono-crystal diamond heat spreaders in an intra-cavity [2] or end-pump configuration [3]. In contrast to that,

we investigated the potential for high-power laser operation, without any high thermal conductivity diamond heatspreaders or intra-cavity cooling, but with quite inexpensive copper heatsinks. The characteristics that have been achieved in that way are presented in Section 3.

2. Beam-Parameter Dependency on the Cavity Geometry

2.1 Theory

Since the thickness of the laser chip is several orders of magnitude smaller than the length of the resonator, the plane Bragg reflector of the laser chip and the external mirror establish a cavity that comes close to an ideal hemispherical cavity, whose geometry is given by its length L_c and the mirror radius of curvature R_c. Stable resonance condition implies that the effective radius of curvature of the beam phase fronts are identical with the mirror radius, located at $z = L_\mathrm{c}$, while its waist is located at the same position $z = 0$ as the Bragg mirror. According to Siegman [4], for any nonideal optical beam, travelling in the z-direction, having its beam waist located at $z = 0$, the effective radius of curvature is given by

$$R(z) = z + \frac{z_\mathrm{R}^2}{z}, \tag{1}$$

which is the same as for the ideal TEM_{00} Gaussian beam. The deviation from the ideal beam and the contribution of higher-order modes is taken into account by the beam-quality factor $M^2 \geq 1$, which can be experimentally determined [5], and the subsequent definition of the Rayleigh range

$$z_\mathrm{R} = \frac{4\pi\sigma_0^2}{M^2\lambda}. \tag{2}$$

The spatial variance σ_0 at the beam waist therein can be related to the beam diameter ω_0 by $4\sigma_0 = \omega_0$. Hence, the relation between the real-beam diameter on the chip, the beam-quality factor, and the cavity geometry is given by

$$\omega_0^2 = \frac{4M^2\lambda}{\pi}\sqrt{L_\mathrm{c}(R_\mathrm{c} - L_\mathrm{c})}. \tag{3}$$

For the boundary case of the ideal TEM_{00} Gaussian beam with $M^2 = 1$, this relation is well-known and reported by Kuznetsov *et al.* [6]. However, the restriction to the lowest order Gaussian mode can be misleading. Actually, higher-order modes can be observed for most resonator geometries, hence there is no stringent physical boundary condition, concerning the beam quality and existence of higher-order modes. On top of Fig. 1, the mode diameter on the chip, calculated by (3), for a mirror radius of 100 mm and different M^2-parameters is shown. Furthermore, another meaningful formulation is given by

$$M^2 = \frac{\pi\omega_0^2}{4\lambda\sqrt{L_\mathrm{c}(R_\mathrm{c} - L_\mathrm{c})}}, \tag{4}$$

for which the graphs for different values of ω_0^2 are shown at the bottom of Fig. 1. If ω_0 and R_c are considered to be constants, determined by the spot size of the pump beam on the

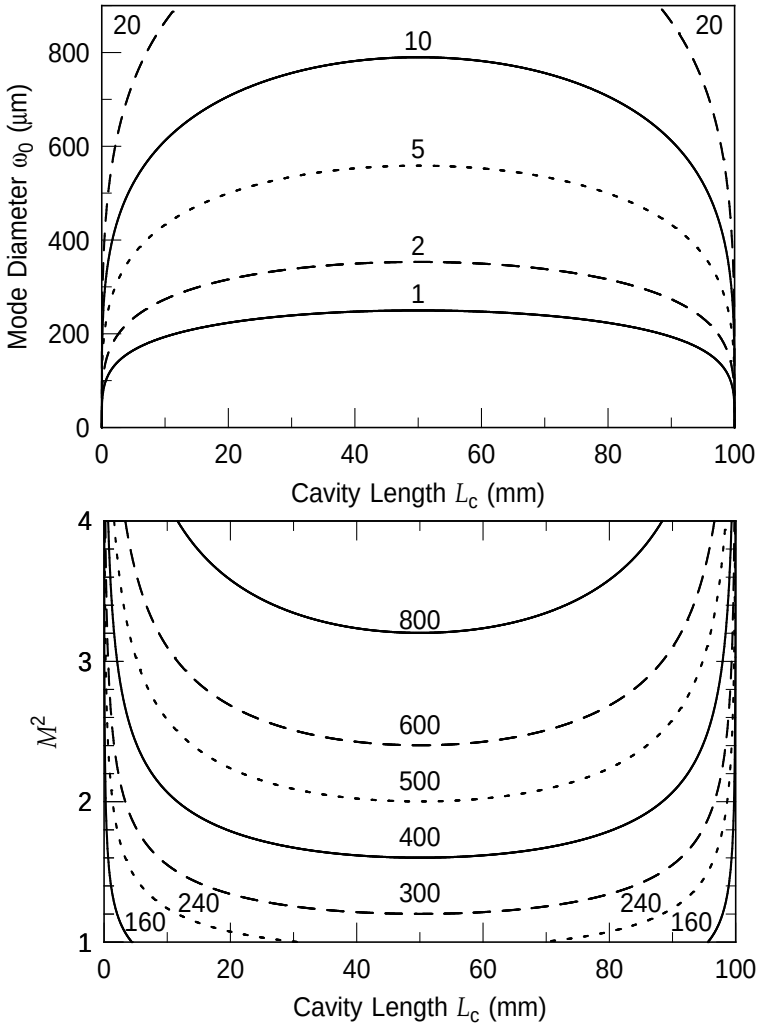

Fig. 1: Calculated function of beam-waist diameter ω_0 and the diffraction-number M^2 on the cavity length for a 100 mm outcoupling mirror radius and a wavelength of 980 nm. On top, the beam-waist diameter at the laser-chip position is given for beams with different diffraction numbers. The bottom diagram shows the dependency of the diffraction number. The different curves are labeled by the beam-waist diameter in units of µm.

chip and the external mirror, whilst M^2 is a function of the resonator length, one would expect a behavior like that. In section 2.2, experimental evidence for such a dependency will be given. It is obvious from the above assumptions, that a limiting condition

$$R_c > \frac{\pi\omega_0^2}{2\lambda} \tag{5}$$

for the mirror radius of curvature exists, at which diffraction limited operation becomes possible. It can be supposed that efficient laser operation only is possible if the laser mode diameter on the chip is not smaller than the pump spot size. If, for example, the pump spot has a diameter of more than 400 µm, then in turn diffraction limited operation for the smaller principal axis can be expected only for a mirror with a radius of curvature longer than 256 mm.

2.2 Experiment

It is well approved by experimental experience that the diffraction number of a semiconductor disk laser increases with increasing pump spot sizes for a given geometry of the cavity. On the other hand, the smaller the pump spot size becomes, the smaller is the range of the cavity lengths in which lasing is possible. Such a behavior can easily be explained by Fig. 1. In order to give a more quantified verification, a series of beam quality and optical-power measurements, shown in Fig. 2 has been performed. In that,

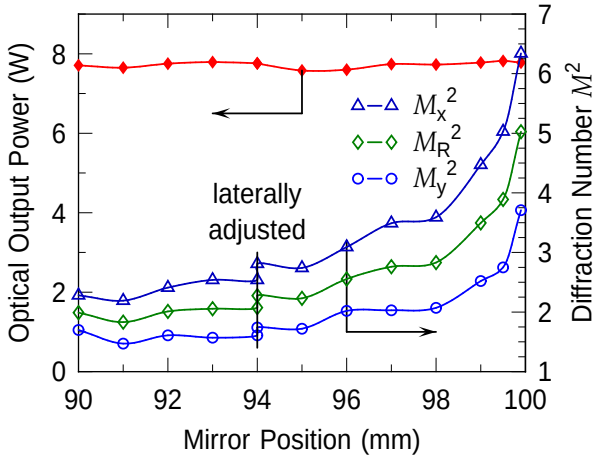

Fig. 2: Series of beam-quality and output-power measurements at different mirror positions. A minor influence on the output power can be observed, whereas there is a significant influence on the vertical and horizontal beam quality.

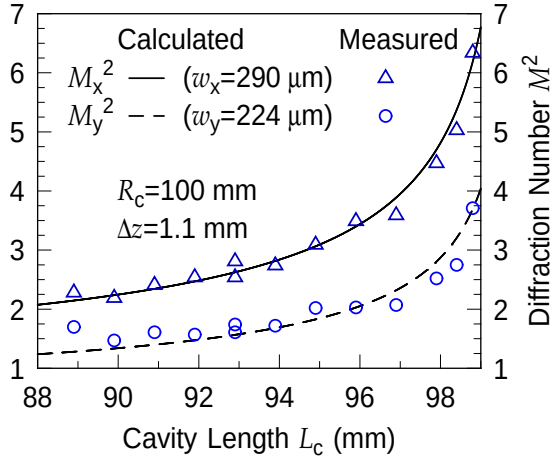

Fig. 3: Fit of the experimental data from Fig. 2 using equation (4). Besides the beam-waist diameters, a slightly position offset Δz, which is within the uncertainty of measurement of the cavity length, was used as a fit parameter.

the cavity length was varied by moving the position of the outcoupling mirror. At a mirror position that corresponds to a cavity length which is close to the mirror's radius of curvature, multi-mode emission with a relatively high diffraction number can be observed. As the laser is pumped under an angle of approximately 25°, the pumped area is elliptical, resulting in different horizontal and vertical diffraction numbers M_x^2 and M_y^2. The geometrical mean M_R^2 represents the effective diffraction number, that corresponds to the diffraction number of a circular beam with the same beam quality. By decreasing the resonator length an increase in the beam quality, which goes ahead with a decrease in the diffraction numbers, can be observed. The correlation with the behavior, predicted by (4) is shown in Fig. 3. The horizontal and vertical beam-waist diameters as well as a position offset Δz are used as fit-parameters. The latter can be justified by the uncertainty of the measured cavity length. The ellipticity of the laser mode on the chip which is achieved that way to be $\omega_x = 290\,\mu\text{m}$ and $\omega_y = 224\,\mu\text{m}$ can not be explained by the pump angle alone. Possible explanations for that are a vertical misalignment of the resonator with respect to the pump spot or a slightly non-planarity of the laser chip and its backside Bragg mirror. Also a misalignment of the traveling stages z-axis with the optical axis has to be taken into account, particularly as a horizontal re-adjustment was necessary at the

labelled z-position. The measurement of the pump spot size itself which was performed by imaging the photoluminescence from the laser-chip to a CCD-camera revealed a value of approximately $230 \times 200\,\mu\text{m}$. Finally it should be mentioned, that the presence of an adequately large dark-line free region seems to be an essential requirement for the here presented experimental result, because dark lines within the pumped region lead to a distinct decline of the beam quality which is not incorporated by the model.

3. High-Power Operation

To achieve high conversion efficiencies which are required for the minimization of generated heat, different design features have been utilized in the epitaxial design of the structure whose characteristics is presented here. First, a proper strain compensation that reduces relaxation defects at which nonradiative recombination takes place [7] is necessary. This is introduced by means of GaAsP layers that are placed between the six InGaAs quantum wells of the acitve region. Another measure is the utilization of a double-band Bragg mirror, that provides not only a high-reflectivity band at the emission wavelength around 980 nm, but also another one for the pump radiation with a wavelength of 808 nm [8]. This reduces the heat, generated by the fraction of the pump beam which is transmitted through the Bragg mirror and penetrates the subsequent metalization layers. Furthermore, the double-pass transmission of the pump beam leads to a more homogeneous carrier generation which increases the differential efficiency due to a reduced virtual threshold shift [9]. A third constructive feature which has to be mentioned is that the micro-cavity of the laser-chip has been performed in way that the surface of the semiconductor lies within an antinode of the longitudinal standing wave pattern of the mode. To obtain that, a quarter-wavelength coating of the semiconductors surface is utilized.

The output characteristics of a device with the mentioned features is shown in Fig. 4. The laser was pumped by a fiber-coupled diode laser with a wavelength of 808 nm under a pump angle of 25° what led to a pump-spot area of $450 \times 500\,\mu\text{m}$. A mirror with 100 mm radius of curvature was used in the setup, because none with a bigger radius of curvature was available at the time of the measurement. The cavity was adjusted to provide maximum optical output power. The temperature of the copper heatsink of the device was actively controlled by a Peltier cooler. At a temperature of -5 °C and an absorbed optical power of 24.5 W, an output power of 13.2 W was measured in the high-order transverse-modal output beam, that corresponds to a conversion efficiency of 54 %. The output characteristics also has been measured at 0 °C, where thermal roll over took place at 12.3 W output power. In Fig. 5, the absorption characteristics of the same measurement is shown. Both, the absorbed pump power, as well as the absorptance are achieved by measuring the reflected pump power. The absorptance shows a distinct dependency on the temperature and reaches its maximum of 94.5 % at the maximum output power and a heat-sink temperature of 0 °C. Of course, the temperature of the structure itself is increasing with increasing pump power. With increasing temperature, the spectral reflectivity characteristics of the structure's Bragg-mirror is shifted towards longer wavelengths. Hence the observed temperature behavior can be easily explained by the assumption that the pump beam is reflected at the short-wavelength edge of the

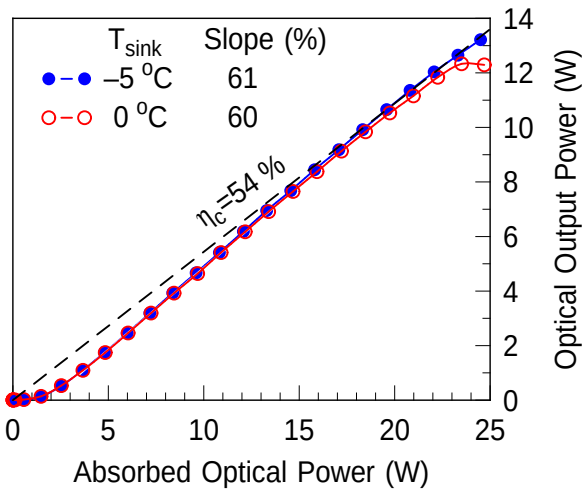

Fig. 4: Output characteristics of a disk laser with an emission wavelength of 970 nm and an outcoupling mirror having a reflectivity of 98 % and a radius of curvature of 100 mm. The pump spot size was measured as 450 × 500 µm.

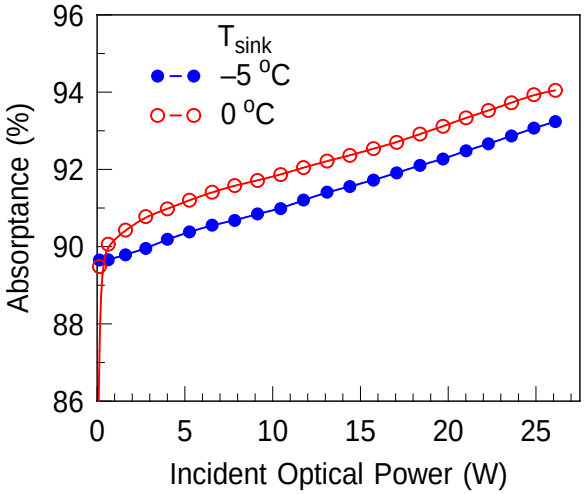

Fig. 5: Corresponding absorption characteristics of the measurement represented in Fig. 4.

mirror's pump-wavelength reflection band. Anyway, due to the high absorptance, even for the low temperature curve, an incident optical power of only 26.1 W was necessary to achieve the maximum output power, resulting in an optical to optical conversion efficiency of more than 50 %.

4. Conclusion and Outlook

The model presented for the influence of the laser cavity geometry on the beam parameters which takes the diffraction number into account appears to be a suitable tool to determine the output behavior of optically-pumped semiconductor disk lasers and for finding a suitable cavity configuration. For large pump-spot areas which are required for high power operation, near diffraction limited operation is possible only for external mirrors with a radius of curvature that extends a certain value, which is given by (5). The basic assumption, that the on-chip beam diameter of the laser mode is determined rather by the pump-spot extension than by the cavity length and the mirror radii appears to be valid at a large extent. The presented design features facilitate high-power operation even with low-cost copper mounts. With CVD-diamond heat spreaders or microchannel coolers [10] even higher optical output powers than the presented 13.2 W appear possible.

References

[1] J. Chilla, S. Butterworth, J. Charles, A. Capra, M. Reed, and L. Spinelli,"High Power optically pumped semiconductor lasers", *Proc. SPIE*, vol. 5332, pp. 143–150, 2004.

[2] A. Härkönen, S. Suomalinen, E. Saarinen, L. Orsila, R. Koskinen, O. Okhotnikov, S. Calvez and M. Dawson, "4 W single-transverse mode VECSEL utilising intra-cavity diamond heat spreader", *Electron. Lett.*, vol. 42, no. 12, pp. 693–694, 2006.

[3] J. Lee, S. Lee, T. Kim and Y. Park,"7 W hight-efficiency continuous-wave green light generation by intracavity frequency doubling of an end-pumped vertical external-cavity surface emitting semiconductor laser", *Appl. Phys. Lett.*, vol. 89, 241107, 2006.

[4] A.E. Siegman, "Defining the effective radius of curvature for a nonideal optical beam", *IEEE J. Quantum Electron.*, vol. 27, no. 5, pp. 1146–1148, 1991.

[5] A.E. Siegman,"Defining and Measuring Laser Beam Quality", in *Solid State Lasers: New Developments and Applications*, M. Incuscio and R. Wallenstein (Ed.), pp. 13–28. New York: Plenum Press, 1993

[6] M. Kuznetsov, F. Hakimi, R. Sprague, and A. Mooradian, "Design and characteristics of high-power (>0.5-W cw) diode-pumped vertical-external-cavity surface-emitting semiconductor lasers with circular TEM_{00} beams", *IEEE J. Select. Topics Quantum Electron.*, vol. 5, no. 3, pp. 561–573, 1999.

[7] F. Demaria, M.C. Riedl, F. Rinaldi, S. Lorch, and U. Brauch, "Advanced Optically-Pumped Semiconductor Disk Lasers With Barrier and Quantum-Well Pumping", *Annual Report 2005, Ulm University, Optoelectronics Department.*

[8] E. Gerster, I. Ecker, S. Lorch, C. Hahn, S. Menzel and P. Unger,"Orange-emitting frequency-doubled AsAsSb/GaAs semiconductor disk laser", *J. Appl. Phys.*, vol. 94, no. 12, pp. 7397–7401, 2003.

[9] O. Casel, *Experimentelle Untersuchung und Modellierung des Einflusses der Epitaxiestruktur auf die physikalischen Eigenschaften optisch angeregter Halbleiterscheibenlaser*. Ph.D. thesis, University of Kaiserslautern, Göttingen: Cuviller, 2005.

[10] E. Gerster, "Semiconductor Disk Laser on Microchannel Cooler", *Annual Report 2004, Ulm University, Optoelectronics Department.*

Optical Coatings for Disk Lasers

Steffen Lorch

The performances of disk lasers can be improved with optical coatings which is shown for two different applications. For an AlGaAs disk laser, the efficiency was increased from 34 % to 50 % using an antireflective coating. Additionally, such a coating passivates the surface resulting in an higher lifetime. For an AlGaN disk laser, the Bragg mirror was fabricated by dielectric layers to achieve the required high reflectivity over 0.995 with only 9 layer pairs and a thermal stability up to 800 °C.

1. Introduction

Thin layers of dielectric materials have a wide range of applications. Especially for optoelectronic devices, such coatings are needed to improve the performances. With optical coatings, the surface reflectivity can be adjusted resulting in higher efficiencies. But also the passivation effect increases the lifetime of such devices. The high quality of the deposited layers is an important factor mainly for high output power densities. The intension is to achieve coatings with low absorption by the use of stoichiometric oxides. A methode to get such layers is the reactive ion-beam sputter deposition [1]–[4], which was used in this work.

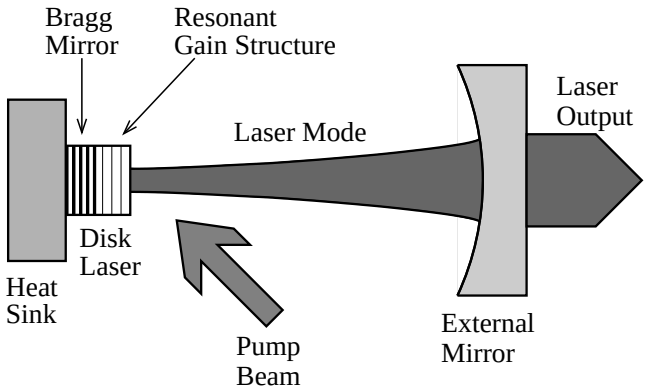

Fig. 1: Illustration of a disk-laser setup. The semiconductor disk laser itself is soldered on a heat sink and consists of a Bragg mirror and a resonant gain structure. An external concave mirror is used to build up the resonator. The pumping is performed optically by a laser beam.

In Fig. 1, a disk-laser setup, also known as OPSDL (*optically-pumped semiconductor disk laser*) or VECSEL (*vertical-external-cavity surface-emitting laser*) is shown [5]–[7]. The disk laser is pumped optically with e. g. an high-power laser bar or laser stack. The pump light is absorbed in the resonant gain structure where the generated carriers recombine and produces laser emission. The resonator is built up by the Bragg mirror and the

external concave mirror. For a good thermal management, the disk laser is soldered on a heat sink. There are a lot of applications for optical coatings on such a disk-laser setup. The external mirror mostly has dielectric multilayer coatings to achieve the required high reflectivities with very low absorptions. But also bandpass filters are used for intra-cavity frequency doubling [8],[9]. Especially in the AlGaN material system, the Bragg mirror consists of dielectric layers due to the small refractive index change between AlGaN and GaN. The coating of the disk laser surface is also an important fact which influences the properties of the laser. In the next sections, two examples for applications of optical coatings on disk lasers will be presented.

2. Antireflective Coating on Disk-Laser Surface

An increase not only of the efficiency but also of the lifetime can be obtained by an AR (*antireflective*) coating. On a AlGaAs disk laser with an emission wavelength of 980 nm, a $\lambda/4$ thick Al_2O_3 layer with a refractive index of $n = 1.66$ was deposited on the surface.

In Fig. 2, the output characteristic of a disk laser is shown. In the left part of the graph, the optical output power is depicted over the whole pump power. It can be seen, that the slope in the characteristic of the coated disk laser and so the efficiency is larger compared to the disk laser without coating. The laser threshold decreases from 425 mW to 300 mW. One reason is the decrease in the surface reflectivity for the pump wavelength of 808 nm at a pump angle of 45° from 0.2 to 0.05. More pump light can reach the absorption region in the semiconductor material, the pumping is more efficient. This effect is taken into account in the right part of the graph. Here the output power is plotted over the absorbed pump power. The coated disk laser still shows a higher efficiency compared to the uncoated one. The differential efficiency η_{diff} increases with coating from 34 % to 50 %. Due to the decreased surface reflectivity for the laser wavelength of 980 nm from

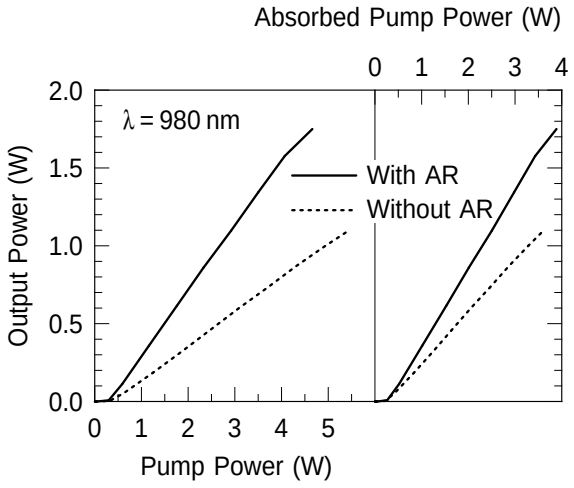

Fig. 2: Optical output power over pump power and absorbed pump power for a disk laser with and without AR coating.

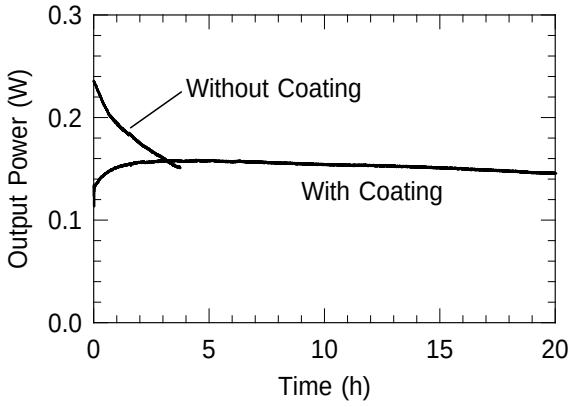

Fig. 3: Longtime measurement of the output power of a disk laser with and without AR coating.

0.3 to 0.02, the whole outcoupling reflectivity of external mirror plus surface reflectivity is lower and more light can be coupled out. The threshold pump power is not effected by this decrease from 0.986 to 0.98 and shows 290 mW in both cases. Also the maximum output power of the coated laser is larger due to the increased output transmission from 1.4 % to 2 %.

In Fig. 3 the influence of the passivation of the used AR-coating is shown. It can be seen, that the output power of the uncoated laser rapidly decreases in the first hours of operation. In contrast, the output power of the coated laser remains nearly constant over the time. This results show the improvement of the longtime stability of a disk laser by a passivation layer.

3. Bragg Reflector for AlGaN Disk Lasers

In the material system of AlGaN, an epitaxially grown Bragg reflector is not suitable due to the small refractive index contrast of GaN and AlN [10]. A better way is to use dielectric materials to achieve a high reflectivity with an adequate number of layers [11]–[13]. For such a disk laser with an emission wavelength of 405 nm and a pump wavelength of 355 nm at 40°, a Bragg reflector with SiO_2 and Ta_2O_5 was fabricated. For the characterization, some test substrates were coated during the deposition process.

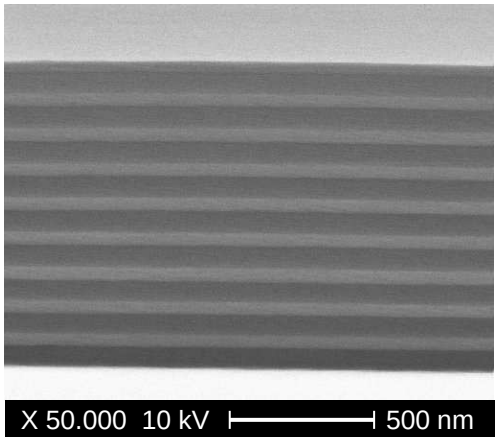

Fig. 4: SEM picture of the dielectric Bragg mirror. On a GaAs test substrate (white) 18 layers can be identified. Each layer pair consists of 67 nm SiO_2 (dark grey) and 45 nm Ta_2O_5 (bright grey).

An SEM picture of the deposited Bragg reflector can be seen in Fig. 4. On a GaAs substrate (white), 9 layer pairs can be recognized. The low-refractive material is SiO_2 with a thickness of 67 nm and appears as the darkgrey layers in the SEM picture. The brighter-grey layers are 45 nm thick Ta_2O_5 which is used as the high-refractive material. The whole thickness of the mirror is approx. 1 µm. In Fig. 5, the wavelength-dependent reflectivity for 0° is shown. There is a good agreement between the simulated and measured curves. For the emission wavelength of 405 nm the reflectivity shows the required maximum. Additionally, the simulated reflectivity for 40° is included in the diagram to recognize the maximum for the pump wavelength at 355 nm.

The reflectivity is dependent of the refractive indices of the substrate n_S, the incident medium n_0, the low n_L and high n_H refractive material, and the number of layer pairs m.

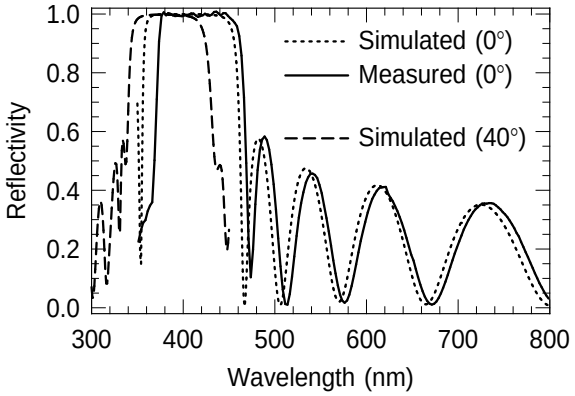

Fig. 5: Simulated and measured reflectivity over wavelength of the dielectric Bragg mirror containing 18 layers. The simulated curve for 355 nm and 40° is also given.

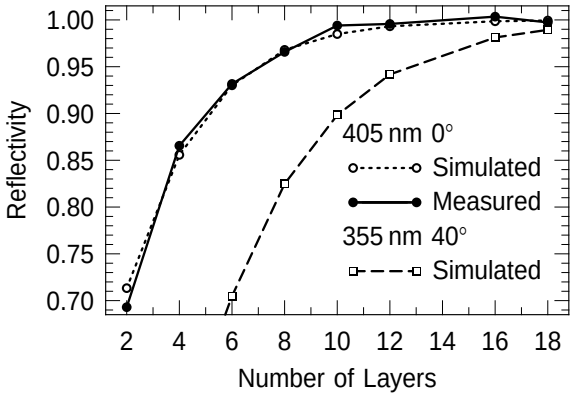

Fig. 6: Simulated and measured reflectivity for 405 nm and 0° versus the number of layers. The simulated curve for 355 nm and 40° is also given.

It can be calculated by using [14]

$$R = \left(\frac{1 - \frac{n_S}{n_0} \left(\frac{n_H}{n_L} \right)^{2m}}{1 + \frac{n_S}{n_0} \left(\frac{n_H}{n_L} \right)^{2m}} \right)^2 . \quad (1)$$

During the depostion sequence of the disk laser, different test substrates were removed between the deposition of the individual layer pairs. So it was possible to measure the reflectivity dependency on the number of deposited layers that is plotted in Fig. 6. There is a high agreement between the simulated reflectivity (Eqn. 1) for the emission wavelength of 405 nm at 0° and the measured one. With 18 layers, a reflectivity of over 0.995 is achieved. Additionally the simulated reflectivity for the pump wavelength of 355 nm at 40° is depicted. It can be seen that the reflectivity for 18 layers is 0.99 which is high enough for an effective pumping.

With an RTA process (*rapid thermal annealing*), the 18-layer Bragg mirror on a Si test substrate were stressed with different temperatures for 2 minutes under nitrogen atmosphere. After each temper step, the wavelength dependent reflectivity were measured as depicted in Fig. 7. There is only a small shift in wavelength and a small decrease in reflectivity.

In Fig. 8, the change of the reflectivity for 405 nm is drawn over the temper temperature like indicated by an arrow in Fig. 7. Up to a temperature of 800 °C, no significant change can be observed. A decrease in the reflectivity starts not below 900 °C. Also the wavelength shift of the band edge is given (right arrow in Fig. 7). Over the temperature range up to 1000 °C there is only a shift of 12 nm. These small changes of the Bragg mirror indicate the high stability of the coated dielectric layers. Therefore, such optical coatings are predestinated for the use with high optical power densities.

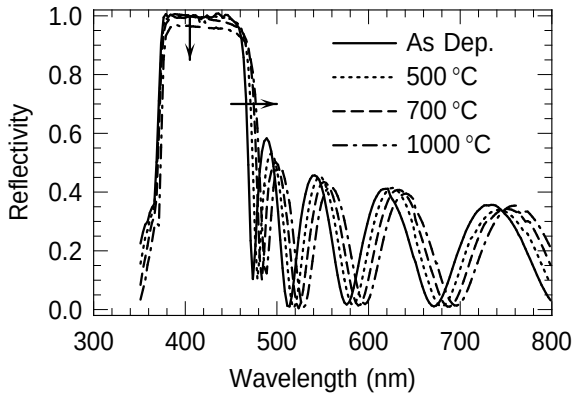

Fig. 7: Wavelength-dependent reflectivity for different temperatures.

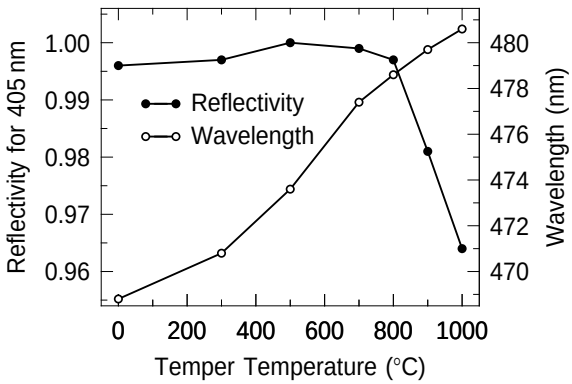

Fig. 8: Reflectivity for 405 nm and wavelength shift on band edge for different temperatures.

4. Conclusion

Optical coatings are an important component for the fabrication of disk lasers. With a simple $\lambda/4$-AR coating on the surface of a disk laser, the efficiency and lifetime were increased. For an AlGaN disk laser, the Bragg mirror was realized by dielectric layers. A reflectivity over 0.995 was achieved with 9 pairs. The mirror shows a thermal stability up to 800 °C.

References

[1] J.M.E. Harper, "Ion beam deposition," ch. II-5 in *Thin Film Processes,* J.L. Vossen, W. Kern (Ed.), New York: Academic Press, Inc., pp. 175–206, 1978.

[2] J. Becker, "Ion-beam sputtering," ch. 7 in *Handbook of Optical Properties, Volume I Thin Films for Optical Coatings,* R.E. Hummel, K.H. Guenther (Ed.), Boca Raton: CRC Press, pp. 189–212, 1995.

[3] D.T. Wei, H.R. Kaufman, and C.-C. Lee, "Ion beam sputtering," ch. 6 in *Thin Films for Optical Systems,* F.R. Flory (Ed.), New York: Marcel Dekker, pp. 133–201, 1995.

[4] A.M. Ektessabi, "Ion-beam-assisted sputter deposition of thin oxide films," *Surf. Coat. Technol.*, vol. 68–69, pp. 208–216, 1994.

[5] M. Kuznetsov, F. Hakimi, R. Sprague, and A. Mooradian, "Design and characteristics of high-power (>0.5-W cw) diode-pumped vertical-external-cavity surface-emitting semiconductor lasers with circular TEM_{00} beams," *IEEE J. Selected Topics Quantum Electron.*, vol. 5, no. 3, pp. 561–573, 1999.

[6] S. Lutgen, T. Albrecht, P. Brick, W. Reill, J. Luft, and W. Späth, "8-W high-efficiency continuous-wave semiconductor disk laser at 1000 nm," *Appl. Phys. Lett.*, vol. 82, no. 21, pp. 3620–3622, 2003.

[7] J. Chilla, S. Butterworth, A. Zeitschel, J. Charles, A. Caprara, M. Reed, and L. Spinelli, "High power optically pumped semiconductor lasers," *Proc. SPIE*, vol. 5332, pp. 143–150, 2004.

[8] E. Schiehlen, M. Golling, and P. Unger, "Diode-pumped semiconductor disk laser with intra-cavity frequency doubling using lithium triborate (LBO)," *IEEE Photon. Technol. Lett.*, vol. 14, no. 6, pp. 777–779, 2002.

[9] E. Gerster, I. Ecker, S. Lorch, C. Hahn, S. Menzel, and P. Unger, "Orange-emitting frequency-doubled GaAsSb/GaAs semiconductor disk laser," *J. Appl. Phys.*, vol. 94, no. 12, pp. 7397–7401, 2003.

[10] G.M. Laws, E.C. Larkins, I. Harrison, C. Molloy, and D. Somerford, "Improved refractive index formulas for the $Al_xGa_{1-x}N$ and $In_yGa_{1-y}N$ alloys," *J. Appl. Phys.*, vol. 89, no. 2, pp. 1108–1115, 2001.

[11] Y.-K. Song, H. Zhou, M. Diagne, A.V. Nurmikko, R.P. Schneider, C.P. Kuo, M.R. Krames, R.S. Kern, C. Carter-Coman, and F.A. Kish, "A quasicontinuous wave, optically pumped violet vertical cavity surface emitting laser," *Appl. Phys. Lett.*, vol. 76, no. 13, pp. 1662–1664, 2000.

[12] Y.-K. Song, M. Diagne, H. Zhou, A.V. Nurmikko, R.P. Schneider, and T. Takeuchi, "Resonant-cavity InGaN quantum-well blue light-emitting diodes," *Appl. Phys. Lett.*, vol. 77, no. 12, pp. 1744–1746, 2000.

[13] S.-H. Park, J. Kim, H. Jeon, T. Sakong, S.-N. Lee, S. Chae, Y. Park, C.-H. Jeong, G.-Y. Yeom, and Y.-H. Cho, "Room-temperature GaN vertical-cavity surface-emitting laser operation in an extended cavity scheme," *Appl. Phys. Lett.*, vol. 83, no. 11, pp. 2121–2123, 2003.

[14] H.A. Macleod, *Thin-Film Optical Filters*, Bristol: Institute of Physics Publishing (IoP), 3. ed., 2001.

Polarization-Controlled Surface Grating VCSELs Under Unpolarized and Polarized Optical Feedback

Johannes Michael Ostermann and Pierluigi Debernardi[†]

The polarization control of a surface grating vertical-cavity surface-emitting laser (VCSEL) and of a nominally identical standard VCSEL without a surface grating are compared for unpolarized and polarized optical feedback with different feedback levels in the long external cavity regime. While the polarization of the standard VCSEL is strongly influenced by isotropic feedback with a feedback level of just 1 % and can even be controlled by polarized feedback, the surface grating VCSEL remains polarization-stable under isotropic feedback. Its polarization can only be disturbed by optical feedback polarized orthogonal to the polarization of the solitary surface grating VCSEL for feedback levels exceeding 18 %.

1. Introduction

The polarization of common VCSELs is very sensitive to optical feedback [1]. It can be switched by means of polarization-selective optical feedback [2], by feedback with rotated polarization [3], or by varying the phase of the feedback in an extremely short external cavity [4]. While the polarization phenomena under feedback are very interesting from a laser physics point of view, VCSELs which are polarization-stable especially under feedback are highly sought-after for many applications, since feedback cannot be avoided in most optical setups. It can already be caused by a collimating lens without an anti-reflection coating or by the facet of an optical fiber into which the laser light is coupled.

While promising results for polarization control were achieved in the past by growth on substrates with higher indices in combination with strained quantum wells, in the last years semiconductor surface gratings have proven to reliably control the polarization of VCSELs fabricated on standard (001)-oriented GaAs substrates [5, 6] even under high-frequency modulation [7]. In the following, it is investigated whether this polarization control is robust enough to withstand even strong and polarized optical feedback.

It is beyond the scope of this article to provide a comprehensive and conclusive investigation of the polarization properties of grating VCSELs under feedback. Instead, we limit ourselves to the long external cavity regime, which is characterized [8] by an external roundtrip delay time (in the present case about 4 ns, corresponding to an approximately 60 cm long external cavity) larger than the inverse of the relaxation oscillation frequency of the laser (typically several GHz in the case of VCSELs). In this regime, the observed physical effects are expected to be qualitatively independent from phase variations in the feedback, which can result, for instance, from a change of the external cavity length. This assumption has been experimentally validated for the measurements presented in this article.

[†]Pierluigi Debernardi is with the IEIIT-CNR c/o Politecnico di Torino, Torino, Italy

2. Measurement Setup

The measurement setup used for the optical feedback experiments is schematically sketched in Fig. 1. The setup comprises the feedback path which consists of an external mirror, a polarizer, and a variable optical attenuator and the detection path with a second polarizer and a photodetector. In addition, there are a halogen lamp and a CCD camera to identify the VCSELs on the chip and facilitate probing. Behind the collimating lens with a transmittivity of 97 %, an uncoated wedge plate is inserted into the optical path to extract about 4 % of the light from the external cavity for detection. A polarization-independent beam splitter with a 50:50 splitting ratio, as it is often used in such setups, would limit the available feedback level (the portion of the laser emission reflected back on the laser facet) to a level below the one of interest, since the polarization properties of VCSELs with a surface grating are quite robust against feedback, as will be shown later. Due to a lack of space on the optical table, the wedge plate had to be inserted into the optical path of the external cavity under a relatively large angle of about 6 degrees. The reflectance at a single facet of the wedge plate is therefore about 3 % larger for the polarization orthogonal to the optical bench than for the polarization parallel to the optical bench, as follows from Fresnel's equations. Since during one round-trip in the external cavity, four facets of the wedge plate are passed, the transmission in the external cavity and thus the feedback level is about 12.5 % higher for the polarization parallel to the optical bench than for the orthogonal polarization, as long as no additional polarization-selective element is inserted into the cavity.

The optical attenuator behind the wedge plate has a variable transmittivity between 0 and 70 % and is used to adjust the feedback level. The polarizer, which can optionally be inserted into the feedback path, exhibits losses of about 6 %. The feedback loop is closed by an external dielectric mirror with a reflectivity exceeding 99 %. In total, the setup allows to vary the feedback level between 0 and 39 %. A typical feedback level to be expected in some applications is about 4 %, corresponding to a reflection from an uncoated glass surface. With the given measurement setup, this expected feedback level can be exceeded by almost a factor of ten.

Besides the reflectivities, the actual feedback strength depends also on the mechanical alignment. In all measurements presented here, the external cavity is carefully aligned. The external mirror and the collimating aspheric lens are iteratively adjusted several times to optimize for the smallest laser threshold current under feedback. Consequently, the feedback strengths are higher than the ones expected for unwanted feedback for a given external reflectivity.

3. VCSELs Under Investigation

To guarantee an as high as possible modal overlap between the laser mode and the feedback field, single-mode VCSELs are desirable for the investigation of feedback phenomena. Therefore VCSELs with a high single-mode current range and a high single-mode output power are chosen for this investigation. The lateral extent of the surface grating of the investigated devices is limited to five grating ridges to form a grating relief [9]. The purpose

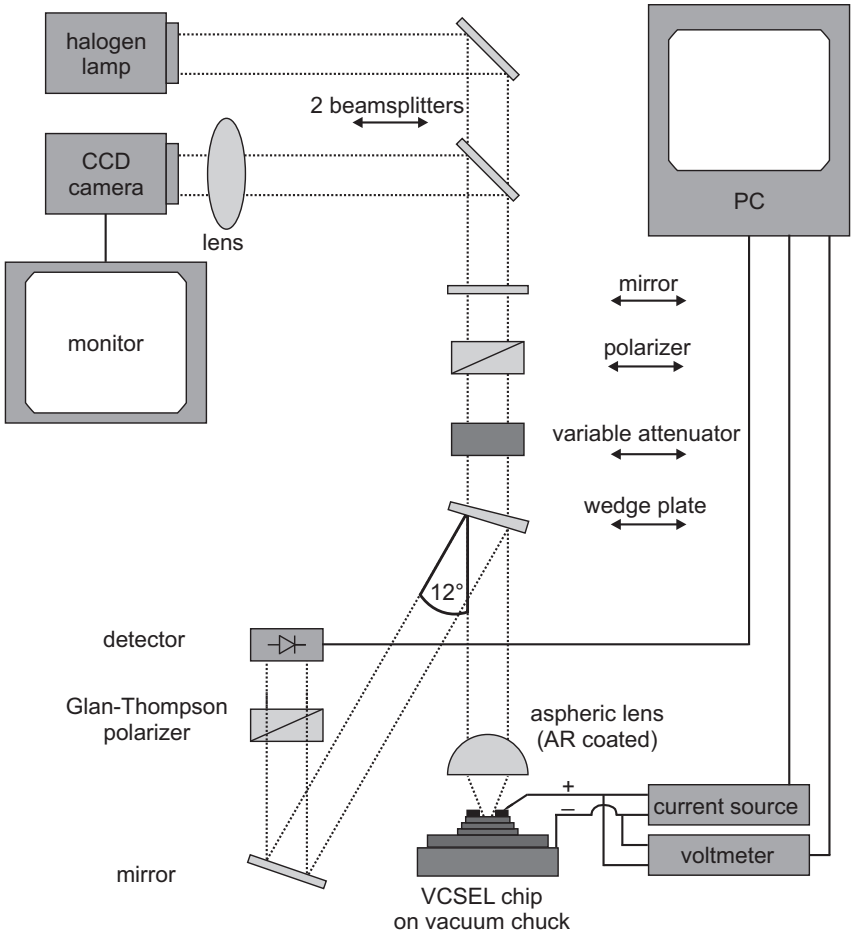

Fig. 1: Schematic drawing of the measurement setup used for the feedback investigations. The double arrows indicate components which can be removed from the optical path.

of such a grating relief is to increase the single-mode output power of the VCSELs. This concept has proven to be successful and single-mode output powers as high as 4.2 mW have been obtained [10]. Standard VCSELs on the same sample deliver single-mode output powers up to 3.5 mW. A much stronger increase of the single-mode output power than with the given normal grating relief structure can be achieved with an inverted grating relief [11].

The polarization-resolved light–current (PR-LI) characteristics of the two VCSELs investigated in the following are shown in Fig. 2. Both VCSELs have an active diameter of about 4 µm and an emission wavelength of 924 nm. They are nominally identical, except that the VCSEL on the left is a standard VCSEL without any surface modification, while the laser on the right is a grating relief VCSEL with a grating period of 0.8 µm, a grating depth of 57 nm, and an outer grating diameter of 3.6 µm. Since the grating is laterally limited to the center of the VCSEL, the polarization control achieved by the grating is weakened. The reduced mirror reflectivity outside of the grating region of such a grating relief VCSEL makes it simultaneously more vulnerable to optical feedback. This reduced overall reflectivity of the Bragg mirror also causes the much higher threshold current of

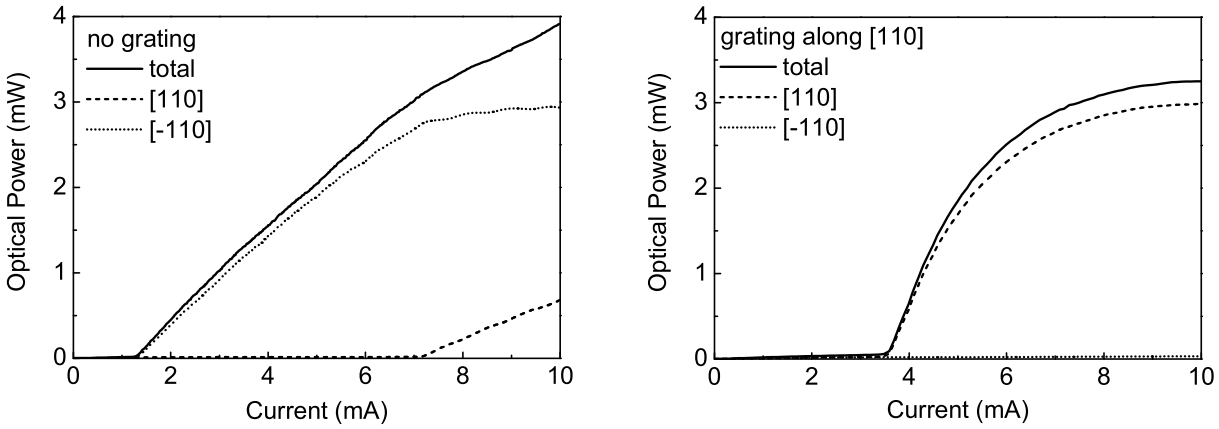

Fig. 2: PR-LI characteristics (without feedback) of a standard VCSEL (left) and a grating VCSEL (right) investigated in the following.

the grating VCSEL compared to the standard VCSEL in Fig. 2. However, the grating VCSEL is single-mode up to thermal rollover, while higher-order modes start to lase in the standard VCSEL at a current of 6.9 mA with a polarization orthogonal to that of the fundamental mode.

4. Isotropic Feedback

Without feedback, both, the standard VCSEL as well as the grating VCSEL exhibit a stable polarization of their fundamental mode. The polarization of the standard VCSEL is oriented along the $[\bar{1}10]$ crystal axis and the polarization of the grating VCSEL along the [110] crystal axis and therefore parallel to the grating grooves. Quasi-isotropic feedback is investigated first. The term quasi refers to the slight polarization asymmetry of the external cavity introduced by the wedge plate, as discussed above. The lasers are mounted in such a way that the $[\bar{1}10]$ and [110] crystal axes are oriented parallel and orthogonal to the optical bench, respectively. Thus the feedback strength along the $[\bar{1}10]$ crystal axis is higher than along [110]. Consequently, the dominant polarization of the standard VCSEL is favored and the dominant polarization of the grating VCSEL is disfavored. However, as soon as the quasi-isotropic feedback is applied, the standard VCSEL is no longer stable, as can be seen in the left graph of Fig. 3.

With increasing feedback strength, the standard VCSEL exhibits (at least in its single-mode range) an almost equal distribution of its output power between the polarization along the [110] (top half of the graph) and the $[\bar{1}10]$ crystal axis (bottom half). The influence of the feedback on the threshold current is enlarged as a total-output-power-versus-current diagram in the inset in the bottom half of the graph. As expected, the reduction of the threshold current with increasing feedback is larger for the grating VCSEL than for the standard VCSEL due to the reduced reflectivity of the upper Bragg mirror. This also explains the different shape of the LI characteristics of both lasers, especially close to threshold. However, virtually no influence of the feedback on the polarization properties of the grating VCSEL can be observed in the right graph of Fig. 3, even for a feedback level as high as 39 %.

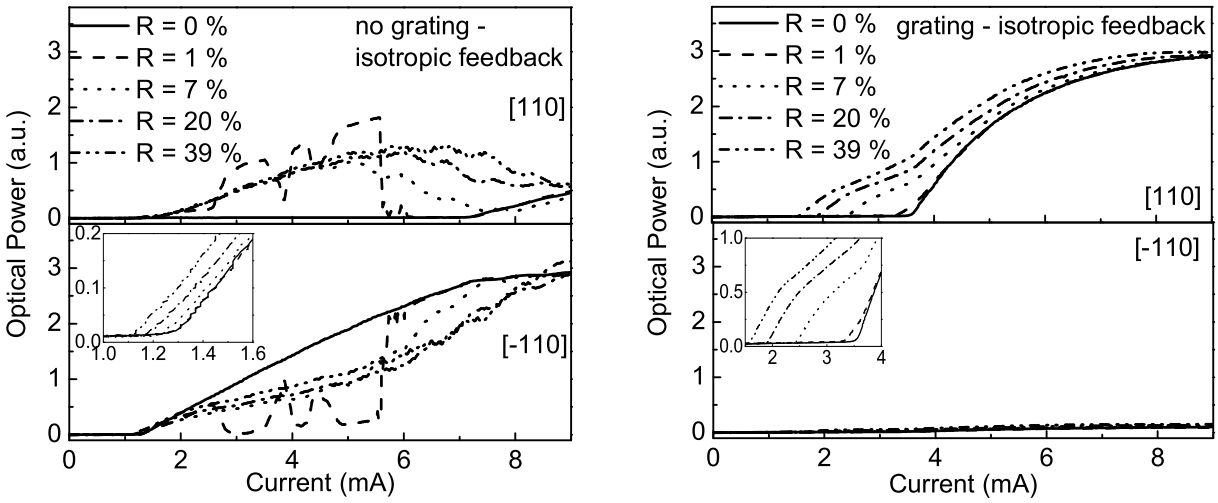

Fig. 3: PR-LI characteristics of the standard (left) and of the grating VCSEL (right) from Fig. 2 under quasi-isotropic feedback. The power in the [110] polarization is given in the top half of each graph, while the power in the [$\bar{1}$10] polarization is displayed in the bottom half. The reflectivity of the external cavity R and therefore the feedback level is varied between 0 and 39 %. The optical power is given in arbitrary units, which are chosen such that their magnitude corresponds to the optical power in mW emitted by the VCSELs in the case without feedback. The reduction of the threshold current with increasing feedback level can be read from the enlarged insets in both graphs, which give the total output power in the same arbitrary units versus the drive current in mA.

5. Polarized Feedback

Quasi-unpolarized feedback is the most probable type of feedback a VCSEL can be exposed to in common applications. Consequently, it is of high relevance that a grating VCSEL can withstand ten times the feedback level resulting from a single uncoated glass surface. However, besides isotropic feedback, also polarized feedback can occur in a setup with polarization-dependent optical elements. For testing highly polarized feedback, a polarizer is inserted into the external cavity.

The PR-LI characteristics of the standard VCSEL are shown in Fig. 4 under feedback polarized along the [$\bar{1}$10] crystal axis (left graph) and along the [110] crystal axis (right graph). Since the solitary standard VCSEL exhibits a dominant polarization along the [$\bar{1}$10] crystal axis, the feedback polarized parallel to that crystal axis in the left graph of Fig. 4 does not change the polarization properties of the device except for the case of a small feedback level of 1 %, for which a polarization switch from the [$\bar{1}$10] to the [110] crystal axis and back again is observed. When the polarizer is rotated by 90 degrees, so that the feedback is polarized along the [110] crystal axis and therefore orthogonal to the dominant polarization of the solitary standard VCSEL, already for a feedback level of 1 % its polarization is oriented parallel to the polarization of the feedback path and orthogonal to the dominant polarization of the VCSEL without feedback, as can be seen in the right graph of Fig. 4. The control of the polarization of the standard VCSEL by the polarized feedback is weakened somewhat for small feedback levels and higher drive currents. This is due to the heat dissipation inside the VCSEL, which results in a change

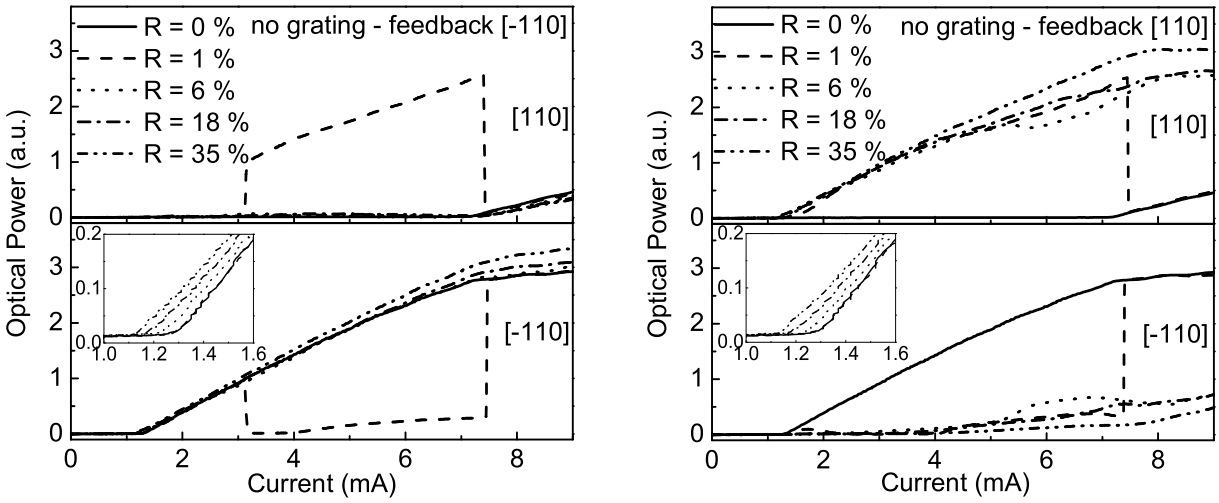

Fig. 4: PR-LI characteristics of the standard VCSEL from Fig. 2 under different levels of optical feedback polarized along the [$\bar{1}$10] crystal axis (left) and along the [110] crystal axis (right).

of the output beam profile and therefore in a less well-aligned external cavity.

In the measurements presented in Fig. 5, it is tested whether the polarization of a grating VCSEL can also be so easily controlled by polarized feedback as the polarization of the standard VCSEL above. As expected and shown in the left graph of Fig. 5, a feedback polarized parallel to the dominant polarization of the solitary grating VCSEL has no influence on its polarization properties. More interesting is the case presented in the right graph of the same figure, in which the feedback is polarized orthogonal to the dominant polarization of the solitary grating VCSEL. Since a surface grating is nothing else than a monolithically integrated type of polarization-dependent feedback, one intuitively expects that, above a certain feedback strength, a polarized external feedback can outbalance the feedback from the surface grating and cause a polarization switch if the orientations of the polarization preferred by the external feedback and preferred by the feedback from the grating are orthogonal to each other.

However, as can be seen in the right graph of Fig. 5, the feedback levels required to influence the polarization of the grating VCSEL are rather high. Even with 18 % of the suppressed polarization and no light in the dominant polarization of the solitary VCSEL reflected back on the laser facet, the polarization properties do not change compared to those of the solitary laser. Also no reduction of the threshold current can be observed for feedback levels up to 18 %. The latter effect is not caused by a less careful alignment, since just turning the polarizer by 90 degrees leads to the results displayed in the left graph of Fig. 5. Even for feedback levels exceeding 18 %, the current range in which the polarization is rotated with respect to the polarization of the solitary grating VCSEL is rather limited and is found close to threshold. Since the feedback is optimized for smallest threshold current and a higher current causes an increased heat dissipation inside the VCSEL and thus a modified emission characteristic of the laser, even a feedback level of 35 % is not high enough to control the polarization for all drive currents.

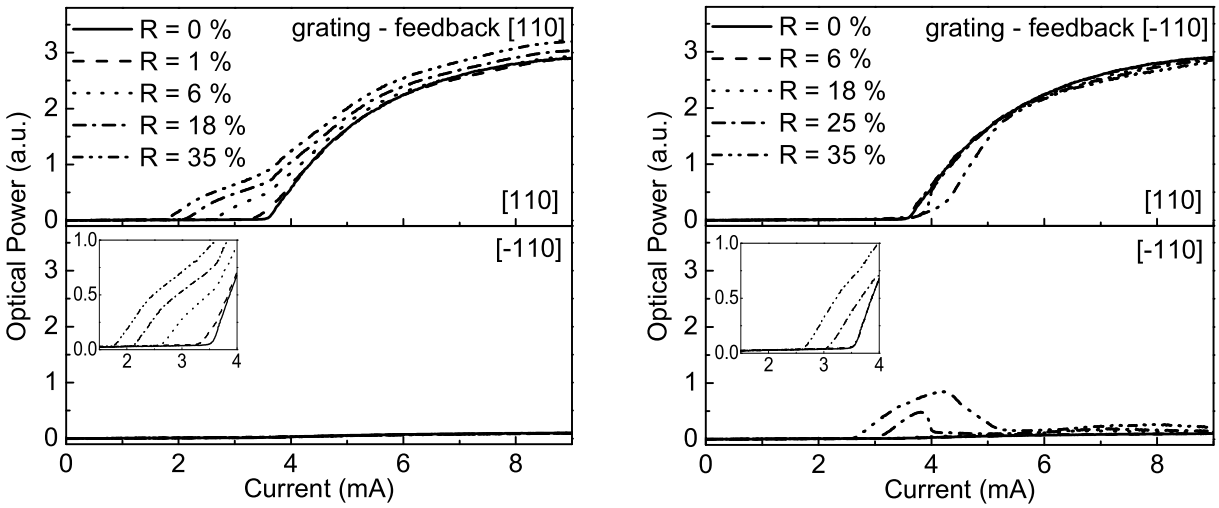

Fig. 5: PR-LI characteristics of the grating VCSEL from Fig. 2 under different levels of optical feedback polarized along the [110] crystal axis (left) and along the [$\bar{1}$10] crystal axis (right).

6. Conclusion

Surface gratings have proven to control the polarization of VCSELs also under isotropic feedback and even under orthogonally polarized optical feedback in the long external cavity regime up to feedback levels of 18 %. In contrast, the polarization of a nominally identical standard VCSEL which is stable without feedback becomes unstable already in case of 1 % isotropic feedback and can be controlled by polarized feedback from the external cavity. Although further investigations of the polarization properties of grating VCSELs under feedback are desirable especially in the short cavity regime, from the presented results one can already conclude that the polarization properties of grating VCSELs are much less sensitive to optical feedback than those of standard VCSELs and that surface gratings are capable of defining the polarization of VCSELs even under very strong external feedback.

Acknowledgment

The authors would like to acknowledge the help of Matthias Golling, Christof Jalics, and Yakiv Men in the fabrication of the sample and the fruitful discussions with Markus Sondermann.

References

[1] F. Robert, P. Besnard, M.L. Chares, and G.M. Stephan, "Switching of the polarization state of a vertical cavity surface-emitting laser using polarized feedback", *Opt. Quantum Electron.*, vol. 27, no. 9, pp. 805–811, 1995.

[2] C.I. Wilkinson, J. Woodhead, J.E.F. Frost, J.S. Roberts, R. Wilson, and M.F. Lewis, "Electrical polarization control of vertical-cavity surface-emitting lasers using

polarized feedback and a liquid crystal", *IEEE Photon. Technol. Lett.*, vol. 11, no. 2, pp. 155–157, 1999.

[3] S. Jiang, Z. Pan, M. Dagenais, R.A. Morgan, and K. Kojima, "High-frequency polarization self-modulation in vertical-cavity surface-emitting lasers", *Appl. Phys. Lett.*, vol. 63, no. 26, pp. 3545–3547, 1993.

[4] M.A. Arteaga, H.J. Unold, J.M. Ostermann, R. Michalzik, H. Thienpont, and K. Panajotov, "Investigation of polarization properties of VCSELs subject to optical feedback from an extremely short external cavity – part II: experiments", *IEEE J. Quantum Electron.*, vol. 42, no. 2, pp. 102–107, 2006.

[5] J.M. Ostermann, P. Debernardi, C. Jalics, A. Kroner, M.C. Riedl, and R. Michalzik, "Surface gratings for polarization control of single- and multi-mode oxide-confined vertical-cavity surface-emitting lasers", *Optics Communications*, vol. 246, no. 4–6, pp. 511–519, 2005.

[6] P. Debernardi, J.M. Ostermann, M. Feneberg, C. Jalics, and R. Michalzik, "Reliable polarization control of VCSELs through monolithically integrated surface gratings: a comparative theoretical and experimental study", *IEEE J. Select. Topics Quantum Electron.*, vol. 11, no. 1, pp. 107–116, 2005.

[7] J.M. Ostermann, P. Debernardi, and R. Michalzik, "Surface grating VCSELs with dynamically stable light output polarization", *IEEE Photon. Technol. Lett.*, vol. 17, no. 12, pp. 2505–2507, 2005.

[8] K. Petermann, "External optical feedback phenomena in semiconductor lasers", *IEEE J. Select. Topics Quantum Electron.*, vol. 1, no. 2, pp. 480–489, 1995.

[9] P. Debernardi and G.P. Bava, "Coupled mode theory: a powerful tool for analyzing complex VCSELs and designing advanced device features", *IEEE J. Select. Topics Quantum Electron.*, vol. 9, no. 3, pp. 905–917, 2003.

[10] J.M. Ostermann, P. Debernardi, C. Jalics, M. Feneberg, A. Kroner, M.C. Riedl, M. Golling, and R. Michalzik, "High single-mode power, monolithic polarization-controlled oxide-confined grating relief VCSELs", in Proc. *19th IEEE Int.'l Semicond. Laser Conf.*, pp. 109–110. Kunibiki Messe, Matsue-shi, Simane Pref., Japan, Sept. 2004. For corrections see URL http://www.uni-ulm.de/opto/forschung/ram/pub/islc2004.html .

[11] J.M. Ostermann, P. Debernardi, C. Jalics, and R. Michalzik, "Polarization-stable oxide-confined VCSELs with enhanced single-mode output power via monolithically integrated inverted grating reliefs", *IEEE J. Select. Topics Quantum Electron.*, vol. 11, no. 5, pp. 982–989, 2005.

Miniaturized Monolithically Integrated Transceiver Chips for Bidirectional Data Transmission over Graded-Index Glass Optical Fiber

Martin Stach and Fernando Rinaldi

We present bidirectional data transmission experiments in half-duplex mode at 1 Gbit/s data rate over 100 m graded-index glass optical fiber with VCSELs and MSM photodiodes as parts of a GaAs-based monolithically integrated transceiver chip.

1. Introduction

As a possible way to satisfy the need for compact and inexpensive solutions for high-speed optical interconnection, we describe a transceiver (Tx/Rx) chip that consists of a vertical-cavity surface-emitting laser (VCSEL) and a metal–semiconductor–metal photodiode (MSM PD). The monolithic integration of both components as well as a design avoiding the use of external optics are expected to simultaneously save space, weight, and module cost. A part of the circular-like detector area is occupied by the integrated VCSEL, thus enabling data transmission between two transceiver chips via a two-side butt-coupled fiber. Owing to an advanced processing technology, miniaturized Tx/Rx chips with 110 µm effective diameter have been fabricated, matching the 100 µm core of a graded-index multimode glass optical fiber (MMF). Compared to Tx/Rx chips with 210 µm diameter for data transmission over a step-index polymer-clad silica (PCS) fiber [1], the new design optimizes the detector area through circular-shaped MSM PD electrodes (Fig. 1). The MMF offers a bandwidth–length product of 100 GHz · m in contrast to the rather poor 3 GHz · m of the PCS fiber. Thus there is the capability to transmit signals at 1 Gbit/s data rate over distances found in high-volume industrial and home network sectors [2]. We first outline the processing of the Tx/Rx chips, followed by investigations on the dark current behavior of the PDs and coupling efficiencies between VCSEL and fiber. Dynamic characterization is performed in terms of bidirectional data transmission in half-duplex mode between two Tx/Rx chips.

2. Transceiver Chip Fabrication

A monolithically integrated transceiver chip must contain all layers necessary for signal generation and reception. The layers for the receiving MSM PD are epitaxially grown (by molecular beam epitaxy) on top of the VCSEL layers. A 200 nm-thick AlAs layer serves as an etch-stop and a barrier for the photo-generated carriers. The generation of the electron–hole pairs takes place in an undoped 1 µm-thick GaAs layer suitable for light

detection at 850 nm wavelength. This layer is separated from a dark current-reducing 40 nm $Al_{0.3}Ga_{0.7}As$ Schottky barrier by a 40 nm $Al_xGa_{1-x}As$ layer (linearly graded from $x = 0$ to 0.3) to minimize the energy band discontinuity which could hinder the transport of the light-induced carriers. The top GaAs layer serves as a protection layer to prevent $Al_{0.3}Ga_{0.7}As$ oxidation.

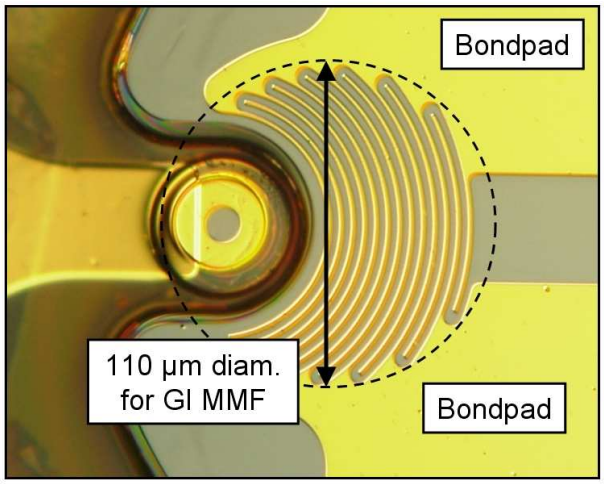

Fig. 1: Transceiver chip with 110 µm effective diameter, matching the 100 µm core diameter of the MMF indicated by the dashed circle. The 1.5 µm-wide PD fingers are separated by 2.5 µm interdigital spacings.

To access the highly p-doped cap layer of the VCSEL, the detector layers surrounding the resist-protected photodiode area are selectively removed by citric acid solutions. The process is terminated at the AlAs etch-stop layer which is subsequently removed by hydrofluoric acid. A dry-etch process is applied to define the VCSEL mesa, during which the photodiode is protected by photoresist. Subsequently, photolithographic steps are performed to put bondpads on the surface, thus allowing wire bonding for dynamic characterization. The 110 µm PD diameter is adapted to the 100 µm core diameter of the MMF that shall be centered in front of the transceiver chip (Fig. 1). The PD-to-VCSEL offset is a trade-off between coupling efficiency and remaining detector area.

3. Dark Currents of the MSM PDs

For dark current characterization, full-area circular MSM PDs with three different diameters are compared with each other, where all PDs have a finger width-to-spacing ratio of 1.5-to-2.5 µm. As expected, the dark current is lowest for the smallest PD and amounts to 0.5 nA at 5 V, as shown in Fig. 2. A further decrease of the dark current is expected if an antireflection (AR) coating is applied. The AR coating will passivate the surface and will also enhance the responsivity which currently amounts to about 0.35 A/W.

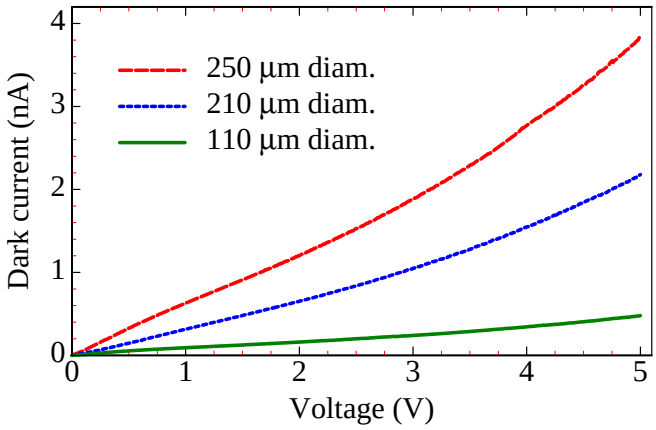

Fig. 2: Voltage-dependent dark currents of Tx/Rx MSM PDs for various PD diameters.

4. Coupling Efficiencies

Two types of chips have been fabricated, namely with 29 and 39 µm radial offset according to Fig. 1. For each chip, this eccentricity between VCSEL and PD results in two different lateral alignment tolerances. From Fig. 3 one obtains the tolerances for a 3 dB decay of coupled power. These are ±38 µm for 29 µm eccentricity and ±31µm for 39 µm offset. A constant 25 µm distance between chip and fiber has been used and the lateral displacement is performed in the direction normal to the PD–VCSEL axis. For displacement parallel to the axis, one finds −20 and +78 µm tolerances for 29 µm radial offset. With this eccentricity, the same maximum coupling efficiency of 89 % as in the case of a centered VCSEL (0 µm offset) is reached. On the other hand, the detector area is somewhat smaller compared to the 39 µm offset case.

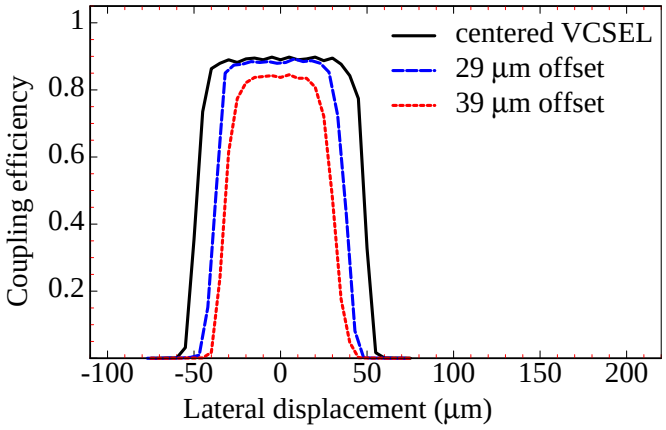

Fig. 3: Coupling efficiencies between VCSEL and fiber for various eccentricities, where a lateral displacement of 0 µm corresponds to a Tx/Rx chip position centered with respect to the fiber axis.

5. Digital Data Transmission

For bidirectional data transmission, one butt-coupled Tx/Rx chip at each fiber end is used, i.e. there are no optics between chip and fiber and the distance is smaller than 25 µm. Each transceiver chip consists of a 110 µm MSM PD and an oxide-confined VCSEL with 7 µm active diameter which has a lasing threshold of 1.6 mA and a 3 dB bandwidth exceeding 5 GHz. For maximized coupling efficiency, the 29 µm offset chip versions are employed. To optimize the photocurrent at both receiving photodiodes, a proper alignment of the Tx/Rx chips is necessary. The data transmission experiments are performed in half-duplex mode, i.e. one VCSEL is modulated while the second laser and the PDs have a constant bias. The eye diagrams for transmission of a non-return-to-zero pseudo-random bit sequence at 1 Gbit/s data rate over 100 m MMF show a clear eye opening both for $2^7 - 1$ and $2^{31} - 1$ word length, indicating error-free transmission (Fig. 4).

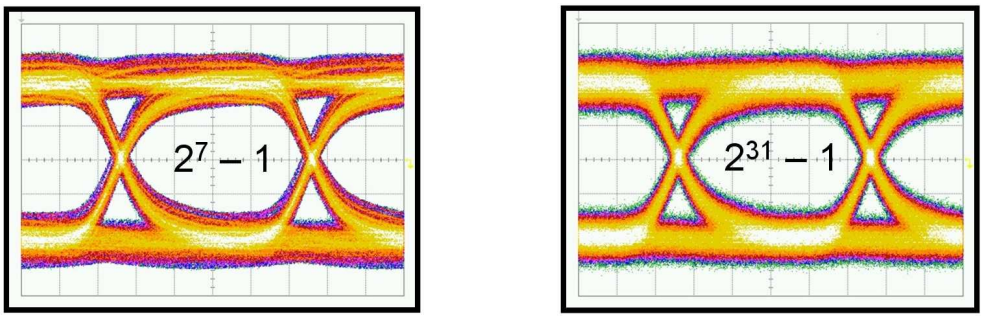

Fig. 4: Eye diagrams for bidirectional data transmission in half-duplex mode at 1 Gbit/s data rate for different word lengths over 100 m of 100 µm core diameter MMF from chip 1 to chip 2 (opposite case similar).

6. Conclusion

With novel miniaturized, monolithically integrated Tx/Rx chips, a 1 Gbit/s data rate, half-duplex mode optical link has been established using a two-side butt-coupled 100 m-long MMF. Such an approach is deemed to be attractive for cost-sensitive industrial and home networks.

References

[1] M. Stach, F. Rinaldi, M. Chandran, S. Lorch, and R. Michalzik, "Bidirectional optical interconnection at Gb/s data rates with monolithically integrated VCSEL–MSM transceiver chips", *IEEE Photon. Technol. Lett.*, vol. 18, pp. 2386–2388, 2006.

[2] M. Stach, F. Rinaldi, A. Gadallah, S. Lorch, I. Kardosh, P. Gerlach, and R. Michalzik, "1 Gbit/s bidirectional data transmission over 100 m graded-index glass optical fiber with monolithically integrated transceiver chips", in Proc. *Europ. Conf. on Opt. Commun., ECOC 2006*, vol. 3, pp. 493–494. Cannes, France, Sept. 2006.

Optical-Domain Four-Level Signal Generation by High-Density 2-D VCSEL Arrays

Hendrik Roscher, Philipp Gerlach, and Faisal Nadeem Khan

We propose a novel modulation scheme using three butt-coupled VCSELs per fiber for the generation of four-level signals in the optical domain. The information density, and hence spectral efficiency, is increased by using multiple VCSELs per 50 µm core diameter multimode fiber to generate more complex signals. First experiments are demonstrated using two VCSELs butt-coupled to the same standard glass fiber, each modulated with two-level signals to produce four-level signals at the photoreceiver. A four-level direct modulation of one VCSEL within a triple of devices produced first 20.6 Gbit/s (10.3 Gsymbols/s) four-level eyes, leaving two VCSELs as backup sources.

1. Introduction

We employ high-density high-speed vertical-cavity surface-emitting lasers (VCSELs) with wedge-shaped mesas in flip-chip integrated two-dimensional (2-D) arrays for the generation of four-level digital signals. Multi-level signals make better use of available bandwidth and thus increase fiber channel capacities.

This article first describes layout and structure of dense wedge-shaped high-speed VCSELs in 2-D arrays and gives their basic static and dynamic characteristics. The second part addresses several ways in which high-density VCSEL arrays may be utilized for different types of multi-level signal generation. A novel modulation scheme is proposed which enables four-level digital signal transmission by a two-level modulation of three separate lasers. All three VCSELs launch light into the same multimode fiber where three optical data streams add up to form a four-level signal. This scheme requires extended capabilities of drive electronics. Since only a regular bit pattern generator was available to us, two out of three lasers in a channel were modulated with two-level signals. The modulation parameters were adjusted such that the combined amplitudes of the two output beams produced a four-level signal.

The final section presents experiments where two separate bi-level data streams were combined in the electrical domain before addressing the laser. Similar to what was done in [1] using a single DFB laser, this resulted in a four-level direct modulation of only one of the three available VCSELs per fiber channel, leaving the two spare lasers as a possible backup in case of premature device failure.

2. Densely Packed Wedge-Shaped VCSELs in 2-D Arrays

Figure 1 shows a triple of wedge-shaped VCSELs. The design aims at closest possible center-to-center distances for mesa-isolated VCSELs while maintaining good thermal and dynamic characteristics of these substrate-removed devices. As the dry etch process utilizes the p-contact metallization as the etch mask, arbitrary mesa shapes are possible.

Figure 2 shows a top view of the completed flip-chip structure around the wedge mesas without solder balls. It is crucial for these substrate-removed lasers with substrate-side emission at 850 nm to place the solder balls at least partially on top of the mesas. This creates paths for efficient heat flow hence allowing for high-current VCSEL operation without excessive internal heating.

For development purposes, the cells within the 2-D arrays were not designed to be uniform but many dimensions were varied. A true-to-scale representation of the actual layout can be found in [2]. The mesa separations are between 3.8 and 1.8 µm. The oxidation length is below 4 µm. The biggest devices have active areas of 158 µm^2, corresponding to circular areas with 14 µm diameter. The active area of the smallest mesas is 38 µm^2 (7 µm diameter). This is the size that was used for some of the multi-level signal transmission experiments in this article.

Figure 3 gives the light–current–voltage (LIV) curves of the smallest VCSEL triple. The insets indicate the device dimensions and the measurement configuration. The VCSELs uniformly show a 2 mA lasing threshold, 3.1 mW maximum output power at 15 mA, 20 % differential quantum efficiency, and 77 Ω differential resistance.

The small-signal modulation characteristics of the same VCSELs are displayed in Fig. 4. As is evident from those curves, the flatness of the modulation response improves at high

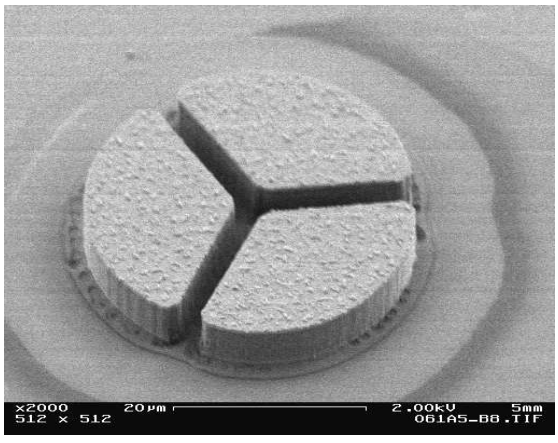

Fig. 1: SEM picture of three wedge-shaped VCSELs in one of 4 × 4 channels of an array after high-temperature oxidation in humid environment. The VCSELs exhibit smooth and vertical sidewalls and a self-aligned full size p-contact.

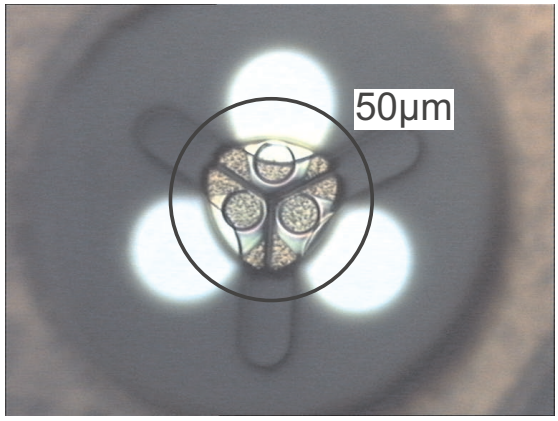

Fig. 2: Epitaxial-side view of completed close-spaced wedge VCSELs prior to solder deposition. The 50 µm circle indicates the relative position of the VCSELs with respect to a centered multimode fiber core.

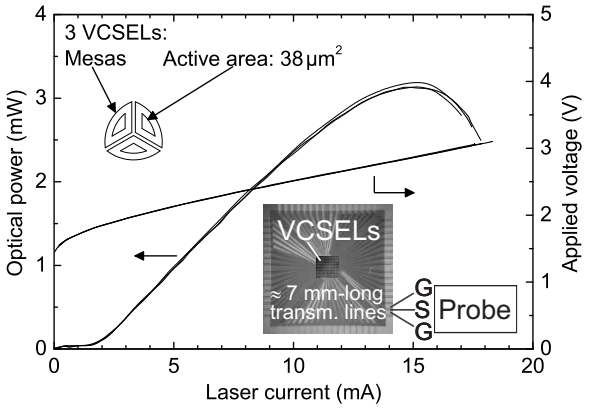

Fig. 3: LIV curves of three VCSELs within one cell of a $(4\times4)\times3$ array. The inset shows a true-to-scale representation of this pixel. The wedge-shaped 38 µm^2 active area corresponds to a 7 µm diameter circular current aperture.

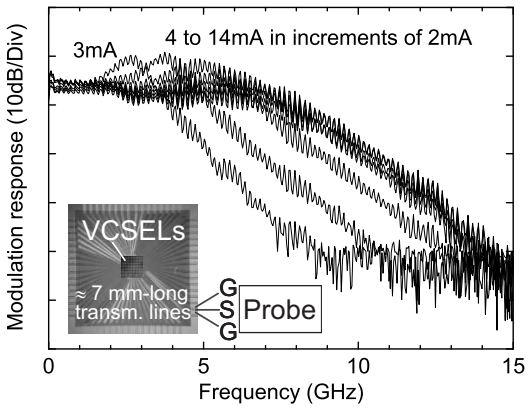

Fig. 4: Bias-dependent transfer functions of a VCSEL from the same pixel indicating 7.7 GHz maximum 3-dB corner frequency, held approximately in the range from 9 to 11 mA, while the 10-dB bandwidth for currents above 10 mA lies between 9.5 and 9.8 GHz.

drive currents. Flat laser transfer functions are important for a consistent signal level definition in large-signal modulation since they contribute to good overall system linearity, especially important when more than two signal levels are present in complex multi-level eye patterns. However, if heat extraction from the laser is insufficient, high power dissipation at high drive currents leads to high junction temperature, diminishing differential gain and quantum efficiency and accordingly the modulation response. Rise and fall times and extinction ratio of digital signals are immediately affected. It is found indispensable, especially for substrate-removed devices, to provide efficient passive cooling. This is done here by solder bonding the VCSELs directly to the mesas.

3. Four-Level Modulation

Dense flip-chip VCSEL integration opens up new avenues for the further increase in total data throughput of transmitter arrays, on one hand through built-in redundancy by keeping all parallel channels fully functional for a longer lifespan [3], on the other by increasing the complexity of the sent data in each channel. This section explores the latter possibility as some systems might benefit from the use of signals of higher complexity than the usual binary format. Expanding the symbol alphabet provides higher spectral efficiency.

Signals with four distinct amplitudes correspond to a four-symbol alphabet as opposed to two symbols available with binary transmission by simple on-off keying. The bit rate (twice the symbol rate) for a given bandwidth is doubled. Accordingly, a given data rate can be transmitted with half the line rate of an equivalent binary modulation format. Of course, extra functionality will be needed for the modulation and de-modulation of four-level signals. Dense transmitter arrays with three VCSELs instead of one launching into each fiber lend themselves to the optical-domain generation of four-level signals.

3.1 Four-level signal generation scheme using high-density VCSEL arrays

High-density VCSEL configurations accommodating three direct-bonded lasers in an area of less than one third the core of high-speed optimized multimode fibers were already demonstrated in [3]. Figure 5 illustrates how three VCSELs per fiber may be used to generate four-level signals. The nominally identical lasers are at the three vertices of an equilateral triangle and emit at the same wavelength. The fiber is perfectly aligned to the orthocenter of this triangle, ensuring equal coupling efficiencies. Precise passive fiber alignment can be achieved with the help of mechanical guides on the emission side of the VCSEL array. Development in this regard is currently underway.

In this scheme, every one of the three lasers can be operated with the optimum drive current and two-level modulation parameters, producing nominally identical amplitudes of two-level bit streams. If all bit streams are well synchronized, the optical intensities will add up to a four-level signal on the photoreceiver. On the right of Fig. 5, a model four-level eye pattern is used to associate each level with the required states of the identical VCSELs A, B, and C. For instance, the symbol `1 0` will be obtained if any two of the VCSELs are in `ON`-state while the third one is `OFF`.

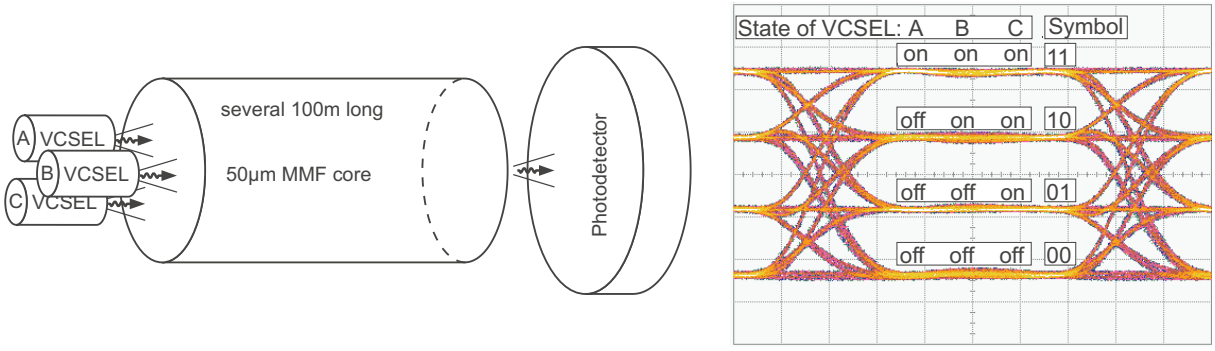

Fig. 5: Schematic showing one fiber channel of an optical link (left) illustrating the idea of four-level digital signal generation in the optical domain. The scheme uses three close-spaced VCSELs that are separately addressable and butt-coupled to one common 50 µm core diameter multimode fiber with equal coupling efficiencies. The optical signals add up at the photoreceiver, resulting in four distinct levels of intensity (right).

The lasers typically used for short-reach optical links have multimode emission. Since all three lasers are nominally identical, there exists a probability that two wavelengths involved are so close to each other that the beating product of co-polarized modes created at the photodetector may interfere with the signal spectrum. At $\lambda = 850\,\mathrm{nm}$, a wavelength difference of $\Delta\lambda = 25\,\mathrm{pm}$ will produce a beating product at $\Delta\nu = 10\,\mathrm{GHz}$, according to $\Delta\nu = (c/\lambda^2)\Delta\lambda$. Normally, fabrication tolerances lead to a certain degree of emission wavelength difference. If the wavelengths are still too close to each other, the VCSELs will have to be slightly modified to prevent beating products at frequencies within the signal spectrum. Beating products of larger wavelength differences are filtered out by the low-pass characteristic of the photodetector.

3.2 Experimental four-level signal generation in the optical domain

The above scheme of four-level signal generation requires additional capabilities of the drive electronics. As usual, when the information density is increased by means of more complex signals, additional "intelligence" is needed on the transmitting and receiving ends of the link. Due to the unavailability of such electronics in our first laboratory experiments, we followed an indirect approach for the optical generation of four-level signals using dense VCSELs.

According to Fig. 6, two of the three VCSELs in one pixel are fed with the DATA or $\overline{\texttt{DATA}}$ streams of a pattern generator. Additional attenuators are inserted to avoid the reflections from the pattern generator ports which otherwise degrade the signals. As the names of the ports imply, both data streams are not independent but one is the inverted version of the other. In order for the superposition of both pseudo-random bit sequences (PRBSs) to yield all four cases (both high, both low, one high the other low), one sequence needs to be delayed with respect to the other by integral multiples of one symbol duration at the given modulation rate. Instead of a variable delay line, a fixed delay was introduced in the form of an extra cable and the symbol rate adjusted for all measurements.

The amplitudes of the DATA and $\overline{\texttt{DATA}}$ streams can be selected independently. Each of the bit sequences are directly modulating one of the two lasers. The optical bit streams are coupled to the same fiber and detected by a fast photoreceiver. At the photoreceiver, the level separation of one signal must be exactly half of the second signal to give four evenly spaced levels. In the present setup, the VCSEL-to-fiber interface was found to be the weak link. There was no mechanical guide to the fiber and due to some instability of the setup it was found difficult to align the fiber such that both lasers coupled with equal efficiency.

Figure 7 shows a resulting four-level eye pattern for NRZ modulation with a $2^7 - 1$ word length PRBS. The symbol rate is 3.9 Gsymbols/s, corresponding to 7.8 Gbit/s. Both lasers

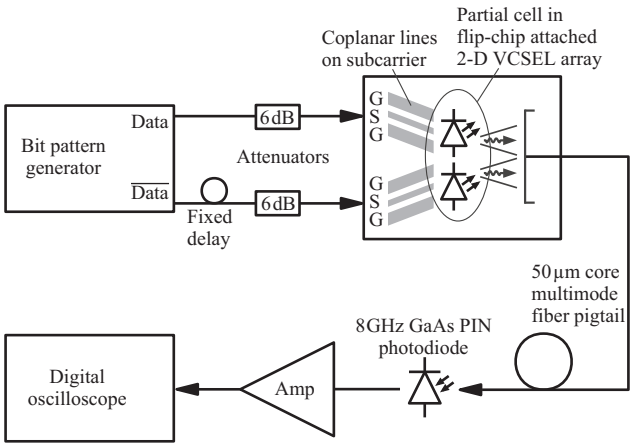

Fig. 6: Experimental setup using two of three available VCSELs per pixel butt-coupled to a standard multimode fiber for the optical-domain generation of four-level signals.

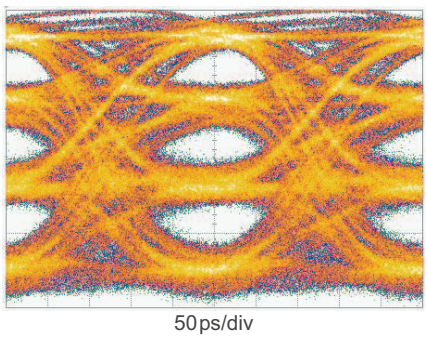

Fig. 7: 7.8 Gbit/s (3.9 Gsymbols/s) four-level eye pattern generated by superposition of two optical signals.

were biased at 8 mA and the peak-to-peak voltages were 2.0 V and 1.0 V. It is evident from the figure that although the eyes are open there is much room for improvement. The maximum achievable signal amplitude is split into four rather than only two levels, making four-level eyes much less robust with regard to noise and system nonlinearities. The particular lasers used for these experiments were circular in shape and had non-flat transfer functions with pronounced ripples from multiple reflections, much worse than the small signal curves in Fig. 4. This is believed to be the main reason for the degradation of the eye pattern. It also limits the bit rate achievable with four-level modulation to less than 10 Gbit/s. The lasers used here were shown to be capable of producing good-quality two-level eyes at 10 Gbit/s in Ref. [3]. Nevertheless, generation of four-level eyes can be beneficial to bandwidth-limited systems. This is true especially when electronics are available to implement the modulation scheme introduced in Sect. 3.1 along with improvements to the VCSEL-to-fiber interface.

3.3 Electrical-domain four-level signal generation experiments

We used a coupler to combine the two 2^7-1 word length NRZ PRBS two-level bit streams from the DATA and $\overline{\text{DATA}}$ ports in the electrical domain. The resulting four-level signal directly modulated one of three VCSELs. In this scheme, the remaining two VCSELs per array cell are left as backup devices in case of VCSEL failure. Figure 8 shows the setup which is similar to the one in the previous section, only that the two bit streams are combined before reaching the VCSEL array. With this method, higher modulation rates were achieved than with the combination of optical bit streams.

Figure 9 shows a four-level eye at 20.6 Gbit/s (10.3 Gsymbols/s) obtained for 12 mA bias current. The values in the two branches were $V_{\text{pp1}} = 1.63$ V, $\alpha_1 = 10$ dB and $V_{\text{pp2}} = 2.00$ V, $\alpha_2 = 6$ dB, respectively. The modulated optical signal is detected by an 8 GHz PIN photodiode. In the case of the eye pattern shown, the electrical signal was filtered by a 7 GHz low-pass filter inserted between amplifier and oscilloscope. It is clear from the

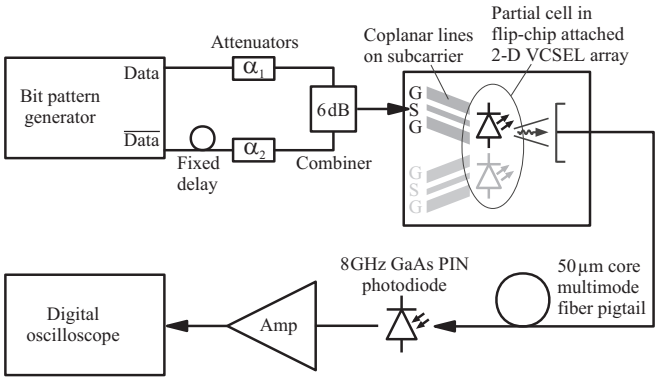

Fig. 8: Experimental setup for the electrical-domain combining of two-level signals of different amplitudes from the DATA and $\overline{\text{DATA}}$ ports. The electrical four-level signal directly modulates one of three VCSELs in a pixel.

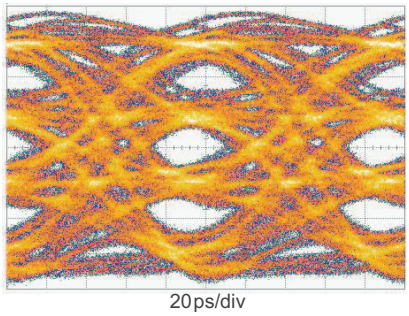

Fig. 9: 20.6 Gbit/s (10.3 Gsymbols/s) four-level eye pattern generated in the electrical domain by superimposing the electrical signals.

eye pattern that there is a lack of symmetry. Slow rise and fall times as well as system nonlinearity strongly reduce the eye openings. This is nevertheless the first time that such extremely close-spaced flip-chip bonded VCSELs in 2-D arrays have been used for the generation of four-level eyes.

4. Conclusion

Ultra-dense wedge-shaped VCSELs showed the ability for single-device four-level modulation at 10.3 Gsymbols/s (20.6 Gbit/s), as well as for the simultaneous operation of two densely spaced mesa-isolated VCSELs at 3.9 Gbit/s each, producing a combined 3.9 Gsymbols/s. A higher VCSEL resonance frequency would have helped to increase the eye openings by shorter rise and fall times. The VCSEL-to-fiber interface limited the performance in the mode of four-level generation in the optical domain. This can be improved by the introduction of mechanical fiber guides to ensure alignment as well as proper index matching to prevent backreflections.

Acknowledgment

Special thanks to Faisal Imam and Alexander Weigl who worked with me toward their theses during this last year. Their many contributions are much appreciated.

References

[1] A. Wonfor, R.V. Penty, I.H. White, K. White, A.E. Kelly, and C. Tombling, "Uncooled 40 Gb/s 4-level directly modulated laser source for datacoms applications", in *Semiconductor Lasers and Laser Dynamics*, D. Lenstra, G. Morthier, T. Erneux, M. Pessa (Eds.), Proc. SPIE 5452, pp. 562–570, 2004.

[2] H. Roscher, P. Gerlach, F.N. Khan, A. Kroner, M. Stach, A. Weigl, and R. Michalzik, "Toward more efficient fabrication of high-density 2-D VCSEL arrays for spatial redundancy and/or multi-level signal communication", in *Micro-Optics, VCSELs, and Photonic Interconnects II: Fabrication, Packaging, and Integration*, H. Thienpont, M.R. Taghizadeh, P. Van Daele, J. Mohr (Eds.), Proc. SPIE 6185, pp. 61850V-1–12, 2006.

[3] H. Roscher, M. Bou Sanayeh, S.B. Thapa, and R. Michalzik, "VCSEL arrays with redundant pixel designs for 10 Gbit/s 2-D space-parallel multimode fiber transmission", in Proc. *31st Europ. Conf. on Opt. Commun., ECOC 2005*, vol. 3, pp. 687–688. Glasgow, Scotland, UK, Sept. 2005.

High-Performance Single Fundamental Mode AlGaAs VCSELs with Mode-Selective Mirror Reflectivities

Andrea Kroner

We present inverted surface relief vertical-cavity surface-emitting lasers (VCSELs) showing a side-mode suppression ratio above 30 dB up to maximum optical output powers of 6.3 mW and differential quantum efficiencies exceeding 90 %. An evaluation of 160 relief devices on a sample incorporating graded layers yields 157 lasers with single-mode output powers of at least 2.9 mW, proving the high effectiveness of the technique despite the comparatively simple manufacture.

1. Introduction

Oxide-confined VCSELs emitting multiple transverse modes are commonly employed for short-distance data transmission. However, with the emergence of new applications like optical spectroscopy or optical sensing, there is an increasing demand for transverse single-mode VCSELs [1]. In standard devices, single-mode emission can only be achieved for small oxide apertures, involving limited maximum output power, increased ohmic resistance and reduced lifetime. More advantageous alternatives to enhance single-mode operation have been demonstrated, like long monolithic cavity VCSELs [2], antiresonant reflecting optical waveguide VCSELs [3] and VCSELs with a triangular holey structure [4]. The latter produced a record-high single-mode output power of 7.5 mW with 30 dB side-mode suppression ratio (SMSR), however, with multi-lobed far-field patterns.

In the so-called surface relief technique, an annular etch of the laser output facet lowers the mirror reflectivity particularly for higher order modes, which show higher optical intensities outside the device centre. The resulting differences in threshold gain then strongly favour the fundamental mode. In an advanced approach, the top Bragg mirror is terminated by an additional quarter-wave antiphase GaAs layer in order to decrease its reflectivity significantly. By removing the antiphase layer only in the centre of the output facet, the threshold gain for the fundamental mode is then selectively decreased. This so-called inverted relief technique requires a less precise etch depth control and higher modes experience additional absorption by the GaAs antiphase layer for emission wavelengths smaller than about 860 nm [2]. The main advantage compared to the above methods is the relatively low fabrication complexity. Furthermore, comparatively small degradations of threshold current, differential resistance or far-field pattern are observed. A high output power of 6.1 mW from a single inverted surface relief VCSEL with continuous single-mode operation and a SMSR above 30 dB has been reported [5]. Even a single-mode power of 6.5 mW was reported, however, the corresponding device showed no continuous

single-mode operation. Instead, a higher-order mode was lasing at about three times the threshold current before the VCSEL was single-mode again at higher currents [5]. Such an instability of the modal behavior questions the reliability of the mode-selective effect induced by the inverted surface relief. Therefore, a statistical investigation of this mode control technique appears to be appropriate.

In this article we investigate a large quantity of inverted relief VCSELs, demonstrate even higher output power and show much improved single-mode properties compared to reference devices for a wide range of relief diameters [6].

2. Device Layout and Fabrication

Figure 1 shows a schematic cross-section of the VCSEL structure and an optical microscope top view of a finished device. The epitaxial layers are designed for 860 nm emission wavelength and were grown by molecular beam epitaxy. The resonator is formed by 23 AlGaAs layer pairs in the p-doped top Bragg mirror and 39.5 pairs in the n-type bottom mirror. The active region consists of three GaAs quantum wells in a one-wavelength thick inner cavity and an adjacent AlAs layer is used for current confinement by selective oxidation. A centre circular opening is etched into the additional quarter-wave antiphase GaAs layer using citric acid. Exact alignment of surface relief and mesa was ensured by applying common optical lithography with a self-alignment technique [2]. Finally, a standard VCSEL process sequence was used to complete the devices, including oxidation and passivation. For current injection a backside n-contact and a p-contact ring with an aperture of 16 µm were deposited. Beside the relief devices also reference lasers were fabricated by etching the antiphase layer across the whole output facet.

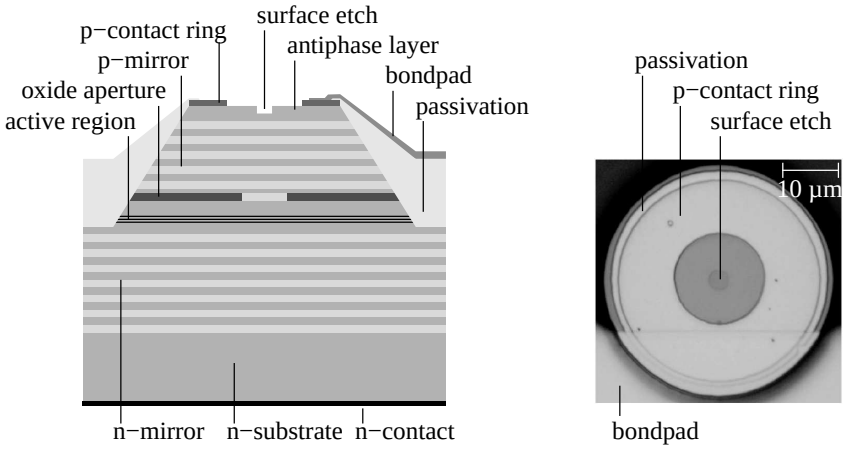

Fig. 1: Cross-section of the device layout (left) and optical microscope top view of a finished VCSEL (right).

3. Device Characterisation

Figure 2 displays the output characteristic of a reference device with an oxide aperture of about 6 µm and its optical spectrum at different driving currents. The laser shows a threshold current of 0.7 mA, a maximum output power of 6.8 mW (measured with an integrating sphere at room temperature) and a differential quantum efficiency of 44 %. Even for small currents close to threshold, no single-mode operation with a SMSR of more than 30 dB is observed and the spectrum gets highly multimode for higher currents. Figure 3 shows the same measurements for a nearby laser on the same sample, which is nominally identical except for a surface relief with a diameter of 3.3 µm and an etch depth of 58 nm, as determined by atomic force microscope measurements. The relief device shows a clearly increased threshold current of 3.1 mA due to the effectively decreased mirror reflectivity. On the other hand, the differential quantum efficiency has increased to 92 %, supported by the supply of carriers from the outer part of the active layers underneath the unetched region. The optical spectra confirm a SMSR exceeding 30 dB up to thermal rollover. The laser delivers a maximum single-mode output power of 6.3 mW at a driving current of 12 mA, which is to our knowledge the highest reported value for a relief VCSEL with continuous single-mode operation. Both devices have similar, low differential resistances of 89 Ω (reference) and 84 Ω.

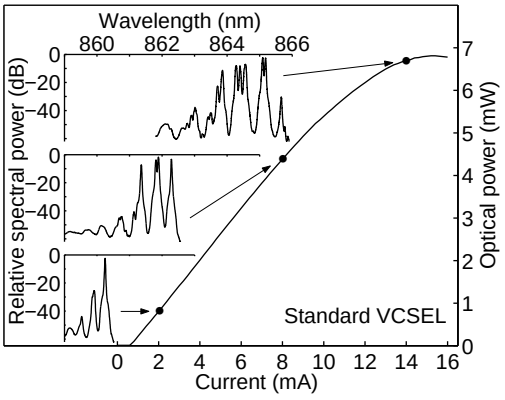

Fig. 2: Output characteristic of a 6 µm active diameter reference VCSEL without relief.

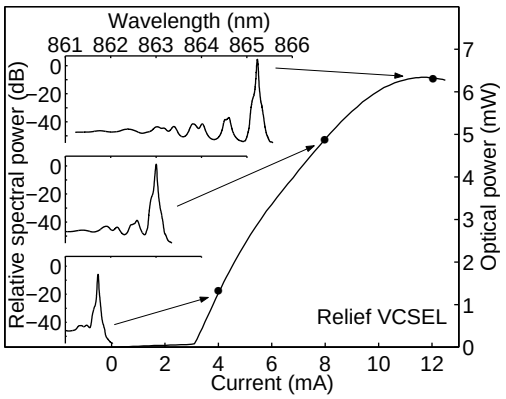

Fig. 3: Output characteristic of a 6 µm active diameter VCSEL with 3.3 µm relief diameter.

Figures 4 and 5 show the far-field patterns for a reference and a relief device at high currents, where both show similar output powers (6.6 and 6.3 mW, respectively). The enhanced single-mode operation of the relief device results in a Gaussian-shaped beam profile and a strongly decreased full-width-at-half-maximum (FWHM) of 7.6 ° compared to 21.3 °. Almost no side-lobes are observed.

Beside the 6 µm oxide apertures, also relief VCSELs with active diameters of 4 and 8 µm are contained in the investigated sample. With both aperture sizes, enhanced single-mode operation is achieved, however, the smaller devices show less output power, owing to the smaller active area. The larger devices provide similar single-mode output power as the 6 µm VCSELs, but show much higher threshold currents due to decreased optical guiding of the fundamental mode. Also lasing of a higher-order mode close to threshold

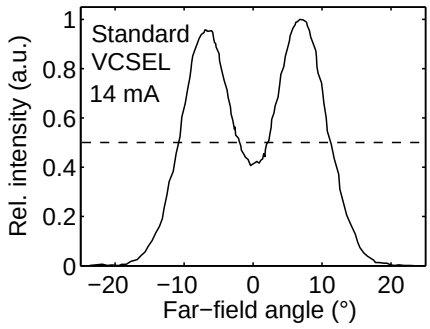

Fig. 4: Far-field pattern of a 6 µm active diameter reference VCSEL without relief at 14 mA driving current.

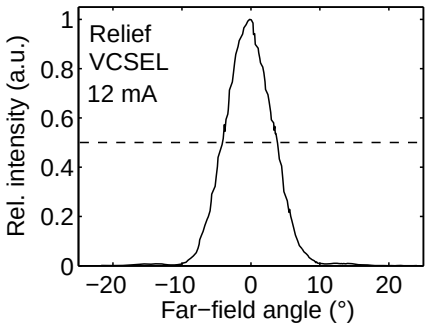

Fig. 5: Far-field pattern of a 6 µm active diameter VCSEL with 3.0 µm relief diameter at 12 mA driving current.

could be observed. Therefore we concentrated on the 6 µm active diameter lasers for the investigations to follow.

4. Statistic Investigations

To substantiate the mode-selective effect of the surface relief, a significant number of VCSELs on the same sample were characterized. The sample is subdivided into unit cells, each containing four relief devices and two reference devices, which are separated by 250 µm. The surface reliefs have nominal diameters of 3.0, 3.2, 3.4 and 3.6 µm. However, deviations of at least ±0.1 µm have to be taken into consideration, especially when comparing distant positions on the sample. To allow statistical conclusions, 75 reference devices and 160 relief devices from 44 unit cells were investigated. Due to a gradient in layer thicknesses, originating from the epitaxial growth process, the cavity resonance frequency varies over the sample, leading to emission wavelengths ranging from 820 to 870 nm. Since the quantum wells are optimised for 860 nm emission, lasers with short wavelengths experience less gain, resulting in lower output powers.

Figure 6 shows a schematic top view of the sample, where each rectangle represents one laser and its color indicates the maximum single-mode output power. The measurements were performed at room temperature, and a collimating objective together with a silicon photodiode were used for detection, incurring losses of about 3 %. Defective devices mainly have a completely metallised output facet owing to fabrication imperfections and are not considered in the evaluation. Only one of the reference devices provides a single-mode output power of more than 1.0 mW, whereas 65 % show no single-mode emission at all. On the other hand, 48 % of the relief VCSELs have single-mode powers of at least 5.0 mW, 3 % emit not less than 6.0 mW. Highest output power is found in the region of high gain (top right in Fig 6). A minimum single-mode output power of 2.9 mW is achieved for 98 % of the relief VCSELs. The missing devices show no single-mode emission due to processing errors resulting in a too large oxide aperture.

Concerning the relief diameter, higher single-mode powers are commonly obtained for smaller reliefs, since devices with large reliefs tend to multimode emission at high currents.

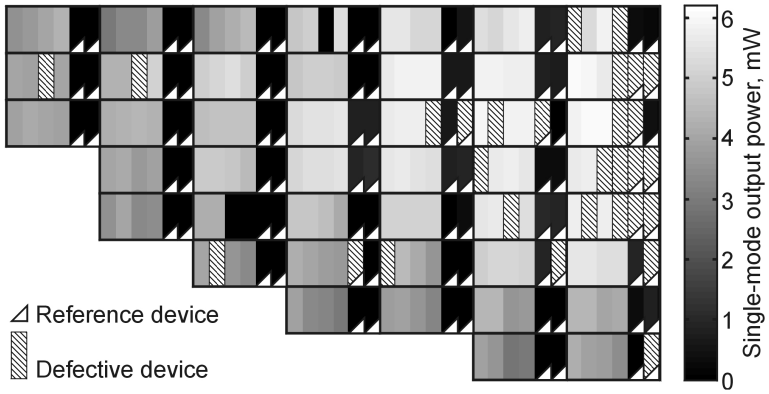

Fig. 6: Schematic top view of the examined sample showing the distribution of maximum single-mode output powers. Each rectangle refers to one laser.

Since the varying detuning of the sample has a much stronger influence on the device performance than the relief variations, a direct comparison of devices is only reasonable if their distance is sufficiently small. As an example, Fig 7 shows the output characteristics of four adjacent VCSELs of the same unit cell with surface reliefs of 3.6, 3.4, 3.2 and 3.0 µm diameter. The 3.6 and 3.4 µm devices are single-mode only up to driving currents of 10.9 and 12.3 mA, respectively, as indicated by kinks in the power curves. Therefore, their single-mode output power is limited to 5.4 and 5.5 mW, respectively. For the 3.2 µm relief size, no higher-order mode starts to lase and a maximum single-mode output power of 5.7 mW is reached. However, at the same time, the threshold current increases by 0.6 mA, due to the reduced overlap between the fundamental mode and the surface etch. So a further reduction of the relief to 3.0 µm eventually diminishes the output power by thermal effects.

The scaling behavior described above can be generally observed and in most cases the maximum single-mode output power within a unit cell was found for the 3.0 or 3.2 µm relief diameter devices. Exceptions are mainly located at the upper left region of the sample, which is attributed to slightly larger oxide apertures in this area. The suitability of the smaller relief sizes is also demonstrated in the lower part of Fig 8. Here, the maximum single-mode output power of each working relief device is normalized to the single-mode output power of the nearest VCSEL with 3.6 µm relief diameter in order to eliminate the influence of the varying resonance frequency. The figure shows the mean increase in single-mode power for devices with the same nominal relief size in dependence on the relief diameter. On average, a 4 % higher output power is achieved by the VCSELs with 3.2 µm relief diameter compared to the devices with the largest relief. In the upper part of Fig 8, the same analysis was done for the threshold current of the relief VCSELs. Here, a strong increase of the threshold with decreasing relief diameter at a rate of approximately 44 %/µm is observed.

Although the single-mode output power is significantly increased by the inverted surface relief technique, a stable polarisation of the fundamental mode is not ensured. This is due to the fact that the relief itself is circular and no further modifications were applied to

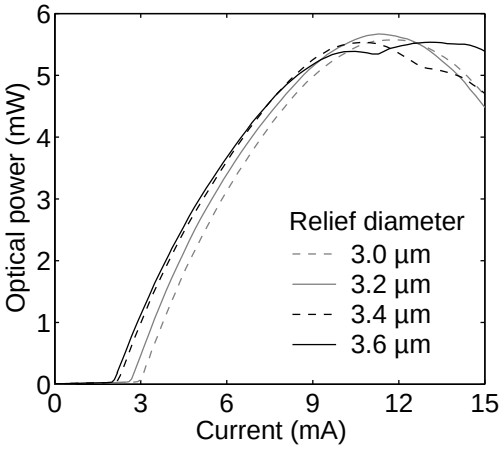

Fig. 7: Light output curves of four adjacent VCSELs of the same unit cell with varying surface relief diameter.

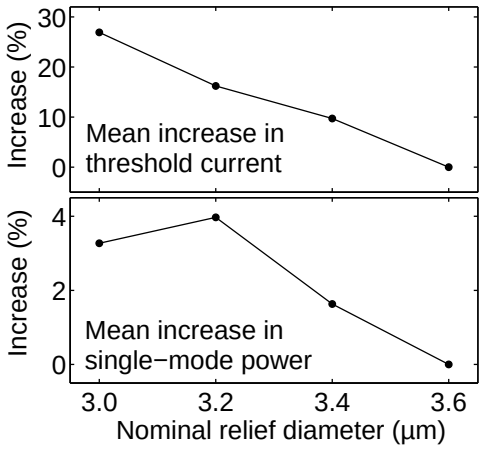

Fig. 8: Mean increase in threshold current (top) and single-mode output power (bottom), normalized to the devices with 3.6 µm relief diameter.

break the rotational device symmetry. However, by combining the relief with an etched linear surface grating, reliable polarisation control is achieved in addition to enhanced single-mode output power [7, 8]. The optimum device parameters determined in this paper can therefore serve as a basis for a further increase of the single-mode output power of grating relief VCSELs.

5. Conclusion

We have fabricated VCSELs with an inverted surface relief using standard optical lithography and wet etching, producing devices with continuous single-mode operation of up to 6.3 mW, a SMSR above 30 dB and FWHM far-field angles below 8 °. Reference devices show no or only weak single-mode emission. The examination of 160 relief devices on an inhomogeneous sample yielded 157 VCSELs with single-mode output powers above 2.9 mW. Among these, 76 devices delivered more than 5 mW, and best performance was generally observed for devices with 3.2 µm relief diameter and 6 µm oxide apertures. These results strongly confirm the suitability of the inverted surface relief technique for single-mode enhancement, since it is effective and reliable as well as relatively simple in fabrication.

Acknowledgment

We wish to thank the German National Academic Foundation for supporting the Ph.D. thesis associated with this work and former VCSEL group member H.J. Unold for mask design.

References

[1] D. Wiedenmann, M. Grabherr, R. Jäger, and R. King, "High volume production of single-mode VCSELs", in *Vertical-Cavity Surface-Emitting Lasers X*, C. Lei, K.D. Choquette (Eds.), Proc. SPIE 6132, pp. 613202-1–12, 2006.

[2] H.J. Unold, S.W.Z. Mahmoud, R. Jäger, M. Golling, M. Kicherer, F. Mederer, M.C. Riedl, T. Knödl, M. Miller, R. Michalzik, and K.J. Ebeling, "Single-mode VCSELs", in *Vertical-Cavity Surface-Emitting Lasers VI*, C. Lei, S.P. Kilcoyne (Eds.), Proc. SPIE 4649, pp. 218–229, 2002.

[3] D. Zhou and L.J. Mawst, "High-power single-mode antiresonant reflecting optical waveguide-type vertical-cavity surface-emitting lasers", *IEEE J. Quantum Electron.*, vol. 38, no. 12, pp. 1599–1606.

[4] A. Furukawa, S. Sasaki, M. Hoshi, A. Matsuzono, K. Moritoh, and T. Baba, "High-power single-mode vertical-cavity surface-emitting lasers with triangular holey structure", *Appl. Phys. Lett.*, vol. 85, no. 22, pp. 5161–5163, 2004.

[5] Å. Haglund, J.S. Gustavsson, J. Vukusic, P. Modh, and A. Larsson, "Single fundamental mode output power exceeding 6 mW from VCSELs with a shallow surface relief", *IEEE Photon. Technol. Lett.*, vol. 16, no. 2, pp. 368–370, 2004.

[6] A. Kroner, F. Rinaldi, J.M. Ostermann, and R. Michalzik, "High-performance single fundamental mode AlGaAs VCSELs with mode-selective mirror reflectivities", *Optics Communications*, vol. 270, no. 2, pp. 310–313, 2007.

[7] J.M. Ostermann, P. Debernardi, C. Jalics, and R. Michalzik, *IEEE J. Select. Topics Quantum. Electron.*, vol. 11, no. 1, pp. 982–989, 2005.

[8] J.M. Ostermann, F. Rinaldi, P. Debernardi, and R. Michalzik, "VCSELs with enhanced single-mode power and stabilized polarization for oxygen sensing", *IEEE Photon. Technol. Lett.*, vol. 17, no. 11, pp. 2256–2258, 2005.

High-Performance AlGaAs-Based VCSELs Emitting in the 760 nm Wavelength Range

Fernando Rinaldi, Johannes Michael Ostermann, and Andrea Kroner

Vertical-cavity surface-emitting lasers (VCSELs) showing continuous-wave operation with emission wavelengths ranging between 717 and 790 nm have been fabricated. The samples are grown by solid source molecular beam epitaxy on GaAs substrates and are entirely based on the AlGaAs material system. A maximum single-mode output power of 2.0 mW is obtained at 754 nm wavelength by using the inverted surface relief technique.

1. Introduction

In recent years, VCSELs emitting in the 760 nm wavelength range have attracted considerable attention for different applications, among which the most important is oxygen sensing [2, 3]. 780 nm VCSELs incorporating AlGaAs quantum wells (QWs) with only 200 µA threshold current and almost 1.1 mW single-mode output power were already demonstrated almost a decade ago [4]. Nevertheless for 760 nm emission wavelength it was difficult to obtain devices with output powers in the milliwatt range. The AlGaAs QW material system was claimed to be responsible for the low performance of these devices and novel QW materials were proposed, for example AlInGaAs/AlGaAs [5]. Despite of this, in the present article we show that the AlGaAs material system can be successfully employed to produce high-performance short-wavelength VCSELs [1].

2. Layer Structure

The epitaxial structure was grown on GaAs (001)-oriented substrates using a Riber 32P molecular beam epitaxy (MBE) system. Silicon and carbon were used for n- and p-type doping, respectively, where the latter was injected as gaseous CBr_4. The active region is composed of three 8 nm thick $Al_{0.14}Ga_{0.86}As$ QWs separated by 10 nm thick $Al_{0.40}Ga_{0.60}As$ barriers. For current confinement, a 25 nm thick AlAs oxidation layer was placed above the QW region in a node of the calculated standing wave pattern. The distributed Bragg reflectors (DBRs) are graded in composition and doping concentration in order to minimize the optical absorption and to decrease the electrical resistance. The n-doping level is varied between $1.3 \cdot 10^{18}$ and $2.7 \cdot 10^{18}\,\mathrm{cm}^{-3}$, while the p-doping is varied between $2.1 \cdot 10^{18}$ and $5.6 \cdot 10^{18}\,\mathrm{cm}^{-3}$. Moreover δ-doping is included both in the n- and the p-side in the vicinity of the standing wave nodes. The mirrors incorporate 40.5 n-type and 26 p-type layer pairs. The highest refractive index in the DBRs is given by $Al_{0.30}Ga_{0.70}As$ layers which exhibit an absorption edge at 690 nm with a sufficient safety

margin to avoid absorption at the emission wavelength. The alloy $Al_{0.93}Ga_{0.07}As$ is the lowest index material in the DBRs, except for the first 32 n-type pairs consisting of AlAs to enhance the refractive index contrast. This composition provides enough tolerance for the subsequent mesa etching process to avoid the oxidation of the AlAs layers in the n-DBR. The p-contact layer consists of 14 nm thick GaAs with a carbon doping concentration exceeding $10^{20}\,cm^{-3}$. The growth temperature was 580 °C during the entire process. In addition, an extra top quarter-wave ($\lambda/4$) layer was grown, yielding antiphase reflection from the semiconductor–air interface. This extra layer is partially or totally removed at the output facet, as explained in detail in Sect. 4.

2.1 Wafer-Level Characterisation

Since the growth rate in the given MBE system exhibits a gradient along the radial direction, resonance wavelengths between 717 and 790 nm were obtained on the same wafer. Figure 1 shows the reflectivity spectra for samples without (curve a) and with the $\lambda/4$ antiphase layer (curve b). The measurements were performed at wafer positions where the resonance dips occur at approximately 765 nm. The sample with the antiphase layer has a reduced resonance reflectivity of 65 %. The curve (c) shows the photoluminescence spectrum corresponding to curve (b) under 512 nm argon ion laser excitation after removal of the top p-doped DBR by wet etching. The photoluminescence spectra are less sensitive to the thickness gradient over the wafer than the resonance wavelengths, because the given variations in the QW thickness do not significantly shift the energy levels. Moreover the aluminium composition is almost constant over the wafer. The photoluminescence peak is located at approximately 748 nm wavelength. This value was optimised to obtain the best performance for 760 nm laser emission at room temperature.

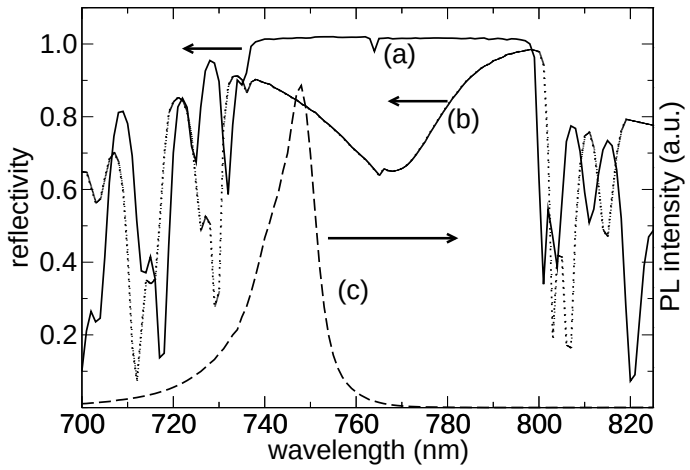

Fig. 1: Reflectivity spectra for standard (a) and for antiphase (b) samples. Photoluminescence spectrum of an etched sample (c).

3. Laser Fabrication

The fabrication process starts with wet mesa etching. The etching process is stopped below the 25 nm thick AlAs oxidation layer. Circular mesas with different diameters between 48 and 54 µm were defined. Oxidation in a N_2/H_2O atmosphere at a temperature of 400 °C resulted in oxide apertures ranging between 2 and 8 µm. On the top side TiPtAu ring contacts and on the bottom side broad-area GeAuNiAu contacts were deposited. The lasers were tested on wafer. The term standard device refers to a VCSEL obtained after etching the extra $\lambda/4$ layer. On the other hand, devices with superior single-mode performance can be obtained by removing this layer only in a center circular region of a few micrometer diameter. The high top mirror reflectivity for the fundamental mode will thus be restored. In contrast, higher order modes will be strongly suppressed since they experience a reduced reflectivity and additional absorption in the $\lambda/4$ thick GaAs layer. These devices are called inverted circular relief VCSELs. Instead of etching only a circular disk into the central region of the extra $\lambda/4$ GaAs layer, one can also implement a surface grating with the same diameter. With these inverted grating relief VCSELs, not only an enhancement of the single-mode performance but also a stable polarisation can be achieved. More details on these devices are found in [6]. In the following we will focus on standard VCSELs and inverted circular relief VCSELs.

4. Results

Figure 2 presents the light–current–voltage (L–I–V) characteristics of a standard VCSEL with 8 µm oxide diameter. The laser shows a threshold current of 1.5 mA and a differential quantum efficiency of 35 %. The maximum output power of 5.6 mW is reached at 16 mA current. The inset of Fig. 2 displays the optical spectrum at 17 mA, indicating transverse multimode operation at approximately 768 nm emission wavelength. In Fig. 3 the L–I–V

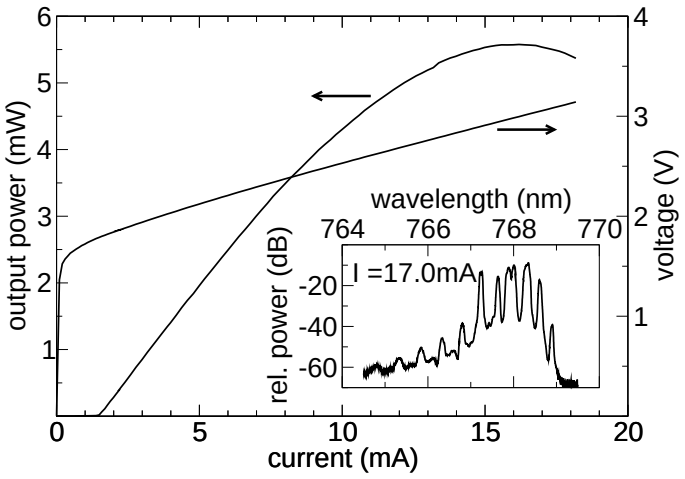

Fig. 2: L–I–V characteristics and spectrum (inset) of a standard multimode VCSEL with an active diameter of 8 µm.

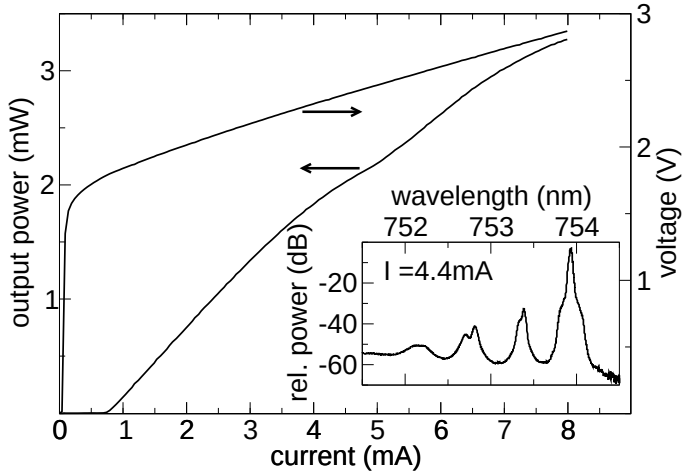

Fig. 3: L–I–V characteristics of a 4 µm active diameter VCSEL with a 3 µm diameter inverted relief, which is single-mode up to 4.4 mA current (see spectrum in the inset).

characteristics of a 4 µm active diameter VCSEL with a 3 µm diameter inverted circular relief shows a threshold current of 0.7 mA and single-mode operation up to 2.0 mW with a side-mode suppression ratio of at least 30 dB, as shown by the spectrum recorded at 4.4 mA. A kink in the output power curve—here at about 5 mA current—is typical for such VCSELs when higher modes appear. Besides emission wavelengths around 760 nm, laser operation could also be observed for wavelengths far away from the gain maximum, due to the mentioned radial gradient. Figure 4 depicts the characteristics of a device with an inverted circular relief of 3 µm diameter and 4 µm oxide aperture lasing at 720 nm in multimode operation, as evidenced by the spectrum taken at 6.6 mA. Despite the large detuning between the gain maximum and the cavity resonance of more than 40 nm, the

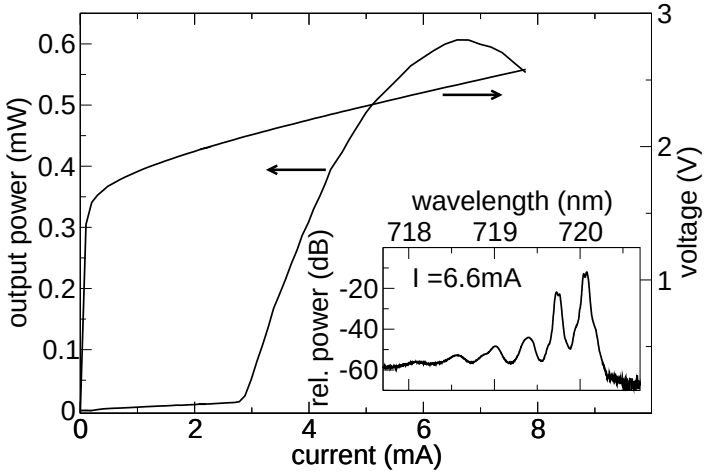

Fig. 4: L–I–V characteristics and spectrum (inset) of a 3 µm diameter inverted relief device with 4 µm active diameter, lasing at 720 nm.

device still shows 16 % differential quantum efficiency, 0.6 mW maximum output power and 2.8 mA threshold current. The sample also contains devices lasing at 717 nm with a maximum output power of 0.3 mW.

The wavelength dependences of the maximum single-mode output power and of the threshold current are shown in Figs. 5 and 6 for standard and inverted relief VCSELs, respectively. For easy comparison, the same scale is used. Both types of VCSELs have an oxide aperture diameter of 4 µm. The relief diameter is 3 µm and its depth is 64 nm. As can be inferred from the minima of the threshold currents of both types of lasers, the best spectral overlap of the gain curve and the cavity resonance is given for emission wavelengths between 760 and 780 nm. For smaller or larger emission wavelengths, the threshold current increases due to detuning between gain peak and cavity resonance. The magnitudes of the threshold currents and their wavelength dependences are very comparable for both types of lasers. The minimum threshold current is found in the 771 to 778 nm range and is 420 µA in both cases. In contrast, the maximum single-mode output powers of standard and inverted relief VCSELs differ significantly. On average, the power is approximately doubled for the inverted circular relief lasers which clearly demonstrates the effectiveness of this technique. Close to 760 nm wavelength, i.e. in the spectral region important for oxygen sensing, standard devices show about 0.9 mW power, whereas more than 1.9 mW are obtained from the relief VCSELs.

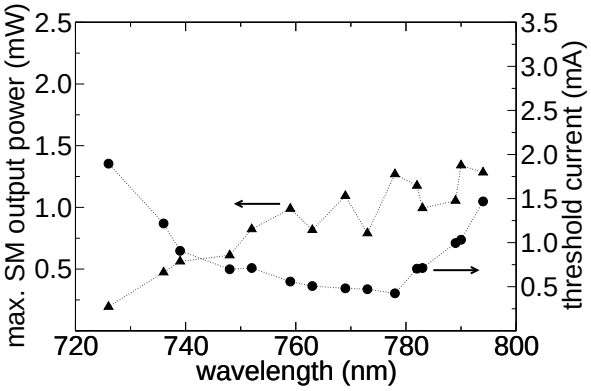

Fig. 5: Wavelength dependence of the maximum single-mode (SM) output power and of the threshold current of standard VCSELs with about 4 µm active diameter.

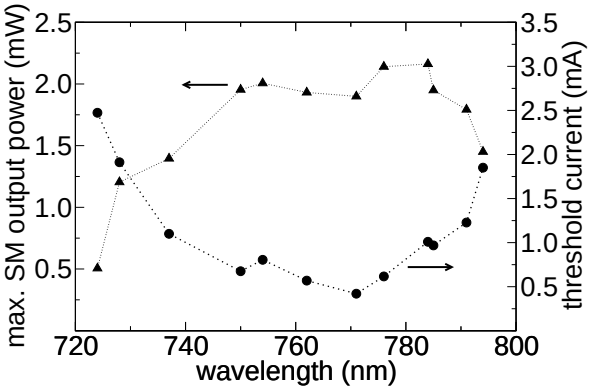

Fig. 6: Wavelength dependence of the maximum single-mode power and of the threshold current of inverted relief VCSELs with 3 µm relief diameter and about 4 µm active diameter, to be compared with Fig. 5.

5. Conclusion

We report multimode VCSELs with a high optical output power of 5.6 mW at 768 nm emission wavelength and single-mode VCSELs showing a high maximum output power of 2.0 mW at 754 nm wavelength. Finally we demonstrate strongly detuned devices operating at wavelengths slightly shorter than 720 nm. To the best of our knowledge, this is the shortest wavelength ever reported for continuous-wave AlGaAs-based VCSELs.

Consequently, in this way we have confirmed the possibility of using the well-known AlGaAs/GaAs system for VCSELs in this wavelength range.

Acknowledgment

We wish to thank the Ministry of Economics of the State of Baden-Württemberg and the German Research Foundation (DFG) for funding this work.

References

[1] F. Rinaldi, J.M. Ostermann, A. Kroner, and R. Michalzik, "High-performance AlGaAs-based VCSELs emitting in the 760 nm wavelength range", *Optics Communications*, vol. 270, no. 2, pp. 310–313, 2007.

[2] H.P. Zappe, M. Hess, M. Moser, R. Hövel, K. Gulden, H.P. Gauggel, and F. Monti di Sopra, "Narrow-linewidth vertical-cavity surface-emitting lasers for oxygen detection", *Appl. Opt.*, vol. 39, no. 15, pp. 2475–2479, 2000.

[3] T. Leinonen, J. Viheriälä, J. Lyytikäinen, P. Leinonen, M. Dumitrescu, and M. Pessa, "MBE-grown 760-nm VCSELs for oxygen sensing", in Proc. *Conf. on Lasers and Electro-Optics Europe, CLEO/Europe 2005*, paper CB-15-MON. Munich, Germany, June 2005.

[4] H.-E. Shin, Y.-G. Ju, J.-H. Shin, J.-H. Ser, T. Kim, E.-K. Lee, I. Kim, and Y.-H. Lee, "780 nm oxidised vertical-cavity surface-emitting lasers with $Al_{0.11}Ga_{0.89}As$ quantum wells", *Electron. Lett.*, vol. 32, no. 14, pp. 1287–1288, 1996.

[5] J. Gilor, I. Samid, and D. Fekete, "Threshold current density reduction of strained AlInGaAs quantum-well laser", *IEEE J. Quantum Electron.*, vol. 40, no. 10, pp. 1355–1364, 2004.

[6] J.M. Ostermann, F. Rinaldi, P. Debernardi, and R. Michalzik, "VCSELs with enhanced single-mode power and stabilized polarization for oxygen sensing", *IEEE Photon. Technol. Lett.*, vol. 17, no. 11, pp. 2256–2258, 2005.

Characterization of Strain-Compensated 980 nm Bottom-Emitting VCSELs

Ihab Kardosh, Michael Riedl, and Fernando Rinaldi

A new design of strain-compensated 980 nm bottom-emitting VCSELs is presented. Single devices and specially designed 3 × 3 VCSEL arrays have been successfully fabricated and characterized.

1. Introduction

Laser devices emitting in the 980 nm spectral region are interesting for many applications like pumping of solid-state lasers, pumping of optical amplifiers and frequency doubling for visible laser light generation. VCSELs with high output power and a good beam quality are attractive for such applications. In this work, strain compensation using phosphorus-containing layers close to the active region has been introduced for the first time, resulting in a considerable reduction of output power degradation and thus in an increase of the laser lifetime. Single laser devices have been fabricated and characterized on wafer, whereas laser arrays consisting of 9 devices have been mounted on heat sinks for simultaneous laser operation and for sufficient heat removal.

2. Device Fabrication

Figure 1 shows a schematic drawing of a typical bottom-emitting VCSEL. The sample consists of InGaAs quantum wells separated by GaAs barrier layers. GaAsP layers are introduced close to the active region for strain compensation. An AlAs layer in the p-side region is required for current confinement. After mesa etching, selective oxidation of the AlAs layer is performed to define the current aperture. Metallization layers are then evaporated to form a circular p-type contact on top of the mesa. Before mounting the devices on heat sinks, the substrate is usually thinned to reduce absorption and to ease cleaving. A Si_3N_4 anti-reflection (AR) coating is then deposited in the opening of the n-type contact on the substrate side.

2.1 VCSEL arrays

The fabricated VCSEL arrays consist of 3 × 3 devices each with an active diameter of 30 µm. Before mounting the devices upside down on heat sinks, a passivation layer of Si_3N_4 is deposited around the p-contacts to avoid any short circuits on mesa edges during the soldering process. Figure 2 shows two photographs of a laser array. The p-type

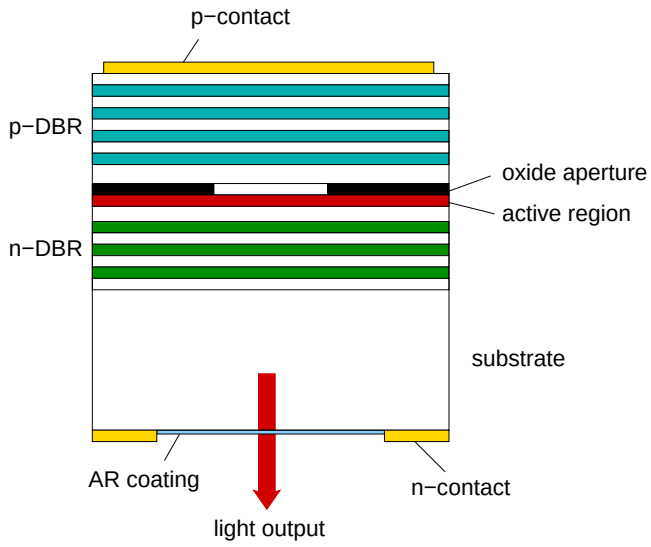

Fig. 1: Schematic cross-section of a bottom-emitting VCSEL.

metallization contacts and the silicon nitride passivation layer can be seen on the left. The substrate side with the n-type metallization is shown on the right. The chip area of about $1.25 \times 1.25\,\mathrm{mm}^2$ is indicated by the dashed lines. Individual chips containing VCSELs placed at 500 µm pitch are separated by cleaving.

The 3×3 VCSEL module is shown in Fig. 3. A cleaved chip is soldered epitaxial side down with indium to a copper heat sink. An underfill is used for mechanical stability. Gold wires are bonded from the electro-plated gold on the substrate side to the $(-)$ connector. The copper holder serves as the $(+)$ connector.

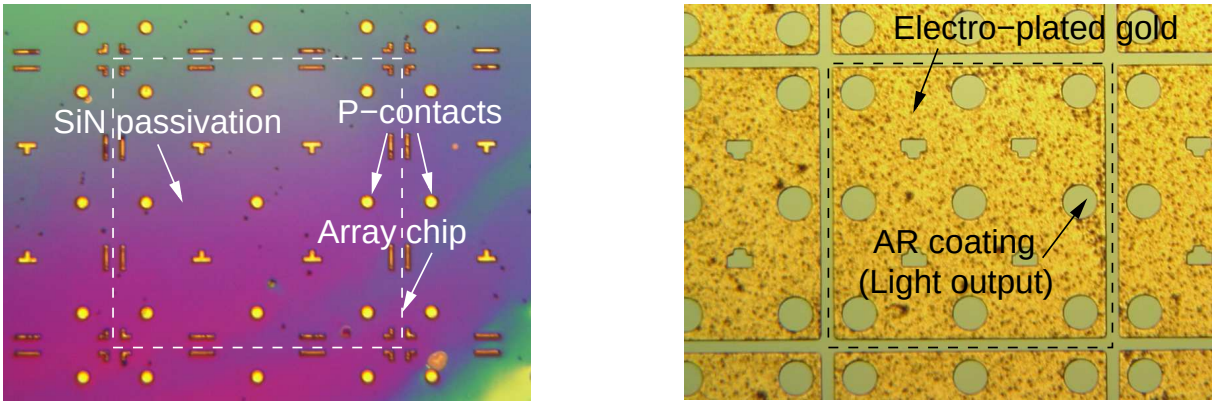

Fig. 2: Photographs of the epitaxial side (left) and the substrate side (right) taken after processing of the 3×3 VCSEL array.

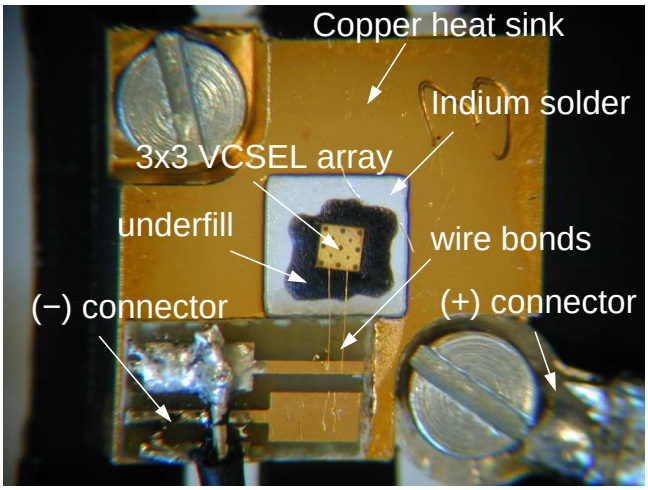

Fig. 3: Laser module containing the 3×3 VCSEL array. The array chip is soldered with indium to the gold-plated copper heat sink.

3. Characterization

VCSELs with different active diameters have been measured on wafer. In general, in addition to the lifetime improvement, the devices show a higher output power and differential quantum efficiency than standard bottom-emitting VCSELs without strain compensation [1]. In Fig. 4 the light–current–voltage (LIV) chracteristics of VCSELs with two different active diameter D_a can be seen. Extracted data like threshold current I_th, maximum output power P_max, differential quantum efficiency η_d, maximum wall-plug efficiency $\eta_\mathrm{wp,max}$, and emission wavelength λ are listed in Table 1.

Table 1: Key parameters of the devices from Fig. 4.

D_a [µm]	I_th [mA]	P_max [mW]	η_d [%]	$\eta_\mathrm{wp,max}$ [%]	λ [nm]
14	1.6	21.8	63	24.7	965
25	3.7	32.4	62	21.9	967

3.1 3×3 VCSEL array

The LIV characteristics of the VCSEL array module are displayed in Fig. 5. The devices have an individual oxide aperture of about 30 µm diameter. Key array data are 145 mA threshold current, 45 % differential quantum efficiency, and an output power of about 400 mW at 720 mA driving current. The IV curve shows 1.9 V threshold voltage and about 3 Ω average differential resistance. The module emits in a wide spectral range of about 10 nm at a driving current of 620 mA.

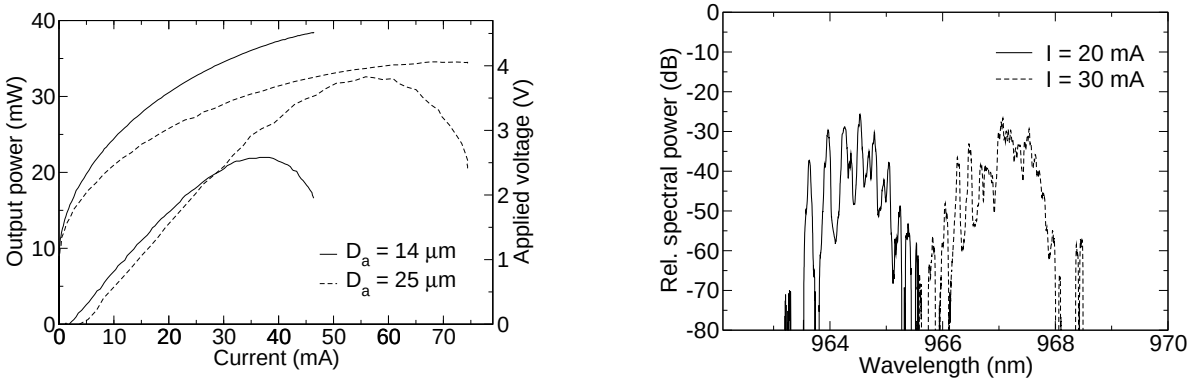

Fig. 4: LIV characteristics (left) and spectra (right) of bottom-emitting VCSELs with 14 µm and 25 µm active diameters.

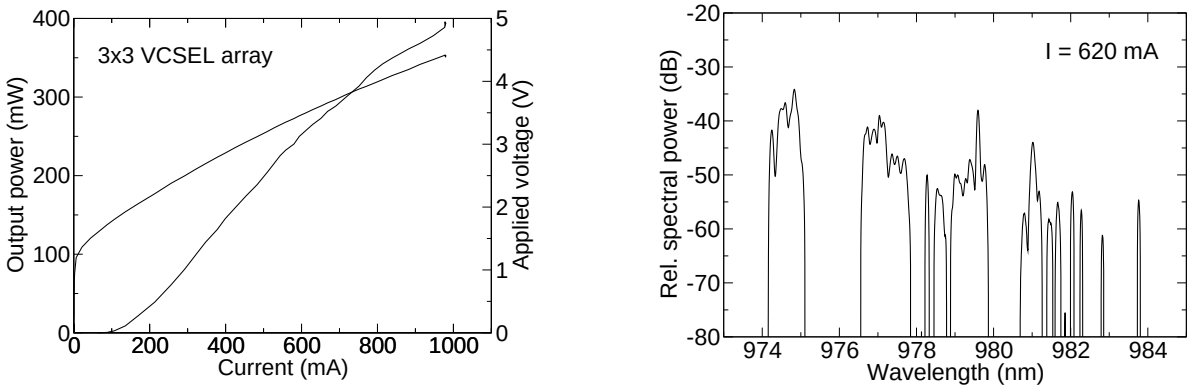

Fig. 5: Operating characteristics of the 3×3 VCSEL module from Fig. 3.

4. Conclusion

In this work, bottom-emitting VCSELs have been fabricated and characterized. A new layer design using GaAsP layers close to the active region has been implemented. In comparison with standard bottom-emitting VCSELs, the strain-compensated devices show higher output power and an increase in differential quantum efficiency. VCSEL arrays consisting of 3×3 elements have been also fabricated and characterized. The custom-designed arrays have a chip area of $1.25 \times 1.25\,\mathrm{mm}^2$ and a device pitch of 500 µm. An output power of about 400 mW is achieved from devices with 30 µm active diameter.

References

[1] I. Kardosh and F. Rinaldi, "Fabrication and characterization of 980 nm bottom-emitting VCSELs", *Annual Report 2005,* pp. 45–48. Ulm University, Institute of Optoelectronics.

Cavity Optimization of Electrically Pumped VECSELs

Wolfgang Schwarz

We have fabricated 960 nm wavelength vertical-external-cavity surface-emitting lasers (VECSELs) showing continuous-wave operation above room temperature. Absorption in the intra-cavity GaAs substrate has a strong impact on the efficiency and has to be considered for the design. Thus, apart from experimental results, in this work we deduce design rules from a numerical transfer matrix approach.

1. Introduction

Surface-emitting lasers with an external cavity delivering a diffraction-limited beam have shown the potential to outperform edge-emitting devices in applications demanding high brightness (emitted intensity per unit solid angle), like pumping of doped fiber amplifiers or frequency doubling [1]–[3]. Due to the large mode size, the VECSEL concept is power-scalable by expanding the pumped area and the heat-sink. This property makes VECSELs less susceptible to catastrophic optical mirror damage (COMD), spatial hole burning, and thermal lensing in comparison to edge-emitting devices. Similar to the sophisticated vertical-cavity surface-emitting laser (VCSEL), the optical resonator consists of a multiple quantum well gain material which is embedded between three distributed Bragg reflectors (DBRs).

2. Fabrication Steps

The semiconductor part of the device was grown by molecular beam epitaxy on GaAs (100)-oriented substrate and is similar to a conventional VCSEL. It consists of 30 p-doped DBR pairs and 7 n-DBR pairs ($Al_{0.11}Ga_{0.89}As/Al_{0.90}Ga_{0.10}As$) forming the internal resonant cavity. Silicon and carbon are used for n- and p-type doping, respectively. Graded heterojunction interfaces in both DBRs provide low electrical and optical losses. The active region is composed of three 8 nm thick $In_{0.15}Ga_{0.85}As$ quantum wells and 10 nm thick GaAs barriers. After growth, a 125 µm diameter circular ohmic contact was deposited on the top side and the n-doped ($\approx 7\,cm^{-1}$ loss) substrate was thinned to 120 µm. An ohmic n-ring contact on the bottom side enables electric current flow. The opening of the n-contact was anti-reflection coated with a single 120 nm thick layer of plasma-enhanced chemical vapor deposited (PECVD) Si_3N_4. The laser structure was p-side down soldered with In onto a copper heat-sink.

3. Optical Resonator Issues and Transfer Matrix Model

The beam quality factor $M^2 = \pi\Theta w_0/\lambda$ indicates how much the far-field divergence angle Θ differs from that of a perfect Gaussian beam, where λ is the wavelength and w_0 the beam radius. Neglecting thermal lensing within the device mesa and antiguiding effects from carrier injection, the optical resonator of a VECSEL can be modelled by the plane epitaxial DBR mirror and the external concave-shaped mirror. In this resonator, the modal beam radius $w_0^2 = M^2\lambda\sqrt{L\,(\varrho - L)}/\pi$ is determined by the resonator length L and the radius of curvature of the external mirror ϱ, since the curvature of the phase fronts must match the curvature of the external mirror [4, 5]. A simple transfer matrix model [6] was used to solve the Helmholtz equation $\partial^2 E(z)/\partial z^2 + \gamma^2 E(z) = 0$ for the electric field $E(z)$ and the propagation constant γ to describe the laser threshold gain g_{th} and the differential quantum efficiency $\eta_{\mathrm{d}} = (\Delta P/\Delta I)\cdot q\lambda/\,(hc)$ with the emitted optical power P, the electric current I, the elementary charge q, the vacuum velocity of light c, and Planck's constant h.

4. Experimental Setup and Results

The experimental setup is sketched in Fig. 1. A curved mirror ($\varrho = 20\,\mathrm{mm}$, 98 % reflectivity) was placed at an axial distance of about 20 mm to the laser aperture. The differential quantum efficiency η_{d} was extracted from the light–current–voltage (LIV) characteristics shown in Fig. 2. The efficiency of 1.5 % is considerably lower than in common VCSELs. A maximum output power of 2 mW was measured with a large-area photodetector. It is limited by thermal rollover and is reduced at elevated temperatures.

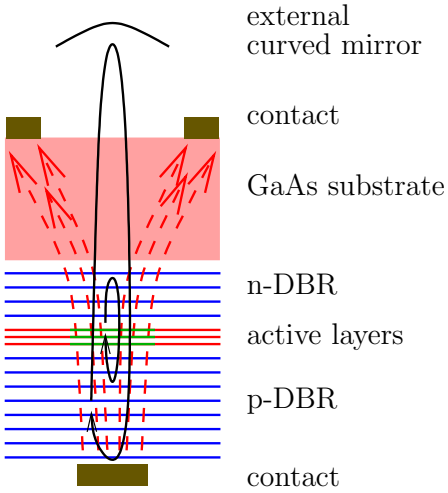

Fig. 1: Schematic VECSEL cross-section. The dashed and full lines indicate the current flow and the round-trip paths of the laser light, respectively.

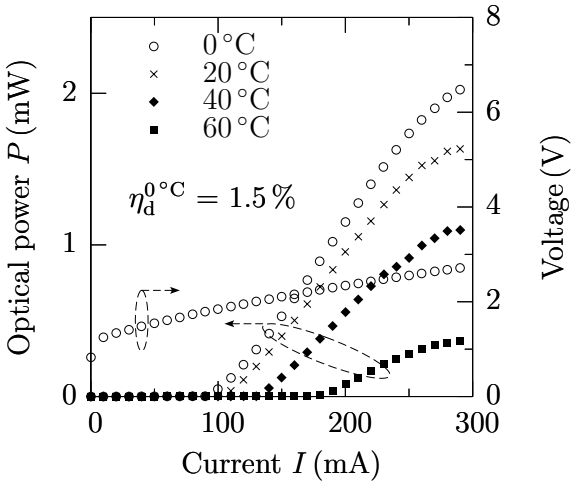

Fig. 2: Measured LIV characteristics of a VECSEL at different ambient temperatures. The p-contact diameter is 125 µm.

5. Discussion of the Results and Simulation

High losses in the external cavity seem to be the reason for the rather low device efficiency. For the simulation of the resonator losses, the transfer matrix method was employed. The absorption of the n-doped GaAs substrate was determined experimentally (Fig. 3). The measured substrate loss amounts to $\approx 7\,\mathrm{cm}^{-1}$ at 960 nm and is attributed to free-carrier absorption [7], corresponding to a doping density of $2.3 \cdot 10^{18}\,\mathrm{cm}^{-3}$. For the simulations, a n- and p-DBR absorption of $5.1\,\mathrm{cm}^{-1}$ and $7\,\mathrm{cm}^{-1}$, respectively, is assumed.

During every external cavity round-trip, a fraction of 15 % of the light is absorbed. In the resonator, this loss accumulates and the major part of the total generated light is absorbed. Consequently, the simulated efficiency drops down to 4 %. The simulated threshold gain and differential efficiency of an improved structure are depicted in Fig. 4 as a function of the number of epitaxial bottom mirror pairs for two different absorptions in the intracavity substrate. The re-design bears on a cavity incorporating a 90 % reflective external mirror and 7 n-doped mirror pairs, resulting in an efficiency of 20 % which is excelled by an efficiency of 60 % in case of an undoped substrate. This balance of internal and external cavity reflectivities provides a compromise beween both high efficiency and low threshold gain. The resulting threshold gain of $500\,\mathrm{cm}^{-1}$ for a device with 7 n-doped mirror pairs and 90 % external reflectivity is easily attainable in InGaAs/GaAs double heterostructures [8]. The dominant effect on the modal structure in the laser resonator is given by the finesse of both internal and external resonator. The inhomogeneous current injection profile resulting from large-area contacts usually does not support TEM_{00} operation. An external resonator with a sufficiently high finesse can be aligned such as to suppress higher-order transverse modes. For this reason, a higher ratio beween external and internal reflectivity might be favored when designing a device operating in the fundamental transverse mode.

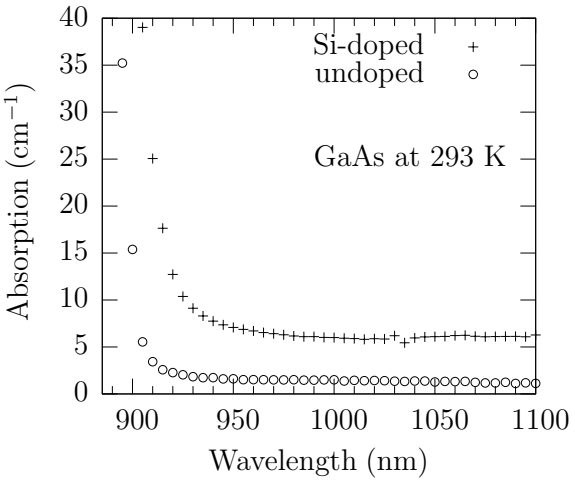

Fig. 3: Measured optical absorption in silicon-doped and undoped GaAs.

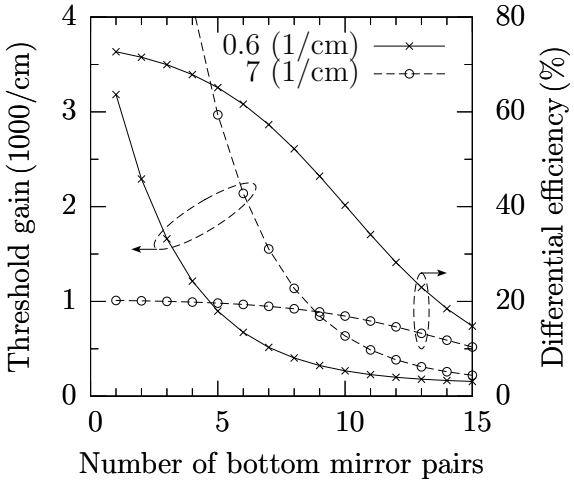

Fig. 4: Simulated threshold gain and differential efficiency in VECSELs incorporating doped and undoped GaAs substrates.

6. Conclusion

We have fabricated bottom-emitting electrially pumped InGaAs/GaAs VECSELs. In the present layout, the output performance is degraded by a high loss in the external cavity due to absorption in the doped GaAs substrate. As a result of transfer matrix calculations, this loss contribution limits the quantum efficiency to less than 4 %, in agreement with experimental results. It is suggested to minimize the impact of substrate absorption by choosing a 7-pairs epitaxial mirror and a 90 %-reflective external mirror. The absorption-induced loss scales with the substrate thickness, yet reducing the thickness below 100 µm makes device handling difficult. In order to get rid of parasitic absorption without the need for extreme wafer thinning, a moderatly doped substrate ($10^{17}\,\mathrm{cm}^{-3}$) is necessary. In this case an efficiency of more than 60 % is expected to be attainable.

References

[1] F. Kuznetsov, F. Hakimi, R. Sprague, and A. Mooradian, "High-power (> 0.5-W CW) diode-pumped vertical-external-cavity surface-emitting semiconductor lasers with circular TEM_{00} beams", *IEEE Photon. Technol. Lett.*, vol. 9, no. 8, pp. 1063–1065, 1997.

[2] E.M. Strzelecka, J.G. McInerney, A. Mooradian, A. Lewis, A.V. Shchegrov, D. Lee, J.P. Watson, K.W. Kennedy, G.P. Carey, H. Zhou, W. Ha, B.D. Cantos, W.R. Hitchens, D.L. Heald, V.V. Doan, and K.L. Lear, "High power, high brightness 980 nm lasers based on extended cavity surface emitting lasers concept", in *High-Power Fiber and Semiconductor Lasers*, M. Fallahi, J.V. Moloney (Eds.), Proc. SPIE 4993, pp. 57–67, 2003.

[3] J.-Y. Kim, S. Cho, S.-J. Lim, J. Yoo, G.B. Kim, K.-S. Kim, J. Lee, S.-M. Lee, T. Kim, and Y. Park, "Efficient blue lasers based on gain structure optimizing of vertical-external cavity surface-emitting laser with second harmonic generation", *J. Appl. Phys.,* vol. 101, no. 3, pp. 033103-1–4, 2007.

[4] A.E. Siegman, "Defining, measuring, and optimizing laser beam quality", in *Laser Resonators and Coherent Optics: Modeling, Technology, and Applications*, A. Bhowmik (Ed.), Proc. SPIE 1868, pp. 2–12, 1993.

[5] B.E.A. Saleh and M.C. Teich, *Fundamentals of Photonics*. New York, NY, USA: John Wiley & Sons, Inc., 1991.

[6] K.J. Ebeling and L.A. Coldren, "Analysis of multielement semiconductor lasers", *J. Appl. Phys.*, vol. 54, no. 6, pp. 2962–2969, 1983.

[7] W.G. Spitzer and J.M. Whelan, "Infrared absorption and electron effective mass in n-type gallium arsenide", *J. Appl. Phys.*, vol. 114, no. 1, pp. 59–63, 1959.

[8] L.A. Coldren and S.W. Corzine, *Diode Lasers and Photonic Integrated Circuits*. New York, NY, USA: John Wiley & Sons, Inc., 1995.

Integrated VCSEL Trap Arrays for Microfluidic Particle Separation and Sorting

Andrea Kroner

We introduce a novel concept of particle manipulation in microfluidics based on integrated linear arrays of optical traps. The integration into the microfluidic system is enabled by using vertical-cavity surface-emitting lasers as trap sources. Device layout and fabrication as well as simulations of the sorting process are presented.

1. Introduction

Microfluidic systems have evolved into an important tool in cell analysis, especially on the single-cell level, where conventional flow cytometry techniques are no longer convenient. Here, high throughput operation is not essential but small sample volumes and a possible integration of serial analysis steps. A basic analysis process is the sorting and separation of particles, where the use of optical forces has gained increasing interest owing to their independence on electrical charges and the compatibility to biological material [1]–[4]. To avoid the bulky and expensive optics commonly used to create optical traps, different approaches have been published which enable an integration into the microfluidic system [5, 6]. Here, the use of vertical-cavity surface-emitting lasers (VCSELs) offers not only small dimensions, high beam quality and low costs, but also a direct transfer of the sorting scheme presented in [1] and [2] into the microfluidic system. The concept is based on tilted arrays of optical traps, where the drag caused by the fluid medium is of the same size as the trapping force of each trap. Therefore, the traps will not fix a particle completely, but only deflect it from its initial flow direction as it passes by. So, while passing the traps, the particle follows the tilt of the array as it moves from the domain of one trap to the next. In this article we present a new approach based on one-dimensional VCSEL arrays directly integrated beneath microchannels to realize this sorting scheme in compact devices [7].

2. Device Layout and Simulation Results

Figure 1 shows the schematic of the integrated optical trap array which is based on top-emitting VCSELs with 850 nm emission wavelength. Photoresist microlenses are integrated on the output facets to focus the beam into the microfluidic channel which is placed on a 30 µm thin glass substrate [6]. The lenses are fabricated by a thermal reflow process and have radii of curvature of about 20 µm. Furthermore, a shallow surface relief is etched into the top mirrors to enhance transverse single-mode emission. In a similar

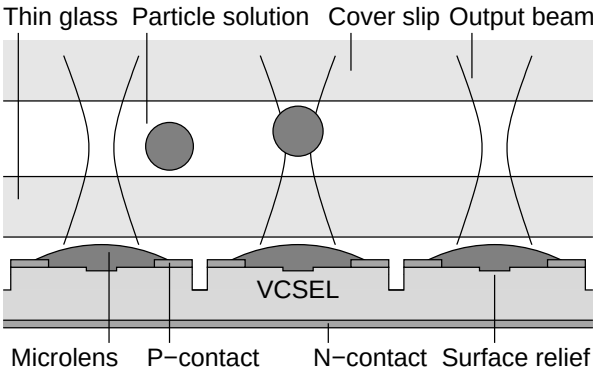

Fig. 1: Schematic of the integrated trap array.

setup with a single lensed relief VCSEL, we already demonstrated deflection, elevation and trapping of 10 µm diameter polystyrene particles with optical powers as low as 5 mW [6].

To determine the appropriate dimensions of the trap array like trap distance or tilt angle, we performed simulations of the separation process. The trapping potential created by a parallel beam with a transverse, Gaussian-shaped intensity profile was calculated based on a ray optics model [8]. The potential was then extended to a linear array, forming a two-dimensional potential profile. By solving the equation of motion including fluidic drag forces, the movement of a particle through the array can be determined. Figure 2 shows the result for a 15 µm diameter polystyrene particle passing a trap array tilted by 10°, where the water velocity is 90 µm/s. Each trapping beam has 5 mW of optical power, a diameter of 8 µm (based on experimental results on lensed relief VCSELs), and

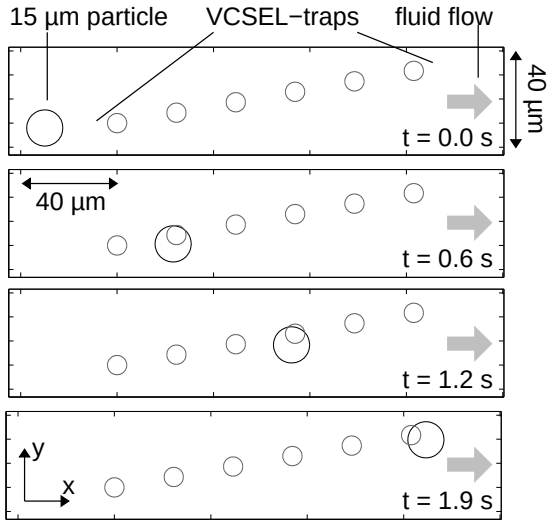

Fig. 2: Calculation of particle movement through a 10° tilted array of VCSEL traps for different points in time (top view on the microfluidic channel).

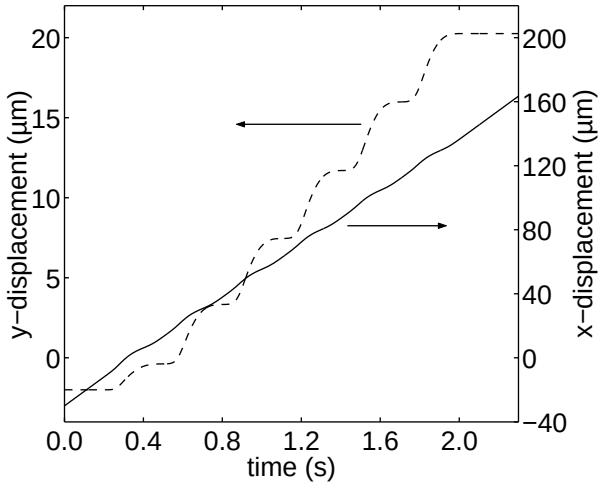

Fig. 3: Calculated x- and y-displacement in dependence on time for the particle movement shown in Fig. 2.

the trap distance is 25 µm. Caused by the six-trap array, the particle is deflected by more than 20 µm in y-direction, while the movement in x-direction is only slightly disturbed, what can be seen in Fig. 3, showing the the x- and y-displacement in dependence on time. Thus, a separation of specific particles can be performed by switching the array on or off. Since the interaction between trap and particle is dependent on particle properties like size or refractive index, also sorting can be achieved, e.g. 10 µm particles are not deflected for the above given conditions.

3. Conclusion

Integrated VCSEL trap arrays promise separation and sorting on the single-cell level in compact devices which are still compatible to other analysis steps like Raman spectroscopy, fluorescence analysis or electrophoresis. First experiments on particle manipulation confirmed the concept of the integrated trap and simulations were performed to analyze the separation process in trap arrays. The achieved results were used for specialty array design. VCSEL array fabrication is currently in progress.

References

[1] M.P. MacDonald, G.C. Spalding, and K. Dholakia, "Microfluidic sorting in an optical lattice", *Nature*, vol. 426, pp. 421–424, 2003.

[2] K. Ladavac, K. Kasza, and D.G. Grier, "Sorting mesoscopic objects with periodic potential landscapes: optical fractionation", *Phys. Rev. E*, vol. 70, no. 1, pp. 010901-1–4, 2004.

[3] R.W. Applegate Jr., J. Squier, T. Vestad, J. Oakey, D.W.M. Marr, P. Bado, M.A. Dugan, and A.A. Said, "Microfluidic sorting system based on optical waveguide integration and diode laser bar trapping", *Lab Chip*, vol. 6, no. 3, pp. 422–426, 2006.

[4] M.M. Wang, E. Tu, D.E. Raymond, J.M. Yang, H. Zhang, N. Hagen, B. Dees, E.M. Mercer, A.H. Forster, I. Kariv, P.J. Marchand, and W.F. Butler, "Microfluidic sorting of mammalian cells by optical force switching", *Nat. Biotech.*, vol. 23, no. 1, pp. 83–87, 2005.

[5] S. McGreehin, K. Dholakia, and F. Krauss, "Monolithic integration of microfluidic channels and semiconductor lasers", *Optics Express*, vol. 14, no. 17, pp. 7723–7729, 2006.

[6] A. Kroner, J.F. May, I. Kardosh, F. Rinaldi, H. Roscher, and R. Michalzik, "Novel concepts of vertical-cavity laser-based optical traps for biomedical applications", in *Biophotonics and New Therapy Frontiers*, R. Grzymala, O. Haeberlé (Eds.), Proc. SPIE 6191, pp. 619112-1–12, 2006.

[7] A. Kroner, A. Gadallah, I. Kardosh, F. Rinaldi, and R. Michalzik,"Integrated VCSEL trap arrays for microfluidic particle separation and sorting", in Proc. *EOS Topical Meeting on Biophotonics and Biomedical Optics*, pp. 140–141. Paris, France, Oct. 2006.

[8] A. Ashkin, "Forces of a single-beam gradient laser trap on a dielectric sphere in the ray optics regime", *Biophys. J.*, vol. 61, no. 2, pp. 569–582, 1992.

Oblong-Shaped VCSELs with Pre-Defined Mode Patterns

A. Gadallah and A. Kroner

We report fabrication and characterization of a novel type of vertical-cavity surface-emitting laser (VCSEL). A dotted surface etch in an oblong-shaped output aperture is utilized to select a certain higher-order transverse mode. Optical trapping and particle manipulation are attractive applications for these VCSELs.

1. Introduction

VCSELs, which emit from the planar surface of the wafer rather than from the cleaved end facets, have been extensively investigated over the last years. The main advantages of these devices over the conventional edge-emitting lasers lie in their spatial and spectral output properties as well as manufacturing, testing, and packaging at lower cost. Because of their suitability for monolithic integration into two-dimensional arrays, VCSELs pave the way for a large variety of applications, such as space-parallel optical communication technologies or optical sensing and lighting using high-power sources. A new and attractive application of VCSELs in biophotonics is optical trapping, where active manipulation of biological cells [1], stacking and translation of microscopic particles [2], as well as a miniaturized system, the so-called integrated optical trap [3], were already successfully demonstrated. In order to sort particles using such an integrated optical trap, we intend to selectively deflect them from their initial flow direction with the trapping forces of a tilted, continuously emitting VCSEL array as described in [4] and the preceding article in this Annual Report. In order to create the required closely spaced intensity maxima, here we introduce a novel VCSEL which oscillates on a pre-defined high-order mode.

2. Fabrication and Simulation

A photograph of the new oblong-shaped VCSEL is shown in Fig. 1. The dotted surface etch is utilized to stimulate a certain transverse mode. There are two main differences between this specially designed VCSEL and a standard device. Firstly, concerning the layer structure, a quarter-wavelength anti-phase layer is added in order to induce a decrease in top mirror reflectivity. This layer is then selectively removed by means of wet-chemical etching. The second point concerns the shape of the mesa and thus of the oxide aperture. It is no longer of circular shape, instead it is rectangular, where one side of the rectangle is much longer than the other. The layer structure consists of 23 C-doped

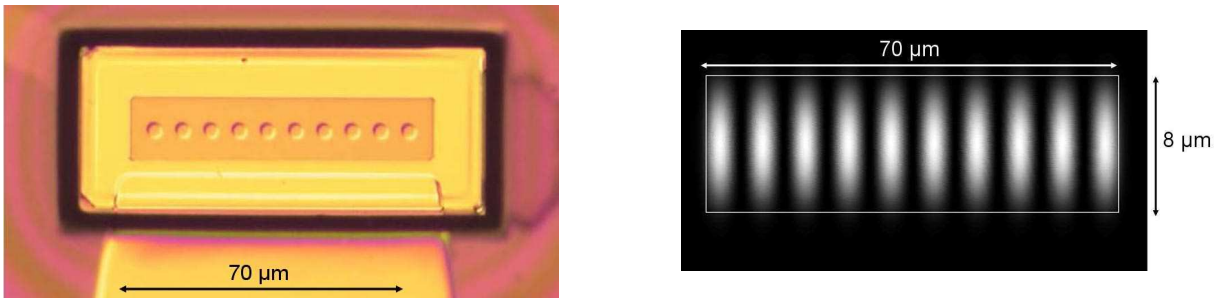

Fig. 1: Photograph of an oblong-shaped VCSEL with a $70 \times 8\,\mu m^2$ size oxide aperture and a 10-spot surface relief pattern (left). Simulated intensity profile of the selected high-order mode (right).

GaAs/AlGaAs p-distributed Bragg reflector (DBR) pairs as top mirror (plus the topmost GaAs quarter-wave layer), 38.5 Si-doped n-DBR pairs as the bottom mirror, and three 8 nm thick GaAs quantum wells for laser emission around 850 nm wavelength. Current confinement is achieved through thermal oxidation of an AlAs layer placed just above the one-wavelength thick inner cavity. Wet etching is used to reach this layer. N- and p- type metallization processes are applied, followed by polyimide passivation. Finally, bond-pad metallization is carried out for electrical contacting. Concerning the simulation of the transverse modes supported by the VCSEL cavity, the following approach is taken: We assume a rectangular semiconductor core of refractive index n_1, which corresponds to the non-oxidized cross-sectional area of the cavity, surrounded by a cladding layer of refractive index $n_2 < n_1$. The indices n_1 and n_2 are interpreted as average numbers in the longitudinal cavity direction. The index difference $\Delta n = n_1 - n_2$ is related to the cavity resonance shift $\Delta\lambda_{ox}$ as [5]

$$\Delta n = n_1 \Delta\lambda_{ox}/\lambda \ , \tag{1}$$

where λ is the lasing wavelength. The parameter $\Delta\lambda_{ox}$ is easily determined from two calculations with the transfer matrix method [5] as the difference in resonance wavelengths in the non-oxidized and oxidized parts of the cavity. With known indices n_1 and n_2, we then solve the Helmholtz equation in the transverse plane while applying the Dirichlet boundary conditions, i.e., the electric field diminishes at the boundary of the calculation window. The result is a usually large number of guided transverse modes. The simulated intensity profile for one such mode for oxide aperture dimensions of 8 µm width and 70 µm length is illustrated in Fig. 1 (right), where the calculation window is $18\,\mu m \times 80\,\mu m$. Its two dimensional mode order can be denoted as $(1, 10)$. In order to select this mode as the main lasing mode of the VCSEL, the anti-phase layer is selectively removed at positions coinciding with the calculated intensity maxima. The resulting surface relief is well visible in Fig. 1 (left).

3. Experimental Results

The light–current–voltage (LIV) characteristics of several oblong-shaped VCSELs without surface modification are displayed Fig. 2 (left), where dimensions (width × length) of the devices, e.g. $4\,\mu m \times 30\,\mu m$, are indicated. With increasing width, both the laser

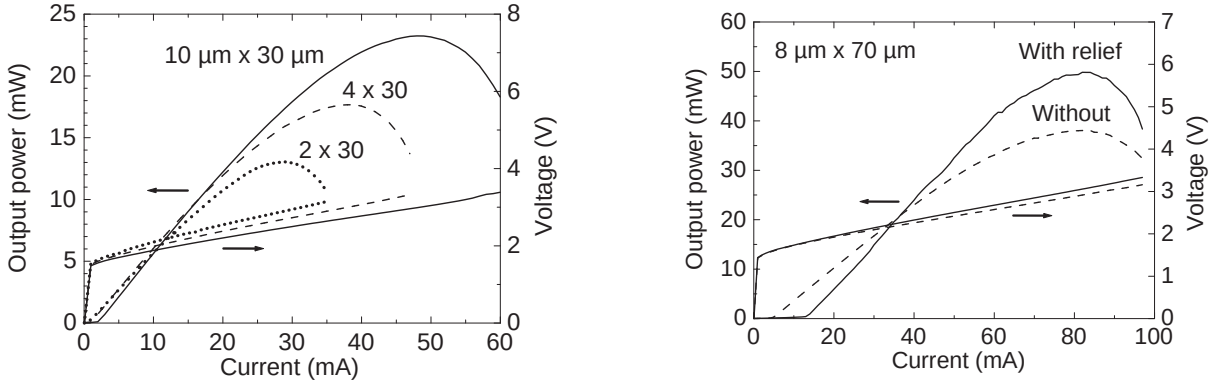

Fig. 2: LIV characteristics of standard oblong-shaped VCSELs of different size (left) and of a relief device in comparison with its reference (right).

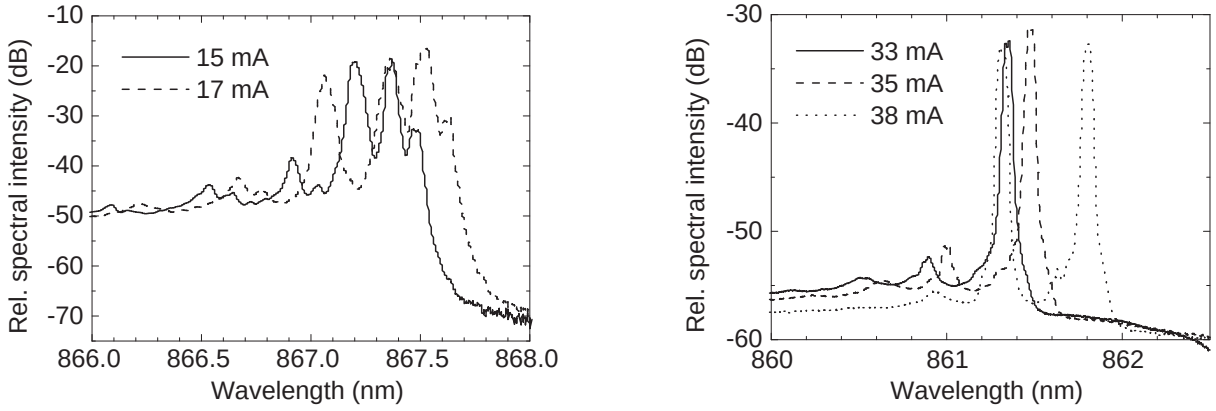

Fig. 3: Laser emission spectra of the standard $(8 \times 70)\,\mu m^2$ VCSEL (left) and of the corresponding relief device (right) according to Fig. 2 (right), both at different laser currents.

threshold current and the output power increase. For instance the laser threshold current and maximum output power are 0.9 mA and 17.5 mW, respectively, at 4 µm width. These values increase to 2 mA and 23.3 mW when the width of the device is 10 µm. On the other hand, it is worth to mention that the threshold current density increases with decreasing width, which is attributed to an increase of diffraction and scattering losses.

A comparison between the LIV characteristics of a reference oblong-shaped VCSEL and a relief device is made in Fig. 2 (right). Both the threshold current and the maximum output power of the relief device are increased, the latter to as much as 50 mW. This is caused by the reduction of the effective top mirror reflectivity. The laser spectra emitted from a standard $(8 \times 70)\,\mu m^2$ VCSEL are shown in Fig. 3 (left) for two different currents. Multiple transverse modes oscillate simultaneously even near threshold. On the other hand, there is a tendency for suppression of these higher-order modes in case of the relief devices, as shown in Fig. 3 (right). In order to identify the main mode in the spectrum in Fig. 3 (right), we have performed a spectrally resolved near-field measurement by scanning a lensed fiber tip over the output aperture with high resolution. Figure 4 shows the near-field intensity pattern of the VCSEL from Fig. 1 (left), having 10 etch spots, each 4 µm wide. The data are recorded at 31 mA current (see Fig. 2, right). The measured and

simulated (Fig. 1, right) spectra are similar, however, the former exhibits 9 instead of 10 maxima as well as some irregularities. Currently we attribute these effects to the gradient in layer thickness incorporated during molecular beam epitaxial growth, which induces a cavity resonance shift along the device length.

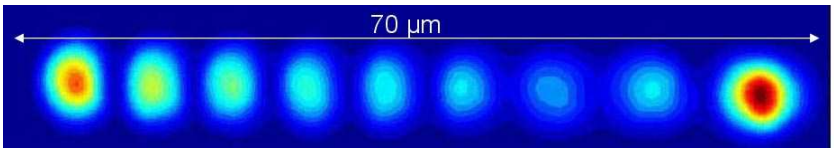

Fig. 4: Near-field intensity pattern of the oblong-shaped VCSEL from Fig. 1 (left), recorded at 31 mA current (see Fig. 2, right). The wavelength is 865 nm.

4. Conclusions

Design, fabrication, and characterization of oblong-shaped VCSELs with large length-to-width ratio of the oxide aperture have been carried out. For very narrow widths, scattering and diffraction losses increase the threshold current density. A dotted surface etch is employed to select a defined mode with order $(1, N)$, where N is a large integer. The surface relief reduces the mirror reflectivity and increases both the threshold current as well as the peak output power. First mode-controlled devices have been realized, however, the selection mechanism needs further improvement.

References

[1] A.L. Birkbeck, R.A. Flynn, M. Ozkan, D. Song, M. Gross, and S.C. Esener, "VCSEL arrays as micromanipulators in chip-based biosystems", in *Biomedical Microdevices*, vol. 5, no. 1, pp. 47–54, 2003.

[2] F. Sumiyama, Y. Ogura, and J. Tanida, "Stacking and translation of microscopic particles by means of 2 × 2 beams emitted from a vertical-cavity surface-emitting laser array", *Appl. Phys. Lett.*, vol. 82, no. 18, pp. 2969–2971, 2003.

[3] A. Kroner, I. Kardosh, F. Rinaldi, and R. Michalzik, "Towards VCSEL-based integrated optical traps for biomedical applications", *Electron. Lett.*, vol. 42, no. 2, pp. 93–94, 2006.

[4] A. Kroner, A. Gadallah, I. Kardosh, F. Rinaldi, and R. Michalzik, "Integrated VCSEL trap arrays for microfluidic particle separation and sorting", in Proc. *EOS Topical Meeting on Biophotonics and Biomedical Optics*, pp. 140–141. Paris, France, Oct. 2006.

[5] R. Michalzik and K.J. Ebeling, "Operating Principles of VCSELs", Chap. 3 in *Vertical-Cavity Surface-Emitting Laser Devices*, H. Li and K. Iga (Eds.), pp. 53–98. Berlin: Springer-Verlag, 2003.

A Simple Half-Duplex Optical Link Using Two Identical Fabry–Pérot Lasers at 1.55 µm Wavelength

Philipp Gerlach

We report on a simple bidirectional optical link using two InP-based Fabry–Pérot (FP) lasers operating at 1.55 µm wavelength as optical transmitter and receiver. Since the emitted light of one FP laser is absorbed by the other when it is reverse biased, no additional photodiode is required. The optoelectronic devices are butt-coupled to single-mode fibers (SMFs). With this configuration, up to 100 Mbit/s operation over a 50 km-long standard SMF is demonstrated. The optical link length is limited by fiber attenuation and coupling losses. In addition, we suggest a simple electrical driver circuit which acts as an interface between a RS 232 computer port and the FP laser. It enables half-duplex operation. A combined transimpedance receiver circuit improves the sensitivity of the optical system and allows successful bidirectional communication of two personal computers (PCs) over 100 km of SMF.

1. Introduction

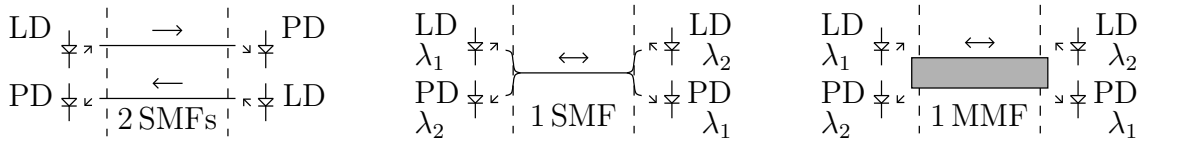

(a) Two unidirectional SMFs

(b) One bidirectional SMF with fiber couplers

(c) One MMF with narrow spaced LD and PD

Fig. 1: Schematics of some basic approaches of bidirectional optical links.

Bidirectional optical links have been established in different configurations. The most straightforward configuration consists of two independent SMFs which operate in unidirectional mode (see Fig. 1(a)). With optical circulators or wavelength-division muliplexing, the use of only one SMF becomes possible, however, expensive components are required, e.g. wavelength filters and a laser and a photodiode on both sides (Fig. 1(b)). The optical system configuration is much relaxed if multimode fibers (MMFs) are used, because laser and photodiode can be placed close to each other and be directly butt-coupled to the MMF (Fig. 1(c)) [1]. However, the bandwidth–length product of this approach is limited by modal dispersion.

In this article we use only one optoelectronic component at each side of the optical link, as indicated in Fig. 2. We operate at $\lambda = 1.55\,\mu\text{m}$ wavelength in order to benefit from

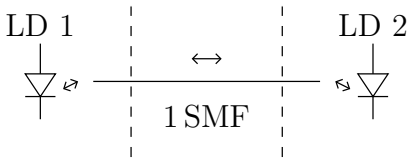

Fig. 2: Schematic of our bidirectional approach incorporating two identical FP lasers.

the attenuation minimum of the SMF. FP lasers are the first choice because they do not have wavelength-selective mirrors, what enables the use as a detector as well. FP lasers emit on several longitudinal modes and have a rather broad spectrum, which limits the modulation speed to several Mbit/s over a 50 km-long SMF.

2. Design and Fabrication

We use an InP-based ridge-waveguide structure to ensure lateral single-mode behavior. The active layer consists of six 6 nm-thick compressively strained InGaAlAs quantum wells. The simulated modal gain is shown in Fig. 3, where the simulation model of [2] has been used. The given laser waveguide provides a transverse optical confinement factor of about 7 %. Due to the strong excitonic absorption at around $\lambda = 1550$ nm, we observe high absorption for reverse-biased waveguides. Figure 4 shows the simulated modal absorption for the same waveguide as in Fig. 3 for several applied reverse voltages.

The 2 µm-wide ridge-waveguide is realized by wet-etching while using the metal p-contact as etch mask. Benzocyclobutene (BCB) has been employed for passivation. P-type bond-pads are created with a lift-off process. After the samples are thinned to a thickness of

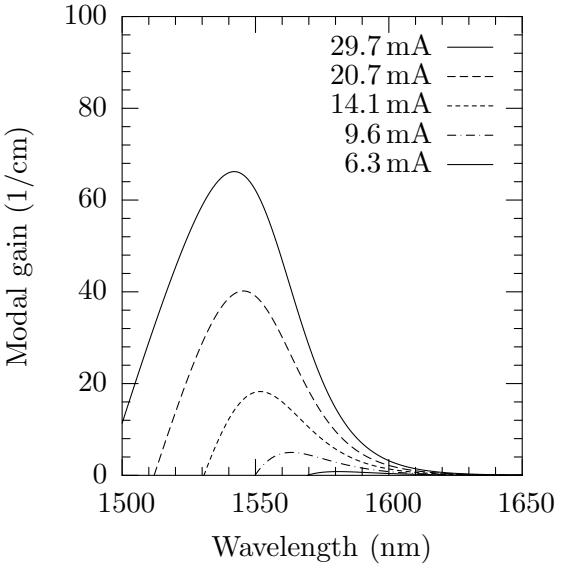

Fig. 3: Simulated modal gain of the ridge-waveguide structure for several pumping currents.

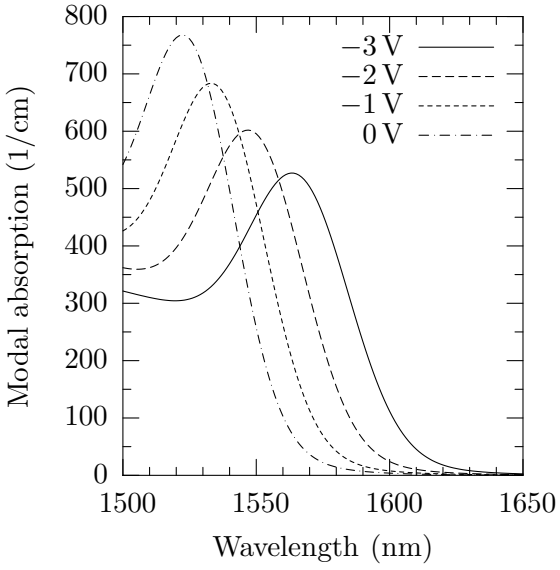

Fig. 4: Simulated modal absorption of the ridge-waveguide from Fig. 3 for several reverse bias voltages.

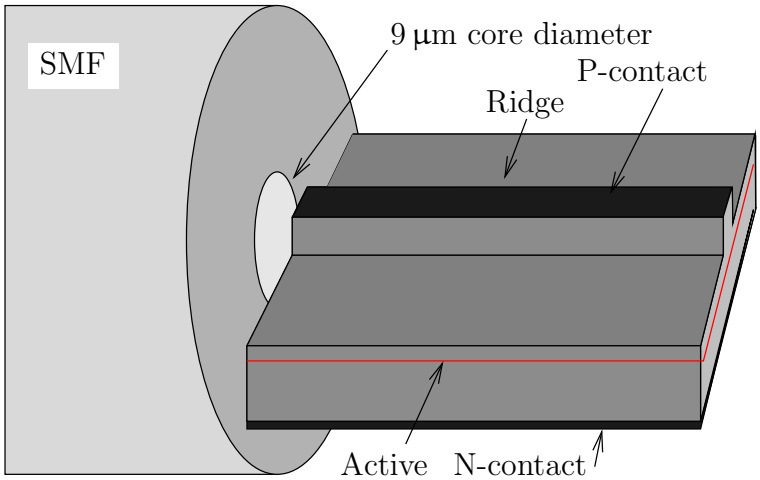

Fig. 5: Schematic of a FP ridge-waveguide laser diode coupled to a SMF.

about 100 µm, the n-contact is evaporated. The devices are cleaved to lengths of 500 µm and resulting short laser bars are glued to SMA-type connectors and wire-bonded.

The devices are directly placed in front of the core of a SMF, as indicated in Fig. 5. Figure 6 shows photographs of mounted lasers prepaired for bidirectional operation. Although relatively high coupling losses are to be expected with this configuration, no additional optics are used in order to keep the setup as simple as possible.

Figure 7 displays the simulated mode field within the ridge-waveguide structure of the laser diode, which is found by a numerical solution of the scalar wave equation. Figure 8 illustrates the simulated field of the fundamental mode of a SMF which is calculated in the same way. Please note the difference in the scaling of the axes. The mode mismatch is chiefly responsible for the low coupling efficiency.

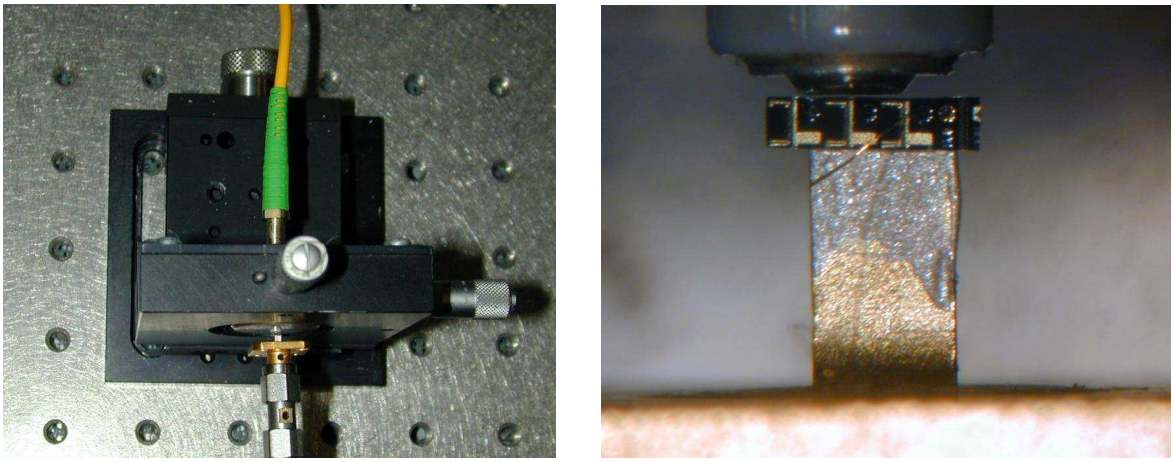

Fig. 6: Photographs of a laser-to-fiber coupling unit. A FP laser bar is glued with its epitaxial side to the inner electrode of a SMA connector. The p-contact is wire-bonded. Laser aligned in front of a SMF (left) and close-up (right).

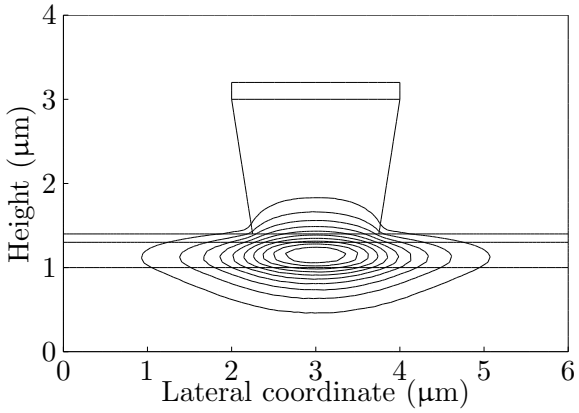

Fig. 7: Simulated transverse mode pattern in the ridge-waveguide laser structure.

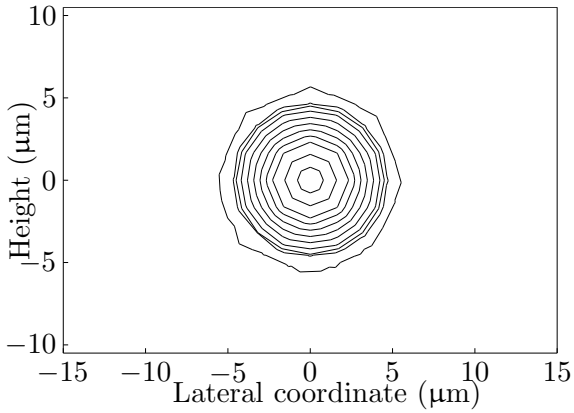

Fig. 8: Simulated fundamental mode of a SMF with 9 µm core diameter.

2.1 Laser characteristics

Figure 9 shows the static light–current–voltage characteristics of the fabricated lasers. The threshold current is 25 mA. An optical output power of more than 8 mW at a laser current of 70 mA is measured at the front facet. The fiber-coupled power is much smaller, corresponding to a coupling coefficient of 10 %. The measured optical spectrum at a laser current of 60 mA features a large number of longitudinal modes, centered at about 1526 nm wavelength.

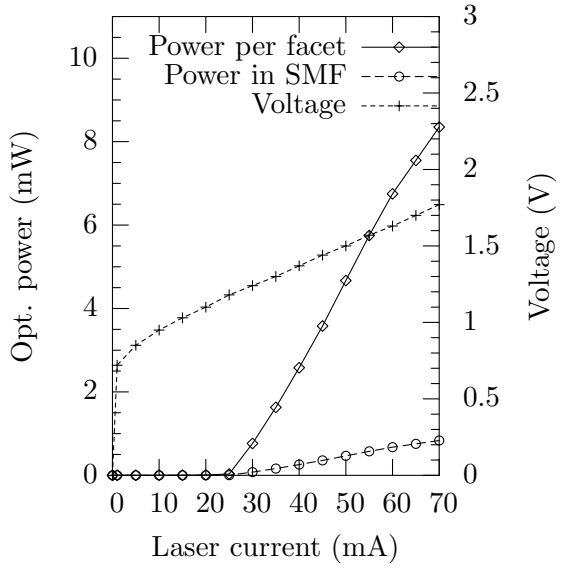

Fig. 9: Operation characteristics of the FP laser, including the light versus current curve for single-mode fiber coupling.

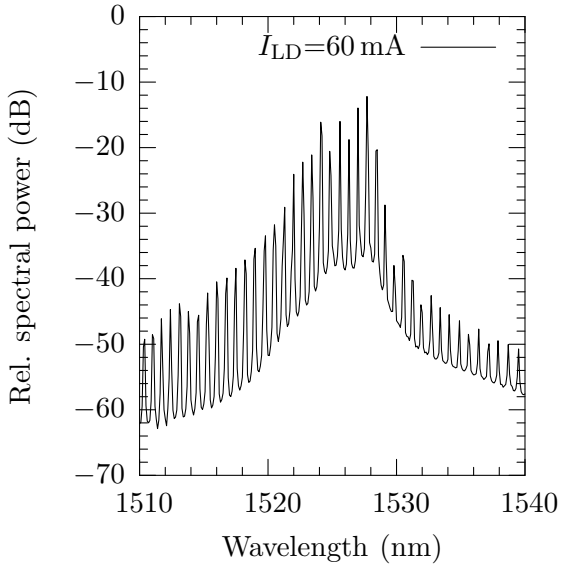

Fig. 10: Measured optical spectrum of the laser in Fig. 9 at 60 mA current.

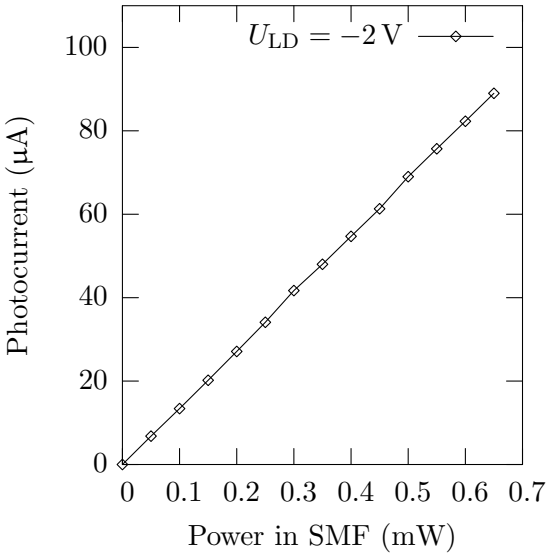

Fig. 11: Measured photocurrent as a function of the power in the single-mode fiber for a reverse voltage of 2 V.

3. Half-Duplex Operation

Figure 11 shows the static characteristic of a fabricated FP laser acting as a photodiode, where the photocurrent has been measured as a function of the incident optical power at an applied reverse voltage of 2 V. A coupling efficiency of 18 % is calculated for the detection process, which is much higher than in the case of forward operation. This might be explained by an increased detection (as compared to emission) area, since photons incident with moderate lateral offset might also contribute to the photocurrent.

Figures 12 and 13 demonstrate the proper modulation capability of the established optical link. One FP laser is directly modulated with a digital pseudorandom bit sequence of

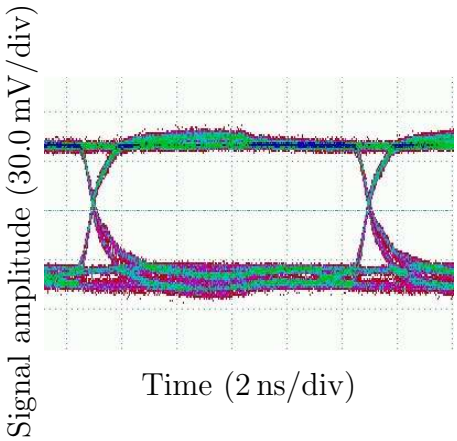

Fig. 12: Measured eye diagram at a data rate of 100 Mbit/s, back-to-back.

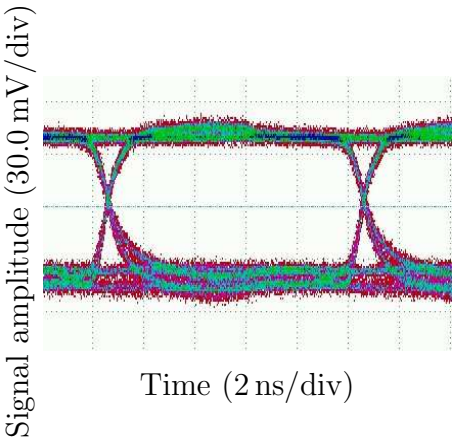

Fig. 13: 100 Mbit/s, eye diagram after transmission over a SMF with 4 km length.

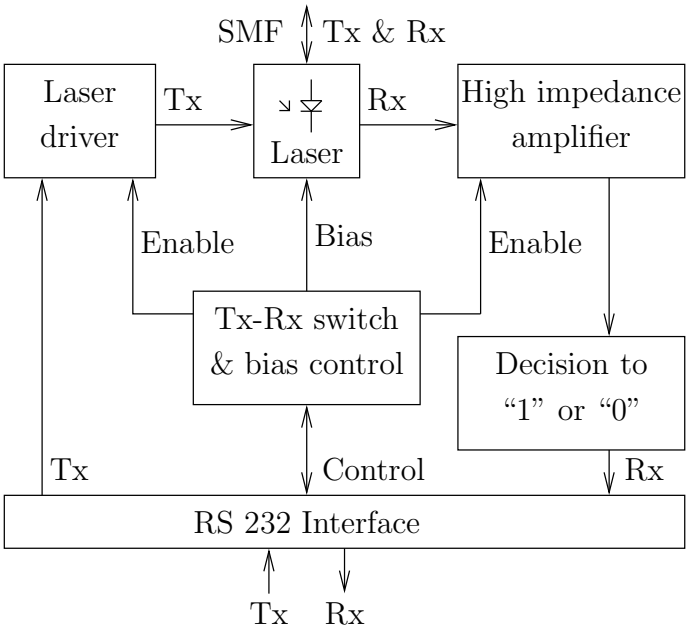

Fig. 14: Block diagram of the bidirectional RS 232 interface.

$2^7 - 1$ word length, where the bias current is 60 mA and the modulation voltage is $2\,V_{pp}$. A second FP laser is reverse biased with 2 V and connected to an amplifier with 50 Ω input impedance and 1.3 GHz bandwidth. The signal is displayed by a sampling oscilloscope. Both eye diagrams are recorded for the same photocurrent of 50 µA. The dispersion of the 4 km-long SMF does not alter the shape of the eye. The rise and fall times are limited by the detection process to a few nanoseconds. The eye diagrams are very similar if the link operates in the opposite direction.

For longer SMFs, the fiber attenuation increases and optical detection with higher sensitivity is required. Since we are operating at 1.55 µm wavelength, the modulation speed would be then limited by group velocity dispersion[2]. For increasing the detection sensitivity, the measurement bandwidth can be decreased and high-impedance amplification can be used.

4. RS 232 Interface with Transimpedance Receiver

A block diagram and a full circuit diagram of the computer interface are shown in Figs. 14 and 15, respectively. The signal-to-noise ratio and therefore the receiver sensitivity can be optimized by choosing a low-noise amplifier with high-impedance input [3]. On the other hand, the electrical time constant given by the product of the impedance R and the input capacitance C sets an upper limit for R. Since the suggested link is supposed to work at very low data rates of several kbit/s, we decided to use a BC 547 npn-type bipolar transistor in emitter configuration with high-impedance input for this purpose. When the laser is reverse biased, the photo-generated current will directly flow through its base.

[2]Dispersion compensation would not be implemented in such a low-cost optical link.

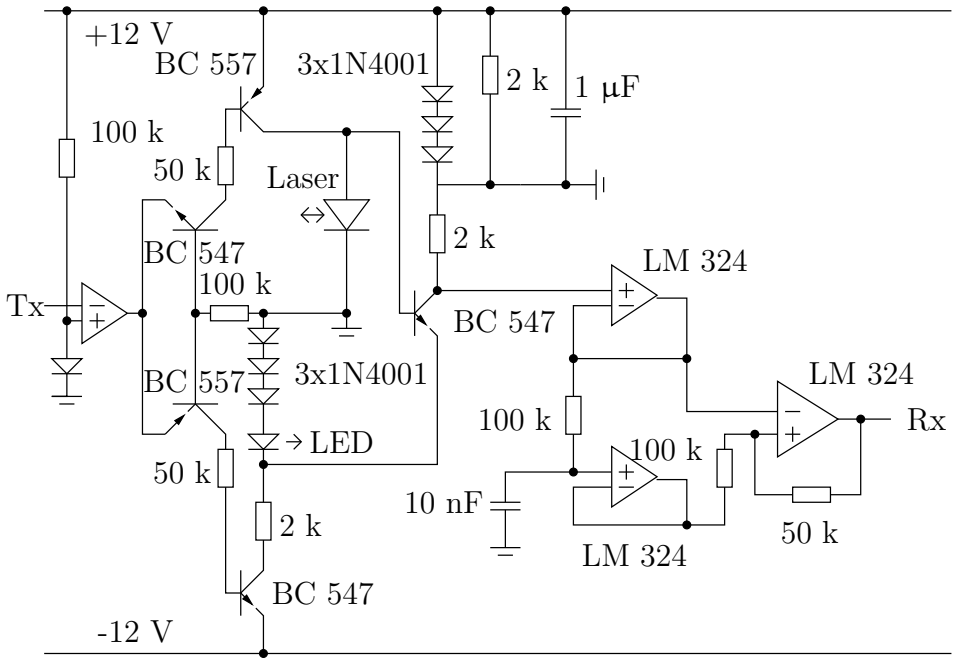

Fig. 15: Electrical circuit diagram of FP laser with driver electronics for bidirectional operation.

The collector current is much higher according to the current amplification factor and will induce a voltage drop at the 2 kΩ-large resistor. Proper digital signals are recovered using three operational amplifiers. They make a digital decision as well, using the low-pass filtered analog signal as reference. In addition, the circuit contains some electronics on the left-hand side. It drives the laser diode for bias-free transmit (Tx) operation and switches back to the reverse-biased receive (Rx) state. With two of the given circuits, a fully operational link has been established between two PCs over a 100 km-long SMF, where the data rate is 2400 bit/s.

5. Conclusion and Outlook

A simple half-duplex bidirectional optical link with FP lasers which act as both transmitter and photodetector is successfully demonstrated. The bandwidth of this link is limited to a maximum data rate of 500 Mbit/s, which might be explained by carriers which are generated lateral to the ridge-waveguide and are expected to have quite high transport time constants. This bandwidth might be improved by using lensed fibers which focus the light more directly into the waveguide. At the same time, the laser coupling efficiency would thus be increased. Unfortunately, the mechanical stability of this configuration is rather critical and not suited for long-term experiments at the moment. It is expected that the bandwidth can be increased to several GHz. A simple electronic interface is suggested which enables bidirectional communication of two PCs. It features transimpedance amplification and automatic decision levelling. Its operation speed is limited to a few kbit/s but is expected to be drastically higher with an improved electronics design.

References

[1] M. Stach, F. Rinaldi, M. Chandran, S. Lorch, and R. Michalzik, "Bidirectional optical interconnection at Gb/s data rates with monolithically integrated VCSEL-MSM transceiver chips", *IEEE Photon. Technol. Lett.*, vol. 18, no. 22, pp. 2386–2388, 2006.

[2] M. Peschke, T. Knoedl, and B. Stegmueller, "Simulation and design of an active MQW layer with high static gain and absorption modulation", in Proc. *Numerical Simulation of Semiconductor Devices, NUSOD 2003*, pp. 15–16. Tokyo, Japan, October 2003.

[3] K.J. Ebeling, *Integrated Optoelectronics*. Berlin: Springer-Verlag, 1993.

Self-Separation of GaN Using In-Situ Deposited SiN as Separation Layer

Peter Brückner

Thick, self-separated GaN layers have been grown by hydride vapor phase epitaxy (HVPE) on templates with SiN-interlayers, which worked as the separation layer. The used templates were prepared by metalorganic vapor phase epitaxy (MOVPE) to start with an excellent seed layer. As several groups reported, it was observed, that by using only one SiN-interlayer, the dislocation density could be reduced by an order of magnitude. To use the SiN-interlayer as separation layer, a much weaker connection between the template and the thick HVPE grown GaN should be generated. To study the separation process in-depth, we started our studies with a stack of multiple SiN-interlayers. Those structures lead to large masked areas or even, by the right choice of the deposition parameters, to a cavernous layer. On those templates, the separation during the cool down of nearly full 2 inch wafers could be observed. These thick self-separated HVPE layers showed a smooth surface morphology with excellent optical and electrical properties.

1. Introduction

The improvement of GaN based electronic and optoelectronic devices is still limited by the fact that epitaxial structures, like lasers and LEDs, have to be grown on foreign substrates like sapphire or SiC, because high quality GaN-wafers are not yet really available for an adequate price. The growth on such foreign substrates causes a high defect density, which limits the device performance. It has been estimated that the dislocation density should be below $10^6\,\mathrm{cm}^{-2}$ in order to get high lifetime and a good radiative efficiency for LASER structures. Many groups investigated techniques like, e.g., laterally epitaxially overgrown GaN stripes to reduce the defect density [1]. Although, those groups could control the propagation and the arrangement of the threading dislocation, they could not reduce the dislocation density homogenously over the whole wafer. To get homogenous, low dislocation densities, it is essential to do homepitaxial growth of GaN. To generate such substrates for the homoepitaxial growth, the growth of thick layers by hydride vapor phase epitaxy was developed by several groups. Excellent optical devices could be fabricated on such HVPE grown quasi-substrates, but these non-freestanding substrates still suffer from several problems. The used foreign substrate for thick GaN make backside contact difficult or even, in case of sapphire, impossible. Moreover, the strain induced by the foreign substrate results in strong bending of these non-freestanding quasi-substrates.

To overcome these problems, freestanding GaN-wafers have been prepared by removing the foreign substrate after the HVPE process. In most cases, this requires some complex, time consuming processes like laser lift-off [2] or special substrates like GaAs, which

can be removed by wet chemical etching [3]. Another possibility is the self-separation of the GaN-layer from the substrate during cool down, using the difference in thermal expansion coefficients. For the self-separation process, it is necessary to define the breakpoint between the substrate and the thick grown GaN-layer. This can be defined with different methods. It is possible to generate the breakpoint with a TiN layer which leads to a cavernous layer [4]. The deposition of a dielectric mask, as it is used for epitaxial lateral overgrowth could also lead to a perforated layer between the substrate and the thick GaN-layer [5]. All of these methods require additional ex-situ steps for preparing the freestanding GaN-substrate. Therefore we focused our studies on a self-separation process during cool down. To avoid additional ex-situ steps, we generate the perforated layer with in-situ deposited SiN-interlayers.

2. Experimental

The HVPE growth experiments have been performed in a commercial single wafer HVPE machine with horizontal quartz reactor. As usual, metallic Ga was transported by HCl gas to the substrate, whereas ammonia was used as nitrogen precursor. The Ga source was kept at 850°C, while the substrate zone was heated to 1010–1070°C. A freely adjustable mixture of N_2 and H_2 could be used as carrier gas to control the strain during growth. The reactor pressure was mostly kept around atmospheric pressure, to achieve a high growth rate.

By growing on quarters of 2 inch templates, up to 4 different templates could be overgrown simultaneously in one HVPE growth experiment, to get a fair comparison between the templates. The templates were grown on (0001) sapphire substrates in a AIXTRON 200/4 RF-S MOVPE system. Trimethylgallium, trimethylaluminium, ammonia and diluted silane were used as precursors for the template growth. The growth parameters were close to parameters for standard GaN growth in MOVPE. To achieve a smooth surface after the HVPE growth, all experiments have been carried out on slightly misoriented sapphire substrates [6]. The sapphire was first heated to 1200°C for thermal cleaning, afterward an AlN nucleation layer was deposited at 900°C. Finally, a thin GaN layer covers the nucleation layer, before the SiN-interlayers were deposited. To study the influence of the SiN-layers on the HVPE growth and the self-separation, the stack of SiN- and GaN-layer was varied to increase the separation probability.

3. Results and Discussion

3.1 MOVPE growth of SiN-layers

We started the investigation of the interlayers with the deposition of single SiN layers. First we studied the influence of reactor pressure, total flow, temperature and ammonia supply. The best deposition conditions could be achieved with a reactor pressure of 100 mbar, around 1100°C with a low ammonia supply, compared to standard GaN growth conditions. Our experiments exhibited, that the temperature mainly influences the deposition rate of the SiN-interlayer [7]. Therefore, we controlled the thickness of the interlayer

by the deposition time and kept the temperature constant. By using one SiN-interlayer, Fang et al. [8] reported a significant defect reduction. Our studies of single SiN-interlayer confirmed those results. We got a decrease in dislocation density with increasing SiN layer thickness. We estimated the dislocation density to a value of $2 \cdot 10^8\,\mathrm{cm}^{-2}$ with a deposition time of 6 min. Longer deposition times results in a rough and non coalesced surface morphology with a masked area on the bottom of a pit. The defect density was evaluated from atomic force micrographs were the dislocations were marked by chemical etching [9].

The SiN-coverage was estimated from the silicon incorporation in a n-doped layer grown with the same process parameters, by calculating the amount of silicon for one complete SiN monolayer. In addition, the coverage could be estimated from pictures of an optical or scanning electron microscope (Fig. 2). This is done by the measurement of the area of small pyramids grown after the SiN-interlayer divided by the hole area of the picture. These measurements confirmed the calculated values for the SiN-coverage.

The most important property of the separation layer is to generate a weak connection between the template and the the thick GaN-layer, as it is the case for TiN- or low temperature interlayers [10]. The second task is to admit an HVPE growth on top. Both major tasks are achievable by using SiN. As mentioned above, by increasing the SiN deposition time, we could achieve a higher coverage with non overgrown areas in MOVPE. However, we observed a bad separation by only increasing the thickness of one SiN-interlayer. To overcome the problems with only one interlayer, we started the deposition of multiple, low coverage SiN-layers with a short GaN growth in between (Fig. 1). The sample in those figures consist of six periods of SiN and GaN. To improve the lateral overgrowth, we doped the layers slightly with magnesium [11].

The use of multiple SiN interlayers leads to several effects. On the one hand, in Fig. 1, it is clearly seen, that overgrown holes developed, which leads to a visible disconnection. A comparable structure was achieved by Y. Oshima et al. [4] using a TiN interlayer for their separation process. This could be achieved by using a relatively low SiN coverage per layer. On the other hand, by increased coverage per layer of a factor of 1.5, the structure of the SiN-template changed completely (Fig. 2). Large areas of the surface are covered with SiN. The increased SiN deposition time causes a coverage of small pyramids and the base of larger pyramids. The distance of those larger pyramids is in the range of 4 µm. This is also suitable for the HVPE overgrowth.

3.2 HVPE growth on templates with SiN-layers

As mentioned above, up to four quarter wafers could be overgrown at the same time, to achieve the best comparability between different templates. We started with the growth of up to 120 µm thick layers on sapphire templates without cracks [12]. By the optimization of the process parameters, we could achieve a mirror like surface morphology [13]. With a further increase of layer thickness on bare templates, the cracking probability increases in the same way. Those cracks, that destroyed the samples, developed only during the

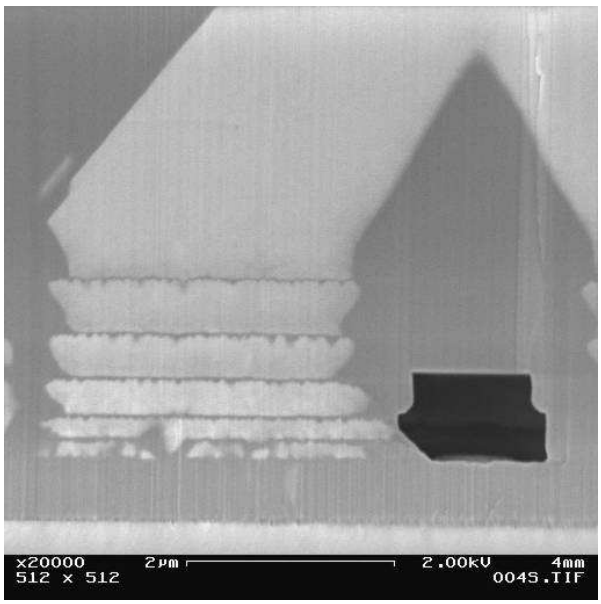

Fig. 1: SEM picture of the cross section of a sample with SiN-interlayers. Six SiN-interlayers are visible and form a cavernous layer, where the separation occured.

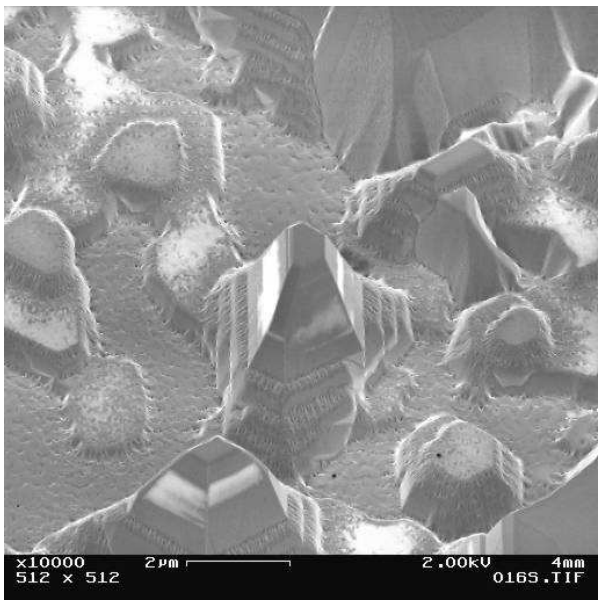

Fig. 2: SEM picture of the surface of a template with a higher SiN-coverage as in Fig. 1. The increased SiN-coverage leads to freestanding pyramids with large masked areas in between.

cool down, induced by the difference in the thermal expansion coefficients of sapphire and GaN.

These results show that the used parameters are suitable for the growth of thick layers. Moreover, we observed that SiN-interlayers lead to a significantly decreased cracking probability in thick GaN layers. This indicates that the SiN-interlayer influences the strain in the same way as it is the case on laterally overgrown templates.

With a layer thickness of approximately 300 µm, the first small area delamination processes were observed. The analysis of those separated small pieces exhibited, that the cracks propagate in the separation layer. Due to a strong connection between the substrate and the HVPE layer and the relatively low thickness of the HVPE layer, also vertical cracks developed. Hence, it is necessary to grow thick GaN-layers and reduce the bonding strength of the separation layer. First we increased the thickness of the layers to improve their stability for the separation process. Large self-separated freestanding samples wit a size of 15x25 mm, could be achieved with a HVPE grown thickness of 600 µm. By a further optimization of the growth parameters, we were able to grow 1.2 mm thick layers with a growth rate of approx. 250 µm/h. This increase of layer thickness tends to result in the separation of large freestanding samples (Fig. 3).

The rough backside, which can be seen in the picture, is caused by the separation layer. Also a high density of inverse pyramids is visible, which causes a change in the surface smoothness around the pyramids. This is also the reason for the incomplete separation of the 2 inch wafer. The crack occurs near the highest density of inverse pyramids (Fig.

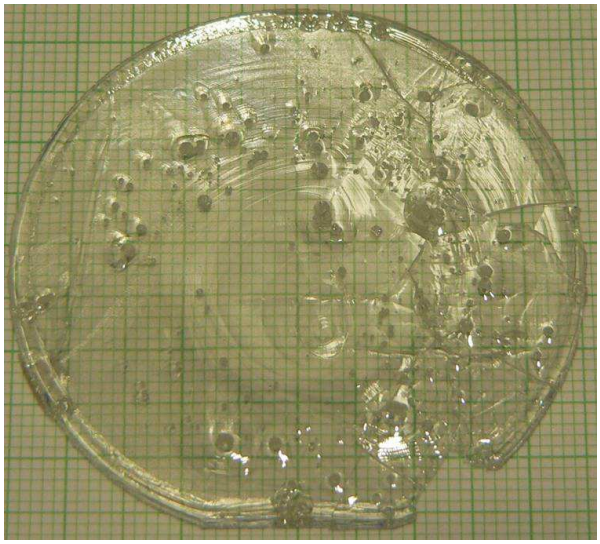

Fig. 3: Nearly full 2 inch self-separated wafer with a thickness of approximately 1 mm.

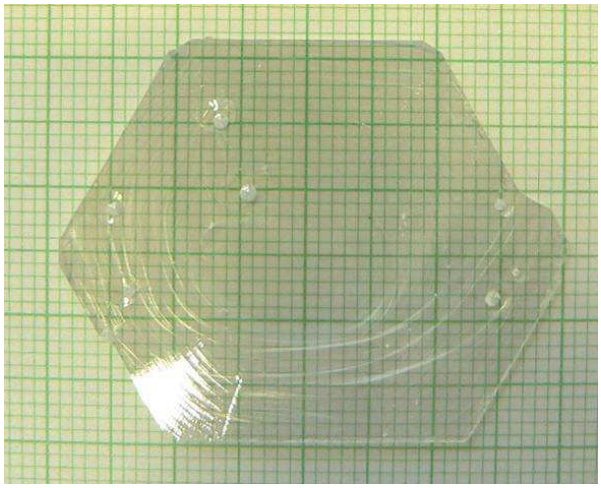

Fig. 4: Sample with a reduced pit density.

3). Parasitic depositions caused a change in diameter of the gas-inlet of the GaCl. This results in a reduced growth rate and a inhomogeneous thickness. Nevertheless, it was possible to separate more than 10 cm^2 out of the center of the sample with the largest thickness. This area is equivalent to a half 2 inch wafer (Fig. 4). We assume, that the lower pit density is caused by the lower growth rate.

In spite of the high growth rate and the partly high inverse pit density, excellent electrical and optical properties could be measured. On the 600 µm thick freestanding sample we found Hall mobilities up to 820 cm^2/Vs with a carrier concentration of approx. $1 \cdot 10^{16}\,cm^{-3}$ at room temperature measured and 3646 cm^2/Vs and $3.6 \cdot 10^{15}\,cm^{-3}$ at 85 K. The surface flatness of the freestanding samples is comparable to high quality MOVPE grown GaN layers, thus enabling the use of these samples for subsequent epitaxial steps without the need of surface polishing.

4. Conclusion

It was demonstrated that a single SiN-interlayer reduces the defect density by an order of magnitude. By further increase of the deposition time, non overgrown masked areas developed. By using those interlayers in a periodic stack, it was possible to generate a cavernous layer or larger masked areas with singe pyramids - both structures lead to a separation. The growth of a 1.2 mm thick layer on such a template resulted in almost 2 inch self-separated wafers. They exhibited excellent optical and electrical characteristics.

Acknowledgment

We gratefully acknowledge the steady support of these studies by Aixtron AG and in particular by D. Schmitz et al. This work was partially financially supported by the Bundesministerium für Bildung und Forschung.

References

[1] M. Hansen, P. Fini, L. Zhao, A.C. Abare, L.A. Coldren, J.S. Speck, S.P. DenBaars, *Appl. Phys. Lett.*, vol. 76, no. 5, pp. 529–531, 2003.

[2] C.R. Miskys, M.K. Kelly, O. Ambacher, M. Stutzmann, *phys. stat. sol. (c)*, vol. 0, no. 6, pp. 1627–1650, 2003.

[3] K. Motoki, T. Okahisa, N. Matsumoto, M. Matsushima, H. Kimura, H. Kasai, K. Takemoto, K. Uematsu, T. Hirano, M. Nakayama, S. Nakahata, M. Ueno, D. Hara, Y. Kumagai, A. Koukitz, H. Seki, *Jpn. J. Appl. Phys.*, vol. 40, no. 2B, pp. L140–L143, 2001.

[4] Y. Oshima, T. Eri, M. Shibata, H. Sunakawa, K. Kobayashi, T. Ichihashi, A. Usui, *Jpn. J. Appl. Phys.*, vol. 42, no. 1A/B, pp. L1–L3, 2003.

[5] S. Bohyama, H. Miyake, K. Hiramatsu, Y. Tsuchida, T. Maeda, *Jpn. J. Appl. Phys.*, vol. 44, no. 1, pp. L24–L26, 2005.

[6] F. Scholz, P. Brückner, F. Habel, M. Peter, K. Köhler, *Appl. Phys. Lett.*, vol. 87, pp. 181902, 2005.

[7] T. Böttcher, J. Dennemarck, R. Kröger, S. Figge, D. Hommel, *phys. stat. sol. (c)*, vol. 0, no. 7, pp. 2039–2042, 2003.

[8] X.L. Fang, Y.Q. Wang, H. Meidia, S. Mahajan, *Appl. Phys. Lett.*, vol. 84, no. 4, pp. 484–486, 2004.

[9] F. Habel, M. Seyboth, *phys. stat. sol. (c)*, vol. 0, no. 7, pp. 2448–2451, 2003.

[10] Yu.V. Zhilyaev, A.V. Nasonov, S.D. Raevski, S.N. Rodin, M.P. Shcheglov, V.Yu. Davydov, *phys. stat. sol. (a)*, vol. 195, no. 1, pp. 122–126, 2003.

[11] B. Beaumont, S. Haffouz, P. Gibart, *Appl. Phys. Lett.*, vol. 72, no. 8, pp. 921–923, 1998.

[12] E. Richter, Ch. Hennig, M. Weyers, F. Habel, J.-D. Tsay, W.-Y. Liu, P. Brückner, F. Scholz, Y. Makarov, A. Segal, J. Kaeppeler, *J. Crystal Growth*, vol. 277, pp. 6–12, 2005.

[13] P. Brückner, F. Habel, F. Scholz, *phys. stat. sol. (c)*, vol. 3, no. 6, pp. 1471–1474, 2006.

Optimization of GaN Growth Conditions for Improved Device Performance

Joachim Hertkorn

By accurately optimizing the growth conditions for an oxygen doped AlN nucleation layer and for the subsequent epitaxial process the crystal quality of our GaN could drastically be improved. In X-ray diffraction (XRD) analyses we observed FWHM values of 39 arcsec and 114 arcsec for the symmetric (004) and asymmetric (114) reflection, respectively. Consequently, the nominally undoped samples showed semi-insulating behavior in Hall-measurements. By in-situ deposition of a SiN interlayer, the dislocation density could be reduced by more than a factor of 2, reaching a value of $4 \cdot 10^8\ cm^{-2}$*. Samples with this low dislocation density showed an extremely narrow X-ray FWHM of 71 arcsec for the asymmetric (114) reflection along with a narrow linewidth of* $870\,\mu eV$ *in photoluminescence (PL) for the donor bound exciton (*D^0X*) at a temperature of 10 K. Atomic force microscopy (AFM) yielded a very low rms-roughness of about 0.14 nm across a* $4\,\mu m^2$ *scan area. Finally, the excellent crystal quality could be confirmed by growing AlGaN/AlN/GaN heterostructures with a low sheet resistance of* $330\,\Omega/\Box$*.*

1. Introduction

The growth of GaN is still known to be problematic because of the lack of lattice-matched substrates. Therefore a low-temperature nucleation layer consisting of AlN [1] or GaN [2] has to be applied as initial growth step before the deposition of the GaN material. With optimized growth conditions for the nucleation layer (NL) one has to find accurate growth conditions for the GaN-buffer layer which is responsible for the device performance. The grown material has to be optimized in terms of background doping and surface roughness, as well as excellent properties in X-ray diffraction and photoluminescence are desirable. Looking at those parameters one has to remember that the large lattice mismatch (13,8 %) between the GaN epitaxial layer and the applied sapphire substrate results in high dislocation densities up to $2 \cdot 10^9\,\mathrm{cm}^{-2}$ [3]. As this can be seen as a limitation for the performance of many GaN-based devices [4, 5, 6, 7] the in-situ deposition of a SiN interlayer [8, 9, 10, 11] is a simple method to reduce the dislocation density. The treatment of the GaN layer with ammonia (NH_3) and silane (SiH_4) leads to a fractional coverage of the surface with SiN which can act as a nano mask and influence the morphology of the overgrown GaN layer leading to a defect reduction.
In this study we investigate the optimization of the growth conditions for an oxygen doped AlN nucleation layer enabling the stable growth of high quality GaN. Therefore, we studied the influence of oxygen during the nucleation. Afterwards, we focus on the influence of the annealing step right after the nucleation layer deposition as well as the growth

parameters during the GaN-buffer layer deposition and the influence of a SiN interlayer on the dislocation density are under investigation. The increased carrier mobility in the AlGaN/AlN/GaN heterostructures which we finally used as a cross check for our material quality was a result of the defect reduction, as we will describe here.

2. Experimental

The samples were grown by metalorganic vapor phase epitaxy (MOVPE) in an AIXTRON 200/RF-S horizontal flow reactor. All layers were grown on 2" c-plane (0001) epi-ready sapphire wafers slightly miscut by about 0.3 ° towards a-plane using an oxygen doped AlN nucleation [12, 13]. Oxygen doping was done with a mixture of 0.3 % oxygen in nitrogen. Before deposition, the substrates went through in-situ annealing [14] at 1200 °C for 10 min in a hydrogen atmosphere. A reduced reactor pressure between 100 and 200 mbar and the standard precursors trimethyl-aluminum (TMAl), trimethyl-gallium (TMGa), and high purity ammonia were used to deposit the NL and the nominally undoped GaN layer, respectively. The carrier gas was Pd-diffused hydrogen. We fixed the GaN-buffer layer growth parameters in order to establish a high growth rate (1.9 µm/h). Hence we used a TMGa flow of 21 sccm (82 µmol/min) and a V/III-ratio of 1100. The temperature was set to 1140 °C. The GaN was deposited for 1 hour, so we had a buffer layer thickness of around 2 µm. The SiN intermediate layer was integrated after the optimization of the buffer layer growth conditions (sec. 6.).
The crystal quality of our layers was evaluated by high resolution X-ray diffraction (HRXRD) and low temperature (10 K) photoluminescence [15]. The HRXRD measurements were performed without any slits on the detector side. The dislocation density of our layers was determined by atomic force microscopy (AFM) after an HCl etch in our HVPE system [16, 17, 18]. The electrical properties were analyzed by van-der-Pauw Hall measurements at room temperature (295 K) and at liquid nitrogen temperature (77 K). The surface properties on a µm and nm scale were investigated by Nomarski differential interference contrast microscopy (DIC) and AFM, respectively.

3. Oxygen Doped AlN Nucleation

All samples were grown in a four step process (Fig. 1). After thermal cleaning we cooled down to 950 °C and started nucleation. Next was a 360 sec annealing step under hydrogen atmosphere and constant ammonia flow. Here the temperature was set to 1140 °C. Subsequently 2 µm thick GaN layers were deposited under the growth conditions described above. To optimize the AlN nucleation layer, the oxygen content and the ammonia flow, the reactor pressure and the thickness of the layer were varied controlling in particular four figures of merit: The FWHM of the rocking curves of the GaN (002) and (114) peaks, the FWHM of the donor bound exciton measured in PL at 10 K and the surface flatness. In our initial experiment on the AlN nucleation we used a reactor pressure of 100 mbar, a high ammonia flow of 2000 sccm and a TMAl flow of 17 sccm. The massflow of our oxygen source was set to 8 sccm resulting in a calculated O_2-concentration of about 3 ppm. The deposition time was 10 min. As we observed prereactions between NH_3 and TMAl,

Table 2: Summary of the measured FWHM in X-ray and PL after each optimization step.

Optimized Step	X-ray-FWHM (arcsec) (002)-reflex	(114)-reflex	PL-FWHM (μeV) D^0X-Exciton
2	66	137	1590
3	44	117	1650
4	43	116	1190
SiN	82	71	870

we fixed the TMAl flow to 25 sccm (TMAl/O_2 ≈ 5.7) and reduced the ammonia flow to 250 sccm. Finally we could achieve samples with extremely narrow X-ray peaks along with an acceptable surface roughness as observed by DIC (Fig. 2). The PL linewidth was quite promising (Table 2). In order to investigate the influence of the oxygen doping on the nucleation layer, we fixed the optimum parameters as described above and set the oxygen flow to 5 sccm. This yields a calculated O_2-concentration of 2 ppm. Even for such small concentrations, the oxygen influence on the subsequently deposited GaN is significant. In X-ray a linewidth of about 400 arcsec for the (002)-reflection was determined along with a rough surface, resulting in a large rms roughness value of 4.9 nm across a 100 μm^2 scan area. In comparison, the sample with higher oxygen flow showed a relatively smooth surface in AFM with a rms roughness value of 1.7 nm. This experiment demonstrates impressively the need of low oxygen doping during the growth of the AlN nucleation layer. We suppose that the formation of an aluminumoxynitride layer close to the Al_2O_3-substrate is the explanation for our observations. As the reproducibility was improved with a temperature of 920 °C and 10 sccm oxygen flow during the nucleation layer growth, we used these parameters during the following experiments.

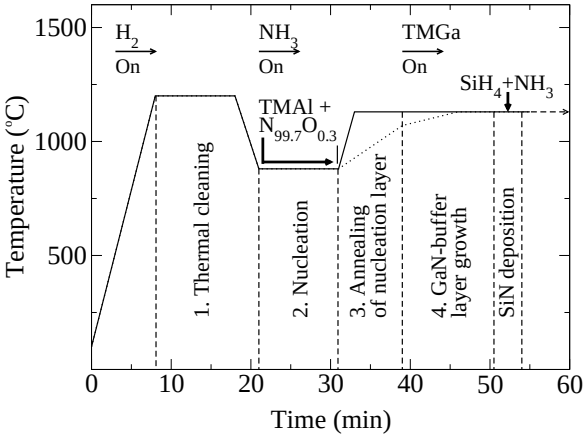

Fig. 1: Temperature ramps during our four step growth process. The temperatures, the ramping-slope and the deposition times were varied in the experiment.

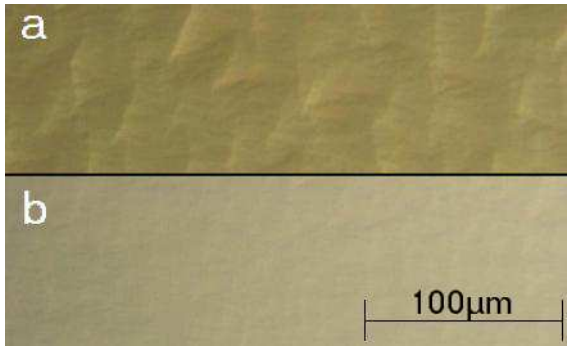

Fig. 2: DIC pictures of two samples with non optimized (a) and optimized (b) annealing step conditions, respectively.

4. Optimization of the Annealing Step After the NL Growth

After optimization of the nucleation layer we studied the influence of annealing as the third process step (Fig. 1) on the GaN quality and surface roughness. Before the optimization of this process step we were used to ramp the reactor temperature to 1140 °C after the deposition of the nucleation layer. Finally the GaN growth was started by opening the TMGa valve after 6 minutes annealing at the chosen temperature (Fig. 1). With these annealing conditions we observed a patterned surface like it is depicted in Fig. 2 (a).
In a first optimization step, we implemented a temperature ramp from 920 °C to 1100 °C in 5 min. There was no additional annealing time with constant temperature. The final GaN growth temperature of 1140 °C was reached during the growth after a second ramp of 7 min. As this improved the crystal quality, we reduced the duration of the first ramp in two steps to 2 min and finally 40 sec. A further reduction was impossible due to the limited heating power of 20 kW. With this extremely short temperature ramp of 40 sec we achieved a smooth surface as illustrated in Fig. 2 (b). The remaining roughness is hardly visible in the interference contrast microscopy. AFM yielded a rms roughness value of 0.9 nm across a 100 μm^2 scan area. The FWHM of the (114)-reflection was hardly affected (Table 2) whereas the FWHM of the (002)-reflection was reduced to the very small value of 44 arcsec. This could mean that under the given conditions the number of threading dislocations is more reduced than that of the edge dislocations [19]. Consequently, edge dislocations might be responsible for the remaining surface roughness in the nanometer range [13, 20]. The influence of the changed annealing conditions on the PL was negligible (Table 2). In agreement with Sugiura et al. we think that mechanisms like recrystallization, decomposition and surface stress relief might be responsible for the discussed effects.

5. Optimization of the GaN Growth Conditions

Finally, we studied the growth conditions during the GaN-buffer layer deposition. As AlGaN/AlN/GaN heterostructures should be used as a probe for our GaN material quality, we decreased the reactor pressure to 100 mbar during the whole growth process as it is normal to prevent prereactions between TMAl and NH_3 during the Al(Ga)N growth. This resulted in an increased GaN growth rate of 2.4 µm/h. The reason might be the increased gas flow speed in the reactor accelerating the material transport.
Due to the changed growth conditions the crystal properties were improved. We observed surface smoothing in the µm and nm ranges, as well as reduced values for the FWHM in the X-ray measurements (Table 2). The rms value determined by AFM across a 100 μm^2 scan area could be reduced to 0.5 nm. The PL linewidth of the D^0X-peak was in the range of 1.2 meV at 10 K. The layer was nominally undoped and showed semi-insulating behavior in van-der-Pauw resistivity measurements. Based on these improvements all samples in the following experiments were grown with a reactor pressure of 100 mbar.

6. Defect Reduction with SiN as Interlayer

Although most properties of the GaN layers could be dramatically improved as discussed above, we still found a relatively high dislocation density ($1 \cdot 10^9\,cm^{-2}$) in those optimized

GaN samples. In order to reduce the dislocation density we ran experiments with a defect-terminating SiN interlayer, which was deposited after the growth of around 500 nm GaN material. For its deposition we decreased the NH_3 flow to 500 sccm, stopped the Ga flow and opened the silane source. Information on the type of dislocation which was reduced most efficiently was obtained by X-ray measurements using the symmetric (002)-reflection and the asymmetric reflections (104) and (114), respectively, as proposed by Heying et al. It is recognized from Fig. 3 that the SiN interlayer was highly effective reducing the dislocation density. The EPD was reduced to $4 \cdot 10^8\,\mathrm{cm}^{-2}$. Based on X-ray measurements we concluded, that mainly edge dislocations were reduced by the SiN interlayer as the asymmetric reflections became extremely narrow. We observed a linewidth of 71 arcsec (114-reflection) and 45 arcsec (104-reflection), respectively. Compared to GaN without a SiN interlayer this was almost a factor of two (Table 2). Thus there is agreement between X-ray measurements and etch pit densities. In addition the reduced edge dislocation density led to a smoothing of the surface in the nanometer range. Finally we measured an extremely low rms roughness value of about 0.14 nm across a $4\,\mu\mathrm{m}^2$ scan area. A slightly increased roughening visible in DIC (not shown) might be traced back to the SiN masking. The excellent crystal quality is confirmed by PL (Fig. 3). The spectrum is dominated by the neutral donor-bound exciton (D^0X) line at 3.486 eV representing the dominant transition and the free exciton (X_A and X_B) emission [15]. Particularly the D^0X linewidth of 870 μeV demonstrates the good crystal quality of these layers. To compare, it should be noted that FWHM values in the range below 1 meV have been reported from samples grown by HVPE [21] with comparably thick layers of several tens of μm but not from samples grown in MOVPE as in the present case. [19]. One disadvantage of the SiN interlayer was the background doping concentration determined by van-der-Pauw Hall measurements (n=$6 \cdot 10^{17}\,\mathrm{cm}^{-3}$; μ=$171\,\mathrm{cm}^2/\mathrm{Vs}$). Although no influence of the background doping on the optical properties was visible (Fig. 3) the SiN interlayer

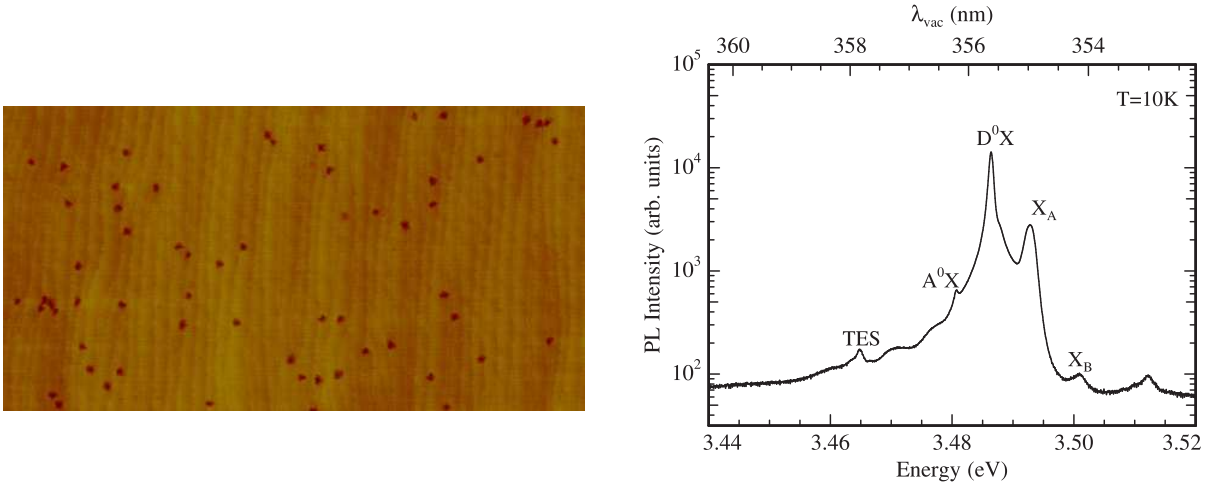

Fig. 3: Left: EPD of a nominally undoped GaN sample with SiN interlayer. The scan size was approximately $2.5\,\mu\mathrm{m} \times 5\,\mu\mathrm{m}$. Right: PL spectrum near the band gap measured at low temperature (10K). X_A and X_B refer to A- and B-valence band exciton, respectively. D^0X denotes donor bound exciton emission with its two-electron satellites (TES).

should not be implemented in HEMT structures, where a semi-insulating buffer is of great importance [22]. Only if the spacing between the SiN layer and the 2DEG would be large enough, carriers from the interlayer would not affect the device performance.

7. Device Performance

We already verified the good crystal quality of our GaN samples with the standard methods like DIC, AFM, HRXRD, PL and Hall. Additionally, we studied their influence on AlGaN/AlN/GaN high electron mobility transistor (HEMT) structures, which are well known as devices with high sensitivity in terms of crystal quality. The surface roughness as well as the dislocation density are only two figures of merit with crucial influence on the carrier mobility in the 2DEG. As we optimized both, we could realize HEMT structures (without SiN interlayer) with a low sheet resistance of $330\,\Omega/\square$ (295 K). In Hall measurement we determined the 2DEG carrier density to $1.1 \cdot 10^{13}\,\mathrm{cm}^{-2}$ and measured a mobility of $1720\,\mathrm{cm}^2/\mathrm{Vs}$. At low temperature (77 K), we determined a mobility of more than $10000\,\mathrm{cm}^2/\mathrm{Vs}$ with a carrier density of $1.3 \cdot 10^{13}\,\mathrm{cm}^{-2}$ ($50\,\Omega/\square$). Although these values are quite promising they don't reach the best values of Miyoshi et al. ($302\,\Omega/\square$) as they reported a dislocation density of about $3 \cdot 10^8\,\mathrm{cm}^{-2}$ in their HEMT samples [23]. If we include our SiN-Interlayer in the structure reducing the dislocation density to $4 \cdot 10^8\,\mathrm{cm}^{-2}$ we can determine a sheet resistance of about $310\,\Omega/\square$, what would be in nice agreement with Miyoshi et al. As our X-ray peaks are reported to be very narrow it was possible to get excellent omega-2-theta scans of our HEMT structure (Fig. 4). The thickness fringes of the 30 nm thick AlGaN ($\approx$ 30% Al) cap are noted at the low and high-angle side, respectively. Additionally one can see the AlN peak from the nucleation layer and the peak from the GaN-buffer. The large number of visible fringes confirm nicely our excellent crystal quality [24, 25] and the abruptness of our AlGaN/AlN/GaN-interfaces.

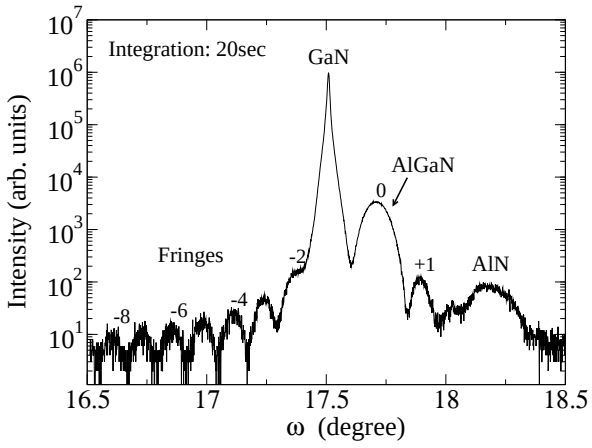

Fig. 4: X-ray diffraction profile of an AlGaN/AlN/GaN HEMT structure.

8. Summary

We demonstrated the optimization of the growth process for our nucleation layer and GaN-buffer. We found that oxygen doping during the nucleation process is of tremendous importance as well as prereactions between TMAl and ammonia were found to be critical. Additionally we demonstrated that the temperature ramp subsequent to the nucleation affects the surface roughness and the crystal quality of the GaN-buffer. We found that a very fast temperature ramp and short annealing time yields the best results. In terms of buffer layer optimization we concluded to grow with a reduced reactor pressure of 100 mbar, resulting in a highly efficient growth with further improved crystal quality. Finally we could reduce the dislocations in our samples by using an in-situ deposited SiN interlayer. With this low dislocation density we could achieve extremely good optical quality material, which was illustrated by a PL linewidth of the donor-bound exciton of 870 µeV (10K). As we used HEMT structures as a probe for our optimization steps, we could confirm excellent crystal properties.

9. Acknowledgment

This research was financially supported by Osram Opto Semiconductors and the Bundesministerium für Bildung und Forschung (BMBF). The sample characterization by M. Feneberg, E. Fuentes, C. Gao, and H. Xu is gratefully acknowledged.

References

[1] H. Amano, N. Sawaki, I. Akasaki, Y. Toyoda, *Appl. Phys. Lett.*, vol. 48, no. 5, pp. 353–355, 1986.

[2] S. Nakamura, *Jpn. J. Appl. Phys.*, vol. 30, no. 10A, pp. L1705-L1707, 1991.

[3] S.D. Lester, F.A. Ponce, M.G. Crawford, D.A. Steigerwald, *Appl. Phys. Lett.*, vol. 66, no. 10, pp. 1249–1251, 1995.

[4] T. Sugahara, H. Sato, M. Hao, Y. Naoi, S. Kurai, S. Tottori, K. Yamashita, K. Nishino, L.T. Romano, S. Sakai, *Jpn. J. Appl. Phys.*, vol. 37, no. 4A, pp. L398–L400, 1998.

[5] C.S. Tomiya, H. Nakajima, K. Funato, T. Miyjima, K. Kobaijashi, T. Hino, S. Kijima, T. Assano, M. Ikeda, *phys. stat. sol. (a)*, vol. 188, no. 1, pp. 69–72, 2001.

[6] D. Zanato, S. Gokden, N. Balkan, B.K. Ridley, W.J. Schaff, *Semicond. Sci. Technol.*, vol. 19, pp. 427–432, 2004.

[7] M. Miyoshi, T. Egawa, H. Ishikawa, K.-I. Asai, T. Shibata, M. Tanaka, O. Oda, *J. Appl. Phys.*, vol. 98, pp. 063713-1–063713-5, 2005.

[8] S. Tanaka, M. Takeuchi, Y. Aoyagi, *Jpn. J. Appl. Phys.*, vol. 39, no. 8B, pp. L831–L834, 2000.

[9] K.J. Lee, E.H. Shin, K.Y. Lim, *Appl. Phys. Lett.*, vol. 85, no. 9, pp. 1502–1504, 2004.

[10] K. Engl, M. Beer, N. Gmeinwieser, U.T. Schwarz, J. Zweck, W. Wegscheider, . Miller, A. Miler, H.-J. Lugauer, G. Brüderl, A. Lell, V. Härle, *J. Crystal Growth*, vol. 289, pp. 6–13, 2006.

[11] O. Contreras, F.A. Ponce, J. Christen, A. Dadgar, A. Krost, *Appl. Phys. Lett.*, vol. 81, no. 25, pp. 4712–4714, 2002.

[12] B. Kuhn, F. Scholz, *phys. stat. sol. (a)*, vol. 188, no. 2, pp. 629–633, 2001.

[13] J. Hertkorn et al., to be published in *J. Crystal Growth*, 2007.

[14] J.-H. Kim, S.C. Choi, K.S. Kim, G.M. Yang, C.-H. Hong, K.Y. Lim, H.J. Lee, *Jpn. J. Appl. Phys.*, vol. 38, no. 5A, pp. 2721–2724, 1999.

[15] K. Kornitzer, T. Ebner, M. Grehl, K. Thonke, R. Sauer, C. Kirchner, V. Schwegler, M. Kamp, M. Leszczynski, I. Grzegory, S. Porowski, *phys. stat. sol. (b)*, vol. 216, pp. 5–9, 1999.

[16] T. Hino, S. Tomiya, T. Miyajima, K. Yanashima, S. Hashimoto, M. Ikeda, *Appl. Phys. Lett.*, vol. 76, no. 23, pp. 3421–3423, 2000.

[17] T. Miyajima, T. Hino, S. Tomiya, K. Yanashima, H. Nakajima, T. Araki, Y. Nanishi, A. Satake, Y. Masumoto, K. Akimoto, T. Kobayashi, M. Ikeda, *phys. stat. sol. (b)*, vol. 228, no. 2, pp. 395–402, 2001.

[18] F. Habel, M. Seyboth, *phys. stat. sol. (c)*, vol. 0, no. 7, pp. 2448–2451, 2001.

[19] B. Heying, X.H. Wu, S. Keller, Y. Li, D. Kapolnek, B.P. Keller, S.P. DenBaars, J.S. Speck, *Appl. Phys. Lett.*, vol. 68, no. 23, pp. 643–645, 1996.

[20] L. Sugiura, K. Itaya, J. Nishio, H. Fujimoto, Y. Kokubun, *J. Appl. Phys.*, vol. 82, pp. 4877–4882, 1997.

[21] P. Brückner et al., to be published in *J. Crystal Growth*, 2007.

[22] Z. Bougrioua, M. Azize, A. Jimenez, A-F. Braña, P. Lorenzini, B. Beaumont, E. Muñoz, P. Gibart, it phys. stat. sol. (c), vol. 2, no. 7, pp. 2424–2428, 2005.

[23] M. Miyoshi, A. Imanishi, T. Egawa, H. Ishikawa, K.-I. Asai, T. Shibata, M. Tanaka, O. Oda, *Jpn. J. Appl. Phys.*, vol. 44, no. 9A, pp. 6490–6494, 2005.

[24] A. Torabi, P. Ericson, E.J. Yarranton, W.E. Hoke, *J. Vac. Sci. Technol. B*, vol. 20, pp. 1234–1237, 2002.

[25] N. Tang, B. Shen, M.J. Wang, Z.J. Yang, K. Xu, G.Y. Zhang, T. Lin, B. Zhu, W.Z. Zhou, J.H. Chu, *Appl. Phys. Lett.*, vol. 88, pp. 172115-1–172115-3, 2006.

Properties of Semipolar GaInN/GaN Light Emitting Diodes on Selectively Grown GaN Stripes

Thomas Wunderer

Semipolar GaInN/GaN light emitting diodes (LEDs) were investigated as possible candidates for high-brightness devices even in the long wavelength regime. To combine the high material quality known from c-GaN and the advantage of a reduced piezoelectric field, the LED structures were realized on the $\{1\bar{1}01\}$ *side facets of selectively grown GaN stripes that have a triangular shape. Time-resolved and locally resolved photoluminescence (PL) measurements show drastically reduced lifetimes for the semipolar sample of only 650 ps at 4 K whereas we found lifetimes exceeding 50 ns for a polar reference sample. Furthermore, more than a doubling of the PL intensity and a significantly reduced blue shift of the peak wavelength with increasing excitation power provides further evidence for the presence of reduced piezoelectric fields in the semipolar sample. Bright blue light emission with powers as high as* $700\,\mu W$ *and 3 mW could be achieved in electroluminescence measurements under dc conditions for 20 and 110 mA, respectively.*

1. Introduction

GaN-based light emitting devices are still going on to revolutionize general lighting, applications in the automotive industry and data storage. In spite of the high performance achieved up to now, the optical efficiency of current commercially available (Al,Ga,In)N LEDs is limited by negative physical properties caused by the crystal structure and is found to decrease with increasing operational wavelength [1]. This is in large part caused by the local separation of electrons and holes in the quantum wells (QWs) as a consequence of strong internal piezoelectric fields in the biaxially compressively strained GaInN QWs. Besides the reduced recombination probability and the increased recombination time, this phenomenon, also known as the quantum confined Stark effect (QCSE), leads to a red-shift of the effective emission wavelength.

To circumvent these negative effects on the luminescence efficiency, it is highly desirable to grow GaInN/GaN heterostructures with reduced or completely without internal piezoelectric fields. This is made possible by rearranging the biaxial strain to planes other than the commonly used [0001] crystal plane (c-plane) [2]. Several groups are currently dealing with this subject by growing heterostructures on the r-plane of sapphire, for instance, in which case GaN grows along the $\langle 11\bar{2}0\rangle$ direction (a-direction) [3, 4]. Other approaches make use of more exotic substrates like $LiAlO_2$ [5], on which pure m-plane GaN $\{1\bar{1}00\}$ growth has been achieved. However, up to now the crystal quality of layers grown on these substrates does not compete with that obtained on the more commonly used c-plane sapphire or SiC wafers, which still limits the optical performance of respective LEDs [6].

These problems may be overcome by starting the epitaxial growth in the c-direction, and forming then GaN stripes with less polar side facets by selective epitaxy. QWs and even complete LED structures can then be grown on these facets [7, 8, 9, 10]. Depending on the stripe orientation and growth conditions, different crystal facets can be achieved which possess reduced or even vanishing polarization fields.

2. Fabrication of Semipolar GaInN/GaN Stripe LEDs

The samples were grown by low pressure metalorganic vapor phase epitaxy (MOVPE). First, 1.6 µm thick GaN templates were grown on c-plane sapphire. These were subsequently structured using SiO_2 stripes oriented along the $\langle 11\bar{2}0\rangle$ direction, fabricated by plasma enhanced chemical vapor deposition (PECVD), optical lithography and reactive ion etching (RIE). The parameters of the second epitaxial step have been tailored to grow triangularly shaped n-doped GaN stripes in the several µm wide mask openings which have $\{1\bar{1}01\}$ side facets as the most stable surface. Thereafter, five GaInN quantum wells were grown covered by a GaN:Mg layer (Fig. 1). Circular mesa structures with diameters between 70 and 140 µm were realized by chemically assisted ion beam etching (CAIBE). For simple and highly reflective contacts, electron beam deposited indium (1 µm) was used for the p-GaN as well as for the n-GaN metallization without alloying.

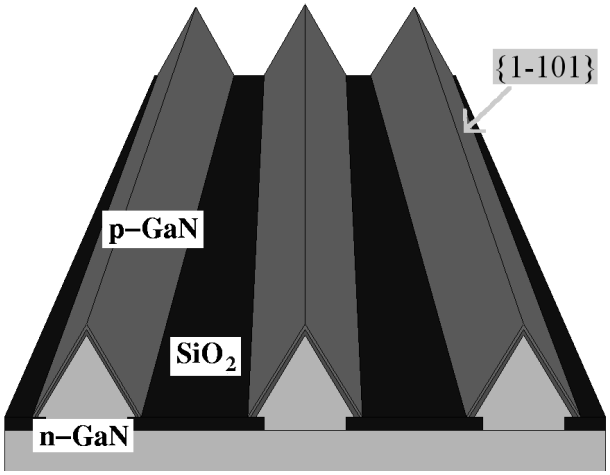

Fig. 1: Schematic sketch of the semipolar LED structure.

3. Mg-doped GaN: Problems and Solutions

An important aspect, which requires careful optimization, is the growth of the p-type regions. Depending on the magnesium fraction we found a very strong anisotropic growth behavior for the Mg-doped top layer. Preferential lateral growth appears when using growth parameters known from c-plane epitaxy. This results in an extremely thin cover layer at the apex of the stripes. Without Mg doping, we found preferential growth along the c-direction on the top areas.

Since Mg is needed for the p-type doping of GaN and due to the fact that the growth rate at the partially flat top is lower than on the side facets, there is a risk for electrical shorts

at the top when the metallization is in direct contact with the n-GaN or the QWs. Indeed, we observed high leakage currents of more than 5 mA @ -2 V for such devices. Therefore we developped, on the one hand, an additional process to achieve an electrically isolating Al_2O_3 coating on the apex of the stripe. This was done by spinning a thin fluid photo resist onto the sample. The resist covers the apex only with a thin film, in contrast to the gap between the stripes where it is relatively thick. Thereon the apex is freed from the resist in an O_2 plasma asher und coated by sputtering Al_2O_3 under a tilted position. After a lift-off process the isolating coating remains only on the apex. On the other hand, we optimized our epitaxial growth process in order to get an appropriate magnesium fraction into the top layer in combination with a closed apex. Therefore, we developed a more-step process with different Mg-concentrations to achieve a fully closed GaN:Mg top layer. Of course, this in-situ step is the favored procedure (see Fig. 2).

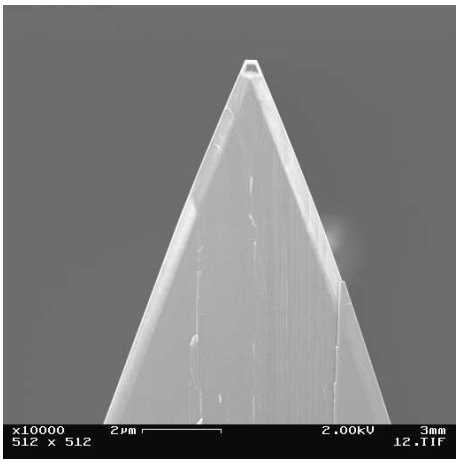

Fig. 2: More-step growth with different Mg-concentrations to achieve fully closed GaN:Mg top layer.

4. Luminescence Properties

To investigate the luminescence properties of the semipolar sample time-resolved photoluminescence and time-integrated electroluminescence measurements were performed. A c-plane reference sample with the same structural and compositional properties was used in order to allow for a reliable comparison.

4.1 Time-resolved photoluminescence

The micro-PL investigations were performed in a helium-flow cryostat at a temperature of 4 K. The laser excitation was realized by frequency doubling (350-500 nm) the output of a tunable Ti:Sapphire laser system which provides 120 fs pulses with a pulse repetition time of 13.1 ns. An excitation wavelength of 380 nm was chosen in order to quasi-resonantly excite the GaInN QW layers. The laser emission could be focused down to a diameter of approximately 1 µm using a long-working-distance 50x microscope objective mounted on a piezo-based actuator which is capable of a spatial resolution of 50 nm. The sample region of interest could be accurately selected as the cryostat can be moved both horizontally and vertically using two orthogonally mounted stepper motors each with an effective spatial

resolution of 50 nm. In the case of the semipolar stripe sample a special holder with a 60° sample mounting plane was used in order to match the triangularly shaped semipolar stripe edge facet angle and to thereby achieve sample excitation and PL collection normal to the stripe edge surface. The PL was dispersed using a 0.75 m spectrometer and detected using either a liquid-nitrogen-cooled charge-coupled-device camera when recording time-integrated spectra, or a fast avalanche photodiode with a time resolution of 40 ps when performing time-resolved photoluminescence (TRPL) via the time correlated single photon counting technique.

Theoretical calculations have predicted a reduced piezoelectric field on the $\{1\bar{1}01\}$ side facets of selectively grown GaN stripes [2, 11, 12]. Thus, the local separation of electrons and holes in the strained GaInN/GaN QWs should be reduced with respect to conventional c-plane LEDs and consequently an enhanced recombination probability should be found. Hence, besides a reduced carrier lifetime an increased luminescence intensity is expected for the semipolar stripe LEDs.

Actually, both aspects could be verified. Fig. 3 a) shows the TRPL intensity of the semipolar sample at an excitation power of 200 µW, a power which corresponds to a power density of approximately 25 kW/cm^2. At this excitation power density at the peak wavelength of 432 nm, the decay time was determined to be 650 ps at 4 K.

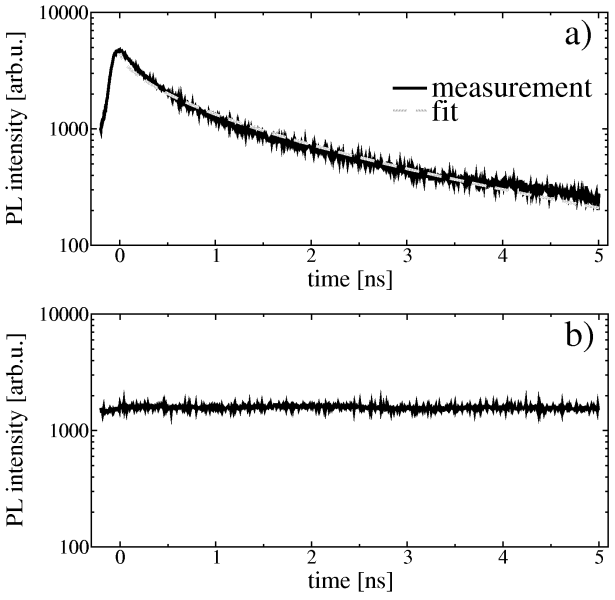

Fig. 3: a) PL decay of the semipolar LED measured at the peak wavelength and an excitation power of 200 µW at 4 K. The decay time is determined to be 650 ps.
b) PL decay of the polar LED measured at the peak wavelength and an excitation power of 200 µW at 4 K. The PL decay time in this case is > 50 ns.

The values were determined by fitting the measured data using the equation

$$I(t) = I_0 \exp\left[-\left(\frac{\mathrm{t}}{\tau}\right)^{\beta}\right], \tag{1}$$

where $I(t)$ is the PL intensity as a function of time and β can vary between 0 and 1. The PL kinetics can be well described by this stretched exponential, which is typically used to describe disordered systems. Nanoscale fluctuations of the indium concentration can produce forms of disordering that are responsible for the non-monoexponential decay observed from GaInN-LEDs [13].

In contrast, very long decay times of more than 50 ns [14] are observed on the *c*-plane reference sample (Fig. 3 b)). Such data are not unusual for high quality, relatively thick GaInN/GaN QWs emitting within this wavelength range [15, 16] and emphasize the fact that the presence of a high piezoelectric field increases the radiative lifetime.

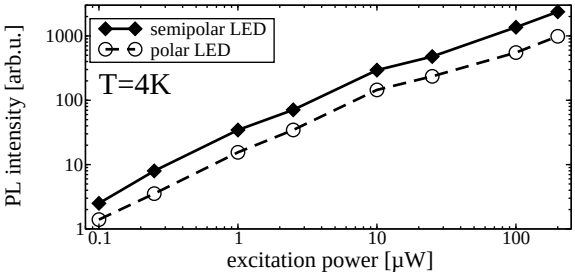

Fig. 4: Integrated PL intensity of the semipolar and polar LED structures measured at 4 K. The emission wavelength can be extracted from Fig. 5.

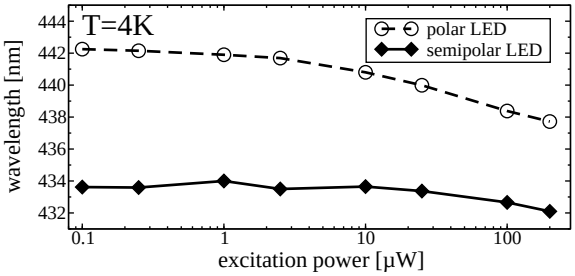

Fig. 5: PL peak shift due to screening of the built-in electric fields for both the semipolar and polar LEDs.

Analyzing the integrated PL intensity of both LED structures (Fig. 4), we found more than twice the optical output power of the semipolar sample than that of the polar sample across the investigated excitation range from 100 nW to 200 µW. This is in good agreement with that predicted by theoretical calculations [11, 12]. This significant improvement is primarily believed to originate from the reduced piezoelectric field.

Free photoexcited carriers in the QWs are expected to lower the influence of the QCSE by screening. This can also give rise to a decrease in PL decay time and to a blueshift of the peak emission wavelength with increasing excitation power.

Indeed, no significant change of the decay time with increasing excitation power could be observed for the semipolar LED. Also, the PL peak position of the semipolar sample shows a much weaker shift with excitation power as compared to the reference (Fig. 5) which emphasizes the proposition that the piezoelectric field is reduced on the $\{1\bar{1}01\}$ side facets of the GaN stripes.

4.2 Time-integrated electroluminescence

The electroluminescence characteristics of the diodes were quantified by on-wafer probing of the devices. The measurement of the optical output power was performed with an integrating sphere and a calibrated Si photo diode. For the electroluminescence spectra light was coupled into a glass fiber and analysed with an Ando AQ-6315A optical spectrum analyser. All measurements were carried out at room temperature.

Semipolar LEDs with a completely closed GaN:Mg top layer show low leakage currents in the range of 200-300 pA @ -2 V. As indium is used for the *p*- and *n*-contacts, the *I*-*V* characteristic is not optimized for operation in forward direction yet. A more sophisticated metallization, e.g. Ni/Au in combination with a highly reflective layer and Ti/Al/Ni/Au for the *p*- and *n*-contact, respectively, should lead to a further improvement of the electrical properties.

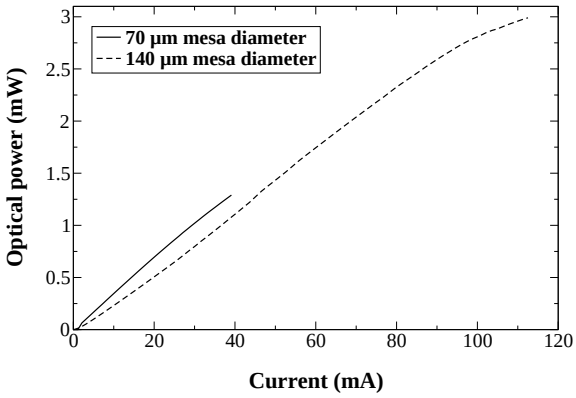

Fig. 6: Optical output power of semipolar facet LED with circular shaped mesa with 70 and 140 µm diameter.

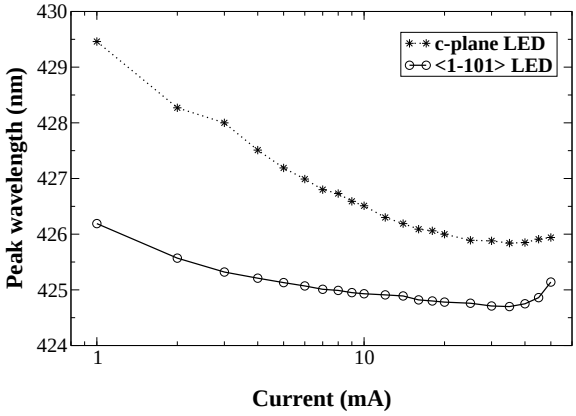

Fig. 7: Shift of EL wavelength caused by screening effects of the electrical field; comparison between polar and semipolar facet LED for currents between 1 and 50 mA.

In Fig. 6 the optical output power under dc operation is shown for devices with mesa diameters of 70 and 140 µm. Bright electroluminescence of 700 µW @ 20 mA and up to 3 mW @ 110 mA at a wavelength of 425 nm could be achieved on-wafer under dc conditions confirming the good performance of our LEDs.

On increasing injection current, a blue shift of the effective emission wavelength is expected due to screening effects of the electrical field. According to this, the shift for our LEDs should be smaller than that known from *c*-plane LEDs because of a reduced piezoelectric field. Actually, this could be verified (fig. 7). The wavelength shift for dc currents ranging from 1 to 50 mA was 1.5 nm for our semipolar LEDs in comparison to 3.5 nm for our reference polar *c*-plane LEDs. Similar to the much weaker wavelength shift in photoluminescence, this value fits well to theoretical data, where a field reduction by a factor of 2.8 is predicted for our semipolar facets [2].

5. Conclusion

In summary, we have reported on the properties of semipolar blue GaInN/GaN MQW LEDs realized on the $\{1\bar{1}01\}$ side facets of selectively grown GaN stripes running along $\langle 11\bar{2}0\rangle$. Time-resolved photoluminescence measurements showed relatively short decay times of 650 ps at an excitation power of 200 µW at 4 K for the semipolar sample while decay times > 50 ns were determined for the polar *c*-plane LED. Furthermore, the integrated PL intensity of the semipolar sample is observed to be more than twice that of the polar reference sample over the three orders of magnitude power range. CW on-wafer optical output powers as high as 700 µW and 3 mW were measured in electroluminescence for drive currents of 20 mA and 110 mA, respectively. A reduced wavelength shift due to screening effects could be observed in both luminescence experiments and confirms the reduced piezoelectric field in our LED structures.

Acknowledgment

We would gratefully acknowledge the cooperation with Gareth J. Beirne, Michael Jetter and Peter Michler from the Institut für Strahlenphysik at the University of Stuttgart and Martin Feneberg and Klaus Thonke from the Institute of Semiconductor Physics at the Ulm University.

References

[1] J. Edmond, A. Abare, M. Bergman, J. Bharathan, K.L. Bunker, D. Emerson, K. Haberern, J. Ibbetson, M. Leung, P. Russel, D. Slater, "High efficiency GaN-based LEDs and lasers on SiC", *J. Cryst. Growth*, vol. 272, pp. 242–250, 2004.

[2] T. Takeuchi, H. Amano, I. Akasaki, "Theoretical Study of Orientation Dependence of Piezoelectric Effects in Wurtzite Strained GaInN/GaN Heterostructures and Quantum Wells", *Jpn. J. Appl. Phys.*, vol. 39, pp. 413–416, 2000.

[3] H. Ng, "Molecular-beam epitaxy of GaN/$Al_xGa_{1-x}N$ multiple quantum wells on *R*-plane ($10\bar{1}2$) sapphire substrates", *Appl. Phys. Lett.*, vol. 80, pp. 4369–4371, 2002.

[4] M. Craven, P. Waltereit, F. Wu, J. Speck, S. DenBaars, "Characterization of *a*-Plane GaN/(Al,Ga)N Multiple Quantum Wells Grown via Metalorganic Chemical Vapor Deposition", *Jpn. J. Appl. Phys.*, vol. 42, pp. L235–L238, 2003.

[5] P. Waltereit, O. Brandt, A. Trampert, H. Grahn, J. Menniger, M. Ramsteiner, M. Reiche, K. Ploog, "Nitride semiconductors free of electrostatic fields for efficient white light-emitting diodes", *Nature*, vol. 406, pp. 865–868, 2000.

[6] A. Chakraborty, B. Haskell, H. Masui, S. Keller, J. Speck, S. DenBaars, S. Nakamura, U. Mishra, "Nonpolar *m*-Plane Blue-Light-Emitting Diode Lamps with Output Power of 23.5 mW under Pulsed Operation", *Jpn. J. Appl. Phys.*, vol. 45, pp. 739–741, 2006.

[7] T. Takeuchi, S. Lester, D. Basile, G. Girolami, R. Twist, F. Mertz, M. Wong, R. Schneider, H Amano, I. Akasaki, "Polarization Control in Nitride-Based Semiconductor", *IPAP Conf. Series*, vol. 1, pp. 137–140, 2000, Proc. Int. Workshop on Nitride Semiconductors.

[8] K. Nishizuka, M. Funato, Y. Kawakami, S. Fujita, Y. Narukawa, T. Mukai, "Efficient radiative recombination from $\langle 11\bar{2}2\rangle$-oriented $In_xGa_{1-x}N$ multiple quantum wells fabricated by the regrowth technique", *Appl. Phys. Lett.*, vol. 85, pp. 3122–3124, 2004.

[9] S. Khatsevich, D.H. Rich, X. Zhang, W. Zhou, P.D. Dapkus, "Temperature dependence of excitonic recombination in lateral epitaxially overgrown InGaN/GaN quantum wells studied with cathodoluminescence", *J. Appl. Phys.*, vol. 95, pp. 1832–1842, 2004.

[10] T. Wunderer, P. Brückner, B. Neubert, F. Scholz, M. Feneberg, F. Lipski, M. Schirra, K. Thonke, "Bright semipolar GaInN/GaN blue light emitting diode on side facets of selectively grown GaN stripes", *Appl. Phys. Lett.*, vol. 89, pp. 041121–041123, 2006.

[11] A.E. Romanov, T.J. Baker, S. Nakamura, J.S. Speck, "Strain-induced polarization in wurtzite III-nitride semipolar layers", *J. Appl. Phys.*, vol. 100, pp. 023522–023532, 2006.

[12] M. Feneberg, F. Lipski, R. Sauer, K. Thonke, T. Wunderer, B. Neubert, P. Brückner, F. Scholz, "Piezoelectric fields in GaInN/GaN quantum wells on different crystal facets", *Appl. Phys. Lett.*, vol. 89, pp. 242112–242115, 2006.

[13] M. Pophristic, F.H. Long, C. Tran, I.T. Ferguson, R.F. Karlicek, Jr., "Time-resolved photoluminescence measurements of InGaN light-emitting diodes", *Appl. Phys. Lett.*, vol. 73, pp. 3550–3553, 1998.

[14] In our measurement setup, the time between succeeding laser pulses is 13 ns. The decay time is therefore only estimated to be > 50 ns.

[15] F. Scholz, "Metalorganic vapor phase epitaxy of GaN and GaInN/GaN heterostructures and quantum wells", *Prog. Cryst. Growth and Charact.*, vol. 35, pp. 243–262, 1997.

[16] H. Gotoh, T. Tawara, Y. Kobayashi, N. Kobayashi, T. Saitoh, "Piezoelectric effects on photoluminescence properties in 10-nm-thick InGaN quantum wells", *Appl. Phys. Lett.*, vol. 83, pp. 4791–4793, 2003.

MOVPE Growth of High Quality AlN Layers and Effects of Si-doping

Sarad Bahadur Thapa

High quality undoped AlN layers were grown by LP–MOVPE by using optimized growth conditions for nucleation and bulk layers. AFM measurements revealed a rms surface roughness of 0.2 nm with a hexagonal pit density well below 10^5 cm^{-2}. The FWHM of HRXRD for the (002) and (114) reflections are 59 and 390 arcsec, respectively. This excellent quality of our AlN layers is further confirmed by low temperature CL spectra with a FWHM of 10 meV. Furthermore, we have studied the effects of Si incorporation on the structural and spectroscopic properties of AlN layers. We found that the surface quality deteriorates with increasing Si concentrations. Surprisingly, the HRXRD (002) peak is much narrower for our Si doped samples. With increasing Si concentrations up to 10^{19} cm^{-3}, both reflections, (002) and (114), get broader. However, their width decreases again for even higher concentrations, which is accompanied by the development of cracks. Accordingly, HRXRD and low temperature CL measurements show that the in-plane tensile stress of our Si-doped layers increases up to Si concentrations of 10^{19} cm^{-3}, whereas a stress release is observed for higher concentrations.

1. Introduction

Among the group III nitride materials, aluminum nitride (AlN) has attracted much attention due to its large direct bandgap (approx. 6.0 eV) and outstanding thermal and chemical stability. It has a wide application perspective especially in the area of high–power high–temperature electronic devices. Due to the piezoelectric and electromechanical coupling properties, high propagation rate, and low transmission loss, AlN can also be used in various types of acoustic devices [1, 2]. Recently, a report of an LED with a wavelength of 210 nm [3] has demonstrated the strong possibility of a promising application of this material in the field of optoelectronics in the days ahead. Meantime, many groups have been using AlN as a template for the fabrication of UV devices [4, 5]. Furthermore, AlN/GaN superlattice structures can be used in optical devices operating at telecommunication wavelengths by exploiting intersubband transitions between bound quantum well states [6, 7]. However, the growth of high quality AlN, as required for device fabrication, is still a big challenge. Especially the proper doping of AlN layers to obtain electrical conduction as a device performance quality remains to be a key issue for the nitride researchers.

We have previously reported the influence of various growth parameters on the structural and spectroscopic properties of AlN bulk layers [8]. In this report, we present the results of a high quality AlN bulk layer after further optimization of the nucleation layer and subsequent stages. In addition, we investigated the incorporation of Si donors and their influence on the properties of the AlN crystal quality.

2. Experiment

Undoped layers of AlN, approximately 500 nm thick, were grown on c–plane sapphire substrates in an AIXTRON AIX 200 RF LP–MOVPE system by using trimethylaluminum (TMAl) and NH_3 as precursors and H_2 as a carrier gas in N_2 and H_2 atmosphere. To achieve a high quality AlN layer, the growth process was optimized by dividing it into 3 parts, namely, 1. Oxygen doped AlN nucleation layer, 2. Stage between nucleation and AlN bulk layer, and 3. AlN bulk layer.

During the optimization of the nucleation layer, the growth conditions of subsequently deposited AlN bulk layers, as given in Table 3, were kept constant. Oxygen from t–Butanol, used as liquid source in conventional bubbler configuration, was supplied in the form of pulses (2 sec on, 28 sec off) whereas TMAl and NH_3 were turned on throughout the nucleation process [9]. As we need a very small amount of oxygen doping during the nucleation layer growth, the pulsed supply could be an effective method to precisely control the amount. This method offers good controllability as we can vary the pulse width and period in addition to the mass flows. The range of growth parameters of the nucleation layer is given in Table 3. After the growth of the nucleation layer, the reactor temperature was increased to the bulk layer growth temperature under NH_3 atmosphere.

Table 3: Growth conditions of subsequently deposited AlN bulk layer after nucleation layer and range of growth parameters for the nucleation layer optimization.

Growth Parameters	Subsequently grown AlN bulk layer	Range for nucleation layer optimization
Growth Pressure	35 mbar	35 - 100 mbar
Growth Temperature	1150°C	820 - 930°C
V–III Ratio	2000	500 - 18000
N_2–H_2 Ratio	1.3	0.8 - 4.0
Total Flow	2500 sccm	1500 - 5000 sccm

Three different procedures were implemented at the stage between the nucleation and bulk layer growths. Those were: a) Continuous growth of AlN bulk layer after the nucleation layer during the ramping up of temperature, b) Thermal annealing of nucleation layer under NH_3 before bulk layer growth, and c) Cooling the nucleation layer down to 400°C under NH_3 atmosphere and ramping the reactor temperature up to the bulk layer growth temperature followed by a short pre-flow of NH_3 before bulk layer growth. Moreover, the growth temperature of the bulk layer was increased from 1150°C to 1190°C while keeping the other growth parameters constant as given in Table 3.

Si doping was performed by typically depositing a 250 nm thick Si-doped AlN layer on a 250 nm thick optimized undoped AlN buffer layer at the growth temperature of 1150°C. Si was incorporated by using silane (SiH_4) as a Si source through a double dilution configuration of massflow controllers. The basic growth conditions of the Si–doped layers were

similar to those of the undoped buffer layers. The Si concentration was extrapolated from our growth parameters using other AlN samples as reference which had been measured by secondary ion mass spectroscopy (SIMS) [10].

The surface quality was analyzed by using atomic force microscopy (AFM). High–resolution X–ray diffraction (HRXRD) rocking curve measurements for the symmetric and asymmetric reflections were carried out to examine the crystal quality of bulk AlN epitaxial layers. Low temperature (T=10 K) cathodoluminescence (CL) provided information about the spectroscopic properties.

3. Results and Discussions

3.1 Undoped AlN layer

Continuing our previous studies described in [11], we have determined the optimized growth parameters for a nucleation layer as given in Table 4.

Table 4: Optimized growth parameters for the nucleation layer.

Growth Parameters	Optimized value
Growth Pressure	70 mbar
Growth Temperature	870°C
V–III Ratio	2500
N_2–H_2 Ratio	1.9
Total Flow	2000 sccm

We observed that the amount of oxygen supplied in the nucleation layer is one of the critical parameters for the surface and crystal quality of AlN. Both the rms surface roughness and FWHM of HRXRD for the (002) reflection of the AlN bulk layers could be minimized when the supply of oxygen was 5 pulses in comparison to the nucleation layer without and with the supply of larger number of oxygen pulses (Fig. 1(left)). The AlN quality is further improved by 2 min extended growth of the AlN nucleation layer without oxygen doping as demonstrated in Fig. 1(right). However, longer times produced a negative effect on both the surface and crystal quality. With these results, we confirmed that oxygen doping is needed just at the beginning of the nucleation layer growth. The total thickness of the nucleation layer should be approximately 30 nm to obtain a high quality AlN layer where only the first part is doped with oxygen.

In a next step, we studied the influence of various processes carried out at the stage between nucleation and bulk layer growth on the quality of AlN. The continuous growth of AlN after the nucleation layer during the ramping up of temperature decreased both, the surface and crystal quality. Though the thermal annealing of the nucleation layer under NH_3 before the growth of the bulk layer improved the crystal quality, it had very bad effect on the surface quality due to the strong decomposition of the nucleation layer.

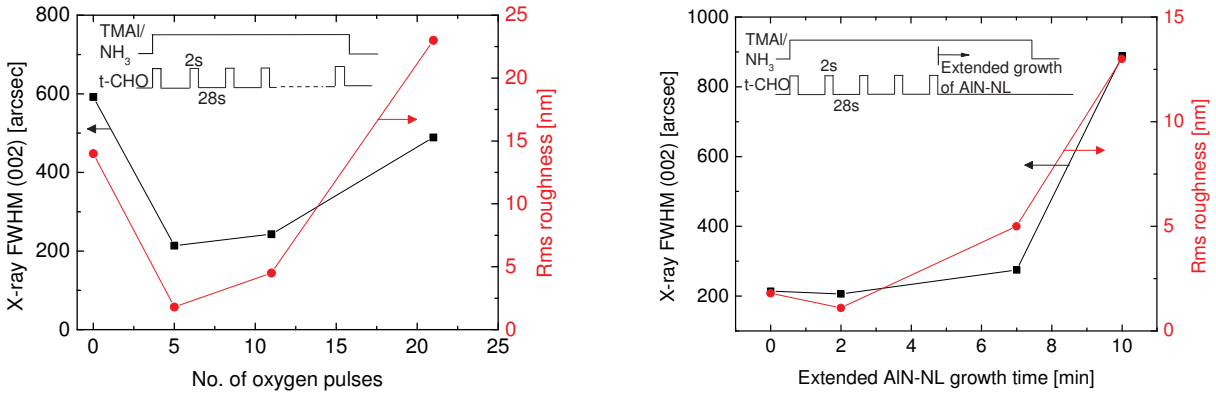

Fig. 1: FWHM of HRXRD for the (002) reflection and rms surface roughness of AlN bulk layers: Plots for different numbers of oxygen pulses supplied during the nucleation layer growth (left), extended growth of the AlN nucleation layer after the supply of 5 pulses of oxygen at the beginning of the nucleation process (right).

However, among the three procedures described in section 2, cooling down of the nucleation layer till 400°C under NH_3 atmosphere and ramping the reactor temperature to the bulk layer growth temperature followed by a short pre–flow of NH_3 enhanced both the surface and crystal quality of AlN further. Cooling down of the nucleation layer might relax the stress induced by thermal mismatch. Hence, further effect of thermal strain on subsequently grown AlN bulk layer was minimized with this procedure. The short pre–flow of NH_3 before the growth of the bulk layer may assist the re–crystallization and further coalescence of AlN islands of the nucleation layer at high temperature which in effect transforms the 3D growth mode of the nucleation layer to 2D growth of the bulk layer.

After the optimization of these initial parts of our growth procedure, we obtained high quality AlN as given in Table 5(a). Further rise of the bulk layer growth temperature from 1150°C to 1190°C finally resulted in a very high quality of AlN (Table 5(b)). The hexagonal pit density on the surface was significantly reduced to less than $10^5\,\mathrm{cm}^{-2}$. Figure 2 shows an AFM image of an atomically flat layer with a measured rms value of the surface roughness of 0.2 nm. The FWHM of the X-ray rocking curve for the (002) and (114) reflections are 59 and 390 arcsec, respectively. These excellent data were further confirmed by a band edge excitonic emission with a FWHM of 10 meV (Fig. 3). The LO phonon replica confirm the good optical quality of the bulk AlN epitaxial layers.

3.2 Si-doped AlN layer

In order to influence the electrical properties of our AlN layers, we investigated Si doping. Similar as reported by Ive et al.[12], we found that it has an adverse effect on the surface quality of AlN. As shown in Fig. 4, we observed the formation of a large number of pits on the surface attributed to the effect of Si doping. Moreover, the Si incorporation has shown a remarkable impact on the crystal quality of AlN [13]. Surprisingly, the HRXRD (002) peak is much narrower for our Si doped samples as compared to their undoped counterparts whereas the (114) peak is slightly broader. For both, (002) and

Table 5: Result of the optimized AlN bulk layers.

Parameters	Growth at 1150°C (a)	Growth at 1190°C (b)
Rms surface roughness	0.4 nm	0.2 nm
Hexagonal pit density	$\approx 10^7\,\mathrm{cm}^{-2}$	$< 10^5\,\mathrm{cm}^{-2}$
FWHM of HRXRD (002) reflection	200 arcsec	59 arcsec
FWHM of HRXRD (114) reflection	600 arcsec	390 arcsec
FWHM of low temp. CL peak	$\approx$ 20 meV	$\approx$ 10 meV

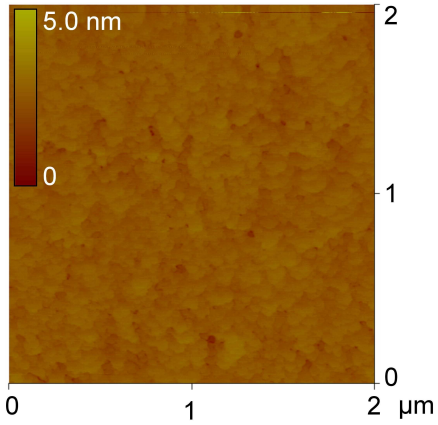

Fig. 2: AFM image of the optimized AlN bulk layer grown at 1190°C.

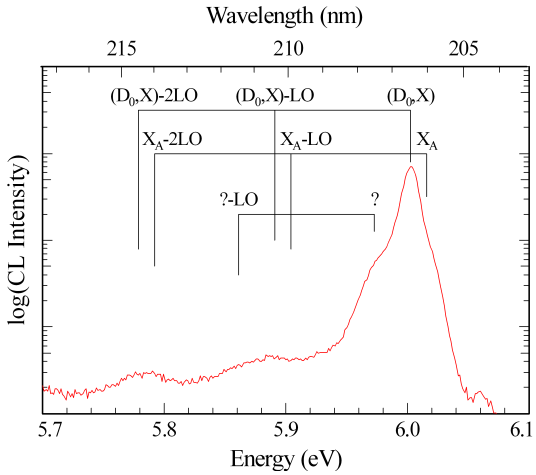

Fig. 3: Low temperature CL spectrum of optimized AlN bulk layer. The FWHM of the CL peak is approx. 10 meV.

(114) reflections, the FWHM increased with increasing Si concentration up to a level of $10^{19}\,\mathrm{cm}^{-3}$ and decreased for higher concentrations (Fig. 5).

Similarly, we found increasing in-plane tensile strain on the AlN:Si layers with increasing Si concentrations up to $10^{19}\,\mathrm{cm}^{-3}$, whereas it decreased for higher concentrations (Fig. 6). A lot of cracks was clearly visible on the surface of such samples under optical microscopy investigations, whereas the samples with Si concentration less than $10^{19}\,\mathrm{cm}^{-3}$ were almost crack free. This behaviour was verified by low temperature CL measurements. Figure 7 demonstrates the red shift of the CL peaks with respect to increasing Si concentrations indicating larger tensile strain, while it was blue shifted for the samples having Si concentration higher than $10^{19}\,\mathrm{cm}^{-3}$. Such an effect of Si incorporation with different concentrations on structural and spectroscopic properties of AlN layers was further evidenced by Raman scattering measurements [14]. Unfortunately, we could not get indications for n–type conductivity in our Si doped AlN layers.

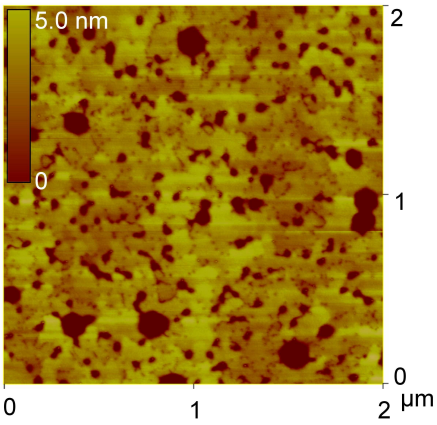

Fig. 4: AFM image of a Si–doped ($9 \cdot 10^{18}\,\mathrm{cm}^{-3}$) AlN layer. A large number of pits are visible.

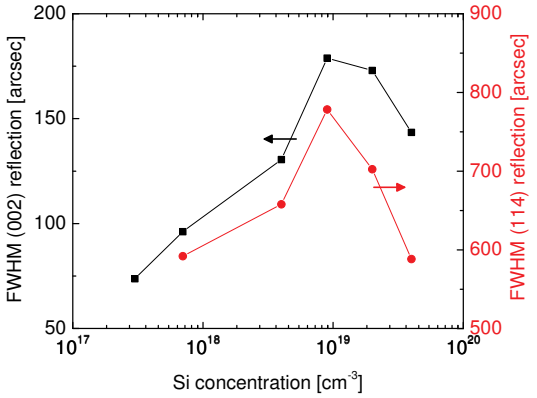

Fig. 5: FWHM of HRXRD for (002) and (114) reflections for different Si concentrations.

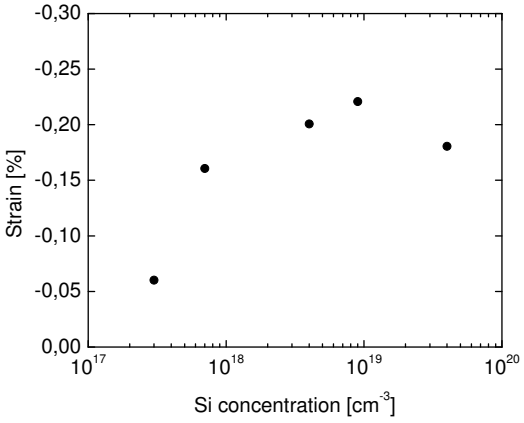

Fig. 6: Strain of Si–doped AlN layers at various Si concentrations determined from the HRXRD rocking curve measurements.

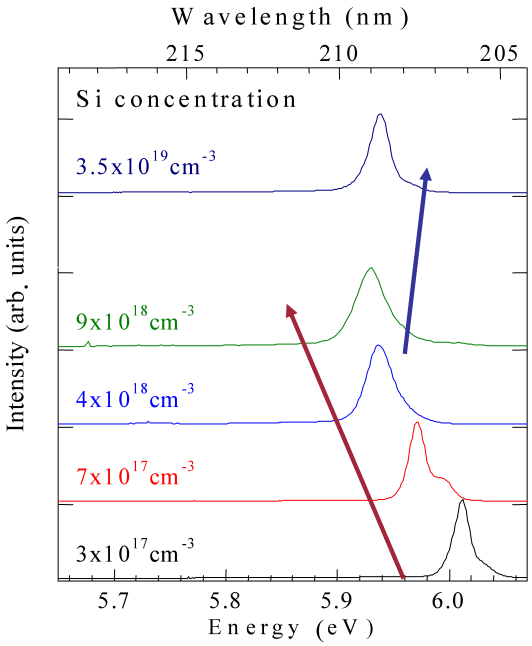

Fig. 7: Red shifting of CL peak of AlN layers till the Si concentration of $10^{19}\,\mathrm{cm}^{-3}$ and blue shifting for higher concentration.

4. Summary

We obtained very high quality AlN layers having rms surface roughness of 0.2 nm, FWHM of HRXRD for (002) and (114) reflections of 59 and 390 arcsec, respectively after optimization of nucleation layer, stage between nucleation and bulk layer, and bulk layer growth where we obtained the best results for a growth temperature of 1190°C. The hexagonal pit density on the surface is determined to be well below $10^5\,\mathrm{cm}^{-2}$. This excellent quality of our AlN layers is further confirmed by low temperature CL spectra with a FWHM

of the donor bound exciton peak of 10 meV. We investigated the effects of Si incorporation on the structural and spectroscopic properties of the AlN layer. It was observed that the surface quality is degraded after Si incorporation. The slight broadening of the (114) reflection of HRXRD measurements can be correlated with the presence of a large number of pits on the surface of Si–doped AlN layers. However, the decrease in FWHM of HRXRD for (002) reflection demonstrates the positive impact of Si on crystal quality. The FWHM of both HRXRD reflections, (002) and (114), increased with increasing Si concentrations up to $10^{19}\,\mathrm{cm}^{-3}$ and decreased for higher concentrations. Furthermore, HRXRD and low temperature CL measurements show increasing in-plane tensile stress up to Si concentrations of $10^{19}\,\mathrm{cm}^{-3}$ and release of such stress by crack formation for higher concentrations.

Acknowledgment

I would like to thank G.M. Prinz, and K. Thonke of the Institute of Semiconductor Physics for CL and Raman measurements; L. Kirste, T. Fuchs, and M. Grimm of Fraunhofer–Institut für Angewandte Festkörperphysik for SIMS measurements. S. Wabra and Hu Wenjie for AFM measurements; J. Hertkorn and P. Brückner for fruitful discussions on epitaxy and system maintenances. This work was financially supported by the Deutsche Forschungsgemeinschaft.

References

[1] C.M. Yang, K. Uehara, S.K. Kim, S. Kameda, H. Nakase, and K. Tsubouchi, "Highly c-axis-oriented AlN film using MOCVD for 5GHz-band FBAR filter", *IEEE Symposium on Ultrasonics*, vol. 1, pp. 170–173, 2003.

[2] R. Lanz, and P. Muralt, "Solidly mounted BAW filters for 8 GHz based on AlN thin films", *IEEE Symposium on Ultrasonics*, vol. 1, pp. 178–181, 2003.

[3] Y. Taniyasu, M. Kasu, and T. Makimoto, "An aluminium nitride light-emitting diode with a wavelength of 210 nanometers", *Nature (London)*, vol. 441, no. 18, pp. 325–328, 2006.

[4] T.M. Katona, T. Margalith, C. Moe, M.C. Schmidt, C. Matt, S. Nakamura, J.S. Speck, S.P. DenBaars, and P. Steven, "Growth and fabrication of short-wavelength UV LEDs", in *Third International Conference on Solid State Lighting*, I.T. Ferguson, N. Narendran, S.P. DenBaars, J.C. Carano (Eds.), Proc. SPIE 5187, pp. 250–259, 2004.

[5] M. Shatalov, Z. Gong, M. Gaevski, S. Wu, W. Sun, V. Adivarahan, and M.A. Khan, "Reliability of AlGaN-based deep UV LEDs on sapphire", *Light-Emitting Diodes: Research, Manufacturing, and Applications*, K.P. Streubel, H.W. Yao, E.F. Schubert (Eds.), Proc. SPIE 6134, pp. 61340P, 2006.

[6] D. Hofstetter, S. Schad, H. Wu, W.J. Schaff, and L.F. Eastman, "GaN/AlN-based quantum-well infrared photodetector for 1.55 m", *Appl. Phys. Lett.*, vol. 83, pp. 572–575, 2003.

[7] I. Waki, C. Kumtornkittikul, Y. Shimogaki, and Y. Nakano, "Shortest intersubband transition wavelength (1.68 µm) achieved in AlN/GaN multiple quantum wells by metalorganic vapor phase epitaxy", *Appl. Phys. Lett.*, vol. 82, pp. 4465–4467, 2002.

[8] S.B. Thapa, C. Kirchner, F. Scholz, G.M. Prinz, K. Thonke, R. Sauer, A. Chuvilin, J. Biskupek, U. Kaiser, and D. Hofstetter, "Structural and spectroscopic properties of AlN layers grown by MOVPE", *J. Crystal Growth*, vol. 298, pp. 383–386, 2007.

[9] B. Kuhn and F. Scholz, "An Oxygen Doped Nucleation Layer for the Growth of High Optical Quality GaN on Sapphire", *physica status solidi (a)*, vol. 188, no. 2, pp. 629–633, 2001.

[10] L. Kirste, T. Fuchs, and M. Grimm; Fraunhofer–Institut für Angewandte Festkörperphysik, Freiburg, Samples Y987,Y989,Y990.

[11] S.B. Thapa, *Annual Report 2005*, Optoelectronics Department, Ulm University.

[12] T. Ive, O. Brandt, H. Kostial, K.J. Friedland, L. Däweritz, and K.H. Ploog "Controlled n-type doping of AlN:Si films grown on 6H-SiC(0001) by plasma-assisted molecular beam epitaxy", *Appl. Phys. Lett.*, vol. 86, pp. 024106, 2005.

[13] V. Lebedev, F.M. Morales, H. Romanus, S. Krischok, G. Ecke, V. Cimalla, M. Himmerlick, T. Stauden, D. Cengher, and O. Ambacher "The role of Si surfactant and donor in molecular-beam epitaxy of AlN", *J. Appl. Phy.*, vol. 98, pp. 093508, 2005.

[14] G.M. Prinz, M. Feneberg, M. Schirra, K. Thonke, R. Sauer, S.B. Thapa, F. Scholz, M. Bickermann, and B. Epelbaum "Optical Spectroscopy of doped and undoped Aluminium Nitride Layers on Sapphire Substrates ", *DGKK-Workshop III-V-Epitaxie*, Ulm, Germany, Dec. 2006

Ph.D. Theses

1. Martin Peschke,
   Laser Diodes Integrated with Electroabsorption Modulators for 40 Gb/s Data Transmission,
   March 2006.

2. Brem Kumar Saravanan,
   Frequency Chirping Properties of Electroabsorption Modulators Integrated with Laser Diodes,
   April 2006.

3. Frank Habel,
   Methoden zur Defektreduktion von Galliumnitrid-Substraten und -Quasisubstraten,
   July 2006.

4. Steffen Lorch,
   Herstellung, Charakterisierung und Anwendungen von ionenstrahlgesputterten optischen Schichten,
   July 2006.

Diploma and Master Theses

1. Thomas Wunderer,
   Elektrolumineszenz-Untersuchungen an GaInN-Facetten-Quantenfilmen,
   Diploma Thesis, March 2006.

2. Kerstin Spöttle,
   Thermisches Management von High-Power-LEDs und dessen Einfluss auf die Bauteil-Lebensdauer,
   Diploma Thesis, October 2006.

3. Faisal Imam,
   Novel High-Speed Test Platform for Flip-Chip Bonded 2-D 850-nm VCSEL Arrays,
   Master Thesis, November 2006.

4. Alexander Weigl,
   Innovative flip-chip integrierbare Vertikallaserarrays,
   Diploma Thesis, November 2006.

Semester Projects

1. Reinhard Nopper,
   Untersuchungen zu Dunkelströmen
   in Metall–Halbleiter–Metall (MSM)-Photodioden,
   May 2006.

2. Alexander Kern,
   Untersuchungen zur Strahlqualität
   eines optisch gepumpten Halbleiter-Scheibenlasers,
   October 2006.

3. Carolin Schneck,
   Statische und dynamische Charakterisierung
   von Metall–Halbleiter–Metall (MSM)-Photodioden
   im Rahmen der Optimierung einer Transceiver-Schichtstruktur,
   September 2006.

Talks and Conference Contributions

[1] P. Brückner and F. Scholz, "Self-separation of GaN using in-situ deposited SiN as separation layer", *Int. Workshop on Nitride Semiconductors*, Kyoto, Japan, Oct. 2006.

[2] P. Brückner and F. Scholz, "Erzeugung von freistehenden GaN-Substraten mit Hilfe von SiN-Zwischenschichten", *DGKK-Workshop III-V-Epitaxie*, Ulm, Germany, Dec. 2006.

[3] A. Gadallah, M. Stach, F. Rinaldi, S. Lorch, I. Kardosh, P. Gerlach, and R. Michalzik, "Fabrication and characterization of GaAs-based transceiver chips for bidirectional optical data transmission", *XXVI Conf. on Solid State Physics and Materials Science* of the Egyptian Materials Research Society, *Eg-MRS 2006* & Workshop on *Nanostructures: Science, Fabrication, Characterization and Devices*, Alexandria, Egypt, Sept. 2006.

[4] P. Gerlach, M. Peschke, T. Wenger, B.K. Saravanan, C. Hanke, S. Lorch, and R. Michalzik, "Complex coupled distributed feedback laser monolithically integrated with electroabsorption modulator and semiconductor optical amplifier at 1.3 µm wavelength", *SPIE Photonics Europe*, Conf. on *Integrated Optics, Silicon Photonics, and Photonic Integrated Circuits,* Strasbourg, France, Apr. 2006.

[5] P. Gerlach and R. Michalzik, "A simple half-duplex optical link using identical Fabry–Perot lasers at 1.5 µm wavelength", Poster at Workshop *Electrical and Electronic Engineering for Communication, EEEfCOM 2006*. Ulm, Germany, June 2006.

[6] J. Hertkorn, P. Brückner, T. Wunderer, S.B. Thapa, and F. Scholz, "AlN-Nukleation auf Saphir-Substraten für das Wachstum von hochqualitativen GaN-Schichten", *DGKK-Workshop III-V-Epitaxie*, Ulm, Germany, Dec. 2006.

[7] A. Kroner, J.F. May, I. Kardosh, F. Rinaldi, H. Roscher, and R. Michalzik, "Novel concepts of vertical-cavity laser-based optical traps for biomedical applications", *SPIE Photonics Europe*, Conf. on *Biophotonics and New Therapy Frontiers*, Strasbourg, France, Apr. 2006.

[8] A. Kroner, A. Gadallah, I. Kardosh, F. Rinaldi, and R. Michalzik, "Integrated VCSEL trap arrays for microfluidic particle separation and sorting", *EOS Topical Meeting on Biophotonics and Biomedical Optics*, Paris, France, Oct. 2006.

[9] R. Michalzik, "Ultra-compact optical traps based on vertical-cavity laser diodes", National Physical Laboratory (NPL), New Delhi, India, Dec. 2006.

[10] R. Michalzik, "Vertical-cavity laser diode research at Ulm University", Indian Institute of Technology Delhi, Physics Dept., New Delhi, India, Dec. 2006.

[11] R. Michalzik, "High-performance vertical-cavity laser diodes enabling new applications" (invited), *Eighth International Conf. on Optoelectronics, Fiber Optics and Photonics, Photonics 2006*, Hyderabad, India, Dec. 2006.

[12] R. Michalzik and A. Kroner, "Ultra-compact optical traps" (in German: "Ultrakompakte optische Fallen"), Working Group *Medicine and Biotechnology* within the Photonics BW Association, Roche Diagnostics GmbH, Mannheim, Germany, March 2006.

[13] R. Michalzik, "Vertical-cavity laser diodes: current research topics and applications" (in German: "Vertikallaserdioden: aktuelle Forschungsgebiete und Anwendungen"), Graduiertenkolleg 384 of the German Research Foundation (DFG): *Nanoelectronics, Micromechanics and Microoptics: Analysis and Synthesis by Ions, Electrons and Photons*, Ruhr-Universität Bochum, Bochum, Germany, Febr. 2006.

[14] R. Michalzik, "Novel short-wavelength vertical-cavity laser diode designs and applications", *Physics Seminar* of the University of Neuchâtel, Neuchâtel, Switzerland, Jan. 2006.

[15] B. Neubert, T. Wunderer, P. Brückner, F. Scholz, M. Feneberg, F. Lipski, M. Schirra, and K. Thonke, "Semipolar GaN/GaInN LEDs with more than 1 mW optical output power", *Int. Conf. on MOVPE*, Miyazaki, Japan, May 2006.

[16] B. Neubert, "Research on GaN at Optoelectronics Department", *Meijo University*, Nagoya, Japan, June 2006.

[17] J.M. Ostermann, P. Debernardi, and R. Michalzik, "Optimization of polarization-stable single- and multi-mode surface grating VCSELs towards high fabrication tolerance and superior performance", *SPIE Photonics Europe*, Conf. on *Semiconductor Lasers and Laser Dynamics II*, Strasbourg, France, Apr. 2006.

[18] M.C. Riedl, F. Rinaldi, S. Menzel, F. Demaria, S. Lorch, I. Kardosh, R. Rösch, R. Michalzik, and P. Unger, "Spannungskompensation für Halbleiter-Scheibenlaser und VCSEL", *DGKK-Workshop III-V-Epitaxie*, Ulm, Germany, Dec. 2006.

[19] F. Rinaldi, J.M. Ostermann, A. Kroner, M.C. Riedl, and R. Michalzik, "760 nm high-performance VCSEL growth and characterization", *SPIE Photonics Europe*, Conf. on *Micro-Optics, VCSELs and Photonic Interconnects: Fabrication, Packaging, and Integration*, Strasbourg, France, Apr. 2006.

[20] F. Rinaldi, F. Demaria, S. Lorch, S. Menzel, M.C. Riedl, R. Rösch, P. Unger, S.-S. Beyertt, U. Brauch, N. Dhidah, A. Giesen, and T. Kübler, "MBE growth and characterization of quantum well pumped disk lasers", *DGKK-Workshop III-V-Epitaxie*, Ulm, Germany, Dec. 2006.

[21] H. Roscher, P. Gerlach, F.N. Khan, A. Kroner, M. Stach, A. Weigl, and R. Michalzik, "Toward more efficient fabrication of high-density 2-D VCSEL arrays for spatial redundancy and/or multi-level signal communication", *SPIE Photonics Europe*, Conf. on *Micro-Optics, VCSELs and Photonic Interconnects: Fabrication, Packaging, and Integration*, Strasbourg, France, Apr. 2006.

[22] W. Schwarz, I. Kardosh, F. Rinaldi, and R. Michalzik, "Cavity optimization of electrically pumped VECSELs", *Semiconductor and Integrated Optoelectronics Conf., SIOE 2006*, Cardiff, Wales, UK, April 2006.

[23] F. Scholz, "GaN für die Optoelektronik: Herausforderungen und Chancen zur Effizienz-Steigerung von Lichtemittern", *TU Karlsruhe*, Karlsruhe, Germany, Febr. 2006.

[24] F. Scholz, "Selektive Epitaxie von GaN: Bessere Wafer, hellere LEDs?", *TU Ilmenau*, Ilmenau, Germany, Febr. 2006.

[25] F. Scholz, "Piezoreduzierte Quantenfilme auf selektiv gewachsenen GaN-Streifen: Chancen für grüne Laser?", *DFG-Rundgespräch*, Regensburg, March 2006.

[26] F. Scholz, "Nitride activities at Optoelectronics Dept.", *NTT Basic Research Lab*, Atsugi, Japan, May 2006.

[27] F. Scholz, "Nitride activities at Optoelectronics Dept.", *Tokyo University of Agriculture and Technology*, Tokyo, Japan, May 2006.

[28] M. Stach, M. Chandran, F. Rinaldi, S. Lorch, I. Kardosh, H. Roscher, P. Gerlach, and R. Michalzik, "Monolithically integrated transceiver chips for bidirectional optical interconnection", *SPIE Photonics Europe*, Conf. on *Micro-Optics, VCSELs, and Photonic Interconnects II: Fabrication, Packaging, and Integration*, Strasbourg, France, Apr. 2006.

[29] M. Stach, F. Rinaldi, M. Chandran, S. Lorch, and R. Michalzik, "Bidirectional optical data transmission over multimode fiber with monolithically integrated transceiver chips", *7th International Conf. on Optical Technologies, Optical Sensors & Measuring Techniques, OPTO 2006*, Nürnberg, Germany, May/June 2006.

[30] M. Stach, F. Rinaldi, A. Gadallah, S. Lorch, I. Kardosh, P. Gerlach, and R. Michalzik, "Monolithically integrated transceiver chips for Gbit/s half- and full-duplex optical data transmission over graded-index multimode fiber", *European Semiconductor Laser Workshop*, Nice, France, Sept. 2006.

[31] M. Stach, F. Rinaldi, A. Gadallah, S. Lorch, I. Kardosh, P. Gerlach, and R. Michalzik, "1 Gbit/s bidirectional data transmission over 100 m graded-index glass optical fiber with monolithically integrated transceiver chips", *Europ. Conf. on Opt. Commun., ECOC 2006*, Cannes, France, Sept. 2006.

[32] M. Stach, F. Rinaldi, S. Lorch, and R. Michalzik, "Novel optoelectronic components for bidirectional optical Gbit/s computer networks" (in German: "Neuartige optoelektronische Komponenten für bidirektionale optische Gbit/s-Computernetzwerke"), *9th Workshop on Optics in Computing Technology, ORT 2006*, Siegen, Germany, Oct. 2006.

[33] M. Stach, F. Rinaldi, S. Lorch, and R. Michalzik, "Gbit/s-range bidirectional optical data transmission at 850 nm wavelength for automotive and in-house networks based on novel transceiver chips and PCS or graded-index glass fibers" (in German: "Bidirektionale optische Datenübertragung im Gbit/s-Bereich bei 850 nm Wellenlänge für Automotive- und Inhaus-Netze basierend auf neuartigen Transceiver-Bauelementen sowie PCS-Fasern oder Gradientenindex-Glasfasern"), *13th ITG Symposium on Communication Cable Networks*, Köln, Germany, Dec. 2006.

[34] S.B. Thapa, C. Kirchner, F. Scholz, G.M. Prinz, K. Thonke, R. Sauer, A. Chuvilin, J. Biskupek, U. Kaiser, and D. Hofstetter, "Structural and spectroscopic properties of AlN grown by MOVPE", Poster at *Int. Conf. on MOVPE*, Miyazaki, Japan, May 2006.

[35] S.B. Thapa, C. Kirchner, F. Scholz, G.M. Prinz, K. Thonke, R. Sauer, A. Chuvilin, J. Biskupek, U. Kaiser, and D. Hofstetter, "Structural and spectroscopic properties of AlN grown by MOVPE", *NTT Basic Research Lab*, Atsugi, Japan, May 2006.

[36] S.B. Thapa, C. Kirchner, F. Scholz, G.M. Prinz, K. Thonke, R. Sauer, A. Chuvilin, J. Biskupek, U. Kaiser, and D. Hofstetter, "Structural and spectroscopic properties of AlN grown by MOVPE", *Tokyo University of Agriculture and Technology*, Tokyo, Japan, May 2006.

[37] S.B. Thapa, C. Kirchner, F. Scholz, G.M. Prinz, K. Thonke, R. Sauer, A. Chuvilin, J. Biskupek, U. Kaiser, and D. Hofstetter, "Structural and spectroscopic properties of AlN grown by MOVPE", *Meijo University*, Nagoya, Japan, June 2006.

[38] S.B. Thapa, J. Hertkorn, F. Scholz, G.M. Prinz, and K. Thonke, "Effect of initial growth process and Si incorporation on structural and spectroscopic properties of AlN grown by MOVPE", *DGKK-Workshop III-V-Epitaxie*, Ulm, Germany, Dec. 2006.

[39] P. Unger, "Physikalische Grundlagen und Eigenschaften anorganischer Halbleiterlichtquellen", *OTTI-Fachforum Halbleiterlichtquellen*, Regensburg, Germany, Dec. 2006.

[40] P. Unger, "Optically Pumped Semiconductor Disk Lasers", *Photonic Seminar Series*, Tyndall National Institute, Cork, Ireland, Dec. 2006.

[41] T. Wunderer, P. Brückner, J. Hertkorn, F. Scholz, G. Beirne, M. Jetter, P. Michler, M. Feneberg, K. Thonke, "Zeitaufgelöste PL an semipolaren GaInN/GaN-Leuchtdioden", *DGKK-Workshop III-V-Epitaxie*, Ulm, Germany, Dec. 2006.

Publications

[1] P. Brückner, M. Feneberg, K. Thonke, F. Habel, and F. Scholz, "High quality GaN layers grown on slightly miscut sapphire wafers", *Mat. Res. Symp. Proc.*, vol. 892, pp. 0892-FF21-04.1–6, 2006.

[2] P. Brückner, F. Habel, and F. Scholz, "HVPE growth of high quality GaN layers", *phys. stat. sol. (c)*, vol. 3, no. 6, pp. 1471–1474, 2006.

[3] A. Gadallah, M. Stach, F. Rinaldi, S. Lorch, I. Kardosh, P. Gerlach, and R. Michalzik, "Fabrication and characterization of GaAs-based transceiver chips for bidirectional optical data transmission", in Proc. *XXVI Conf. on Solid State Physics and Materials Science* of the Egyptian Materials Research Society, *Eg-MRS 2006* & Workshop on *Nanostructures: Science, Fabrication, Characterization and Devices*, p. 128. Alexandria, Egypt, Sept. 2006.

[4] P. Gerlach, M. Peschke, T. Wenger, B.K. Saravanan, C. Hanke, S. Lorch, and R. Michalzik, "Complex-coupled distributed feedback laser monolithically integrated with electroabsorption modulator and semiconductor optical amplifier at 1.3 μm wavelength", in *Integrated Optics, Silicon Photonics, and Photonic Integrated Circuits*, G.C. Righini (Ed.), Proc. SPIE 6183, pp. 61831J-1–9, 2006.

[5] P. Gerlach and R. Michalzik, "A simple half-duplex optical link using identical Fabry–Perot lasers at 1.5 µm wavelength", in Proc. (CD ROM) Workshop *Electrical and Electronic Engineering for Communication, EEEfCOM 2006*, poster 1. Ulm, Germany, June 2006.

[6] A. Kroner, I. Kardosh, F. Rinaldi, and R. Michalzik, "Towards VCSEL-based integrated optical traps for biomedical applications", *Electron. Lett.*, vol. 42, no. 2, pp. 93–94, 2006.

[7] A. Kroner, J.F. May, I. Kardosh, F. Rinaldi, H. Roscher, and R. Michalzik, "Novel concepts of vertical-cavity laser-based optical traps for biomedical applications", in *Biophotonics and New Therapy Frontiers*, R. Grzymala, O. Haeberlé (Eds.), Proc. SPIE 6191, pp. 619112-1–12, 2006.

[8] A. Kroner, A. Gadallah, I. Kardosh, F. Rinaldi, and R. Michalzik, "Integrated VCSEL trap arrays for microfluidic particle separation and sorting", in Proc. *EOS Topical Meeting on Biophotonics and Biomedical Optics*, pp. 140–141. Paris, France, Oct. 2006.

[9] R. Michalzik, A. Kroner, J.M. Ostermann, M. Riedl, F. Rinaldi, H. Roscher, and M. Stach, "High-performance vertical-cavity laser diodes enabling new applications" (invited), in Proc. *Eighth International Conf. on Optoelectronics, Fiber Optics and Photonics, Photonics 2006*, vol. 2, p. 246. Hyderabad, India, Dec. 2006.

[10] B. Neubert, F. Habel, P. Brückner, F. Scholz, M. Schirra, M. Feneberg, K. Thonke, T. Riemann, J. Christen, M. Beer, J. Zweck, G. Moutchnik, and M. Jetter, "Investigations on local Ga and In incorporation of GaInN quantum wells on facets of selectively grown GaN stripes", *phys. stat. sol. (c)*, vol. 3, no. 6, pp. 1587–1590, 2006.

[11] J.M. Ostermann, P. Debernardi, and R. Michalzik, "Optimized integrated surface grating design for polarization-stable VCSELs", *IEEE J. Quantum Electron.*, vol. 42, no. 7, pp. 690–698, 2006.

[12] J.M. Ostermann, P. Debernardi, and R. Michalzik, "Optimization of polarization-stable single- and multi-mode surface grating VCSELs towards high fabrication tolerance and superior performance", in *Semiconductor Lasers and Laser Dynamics II*, D. Lenstra, M. Pessa, I.H. White (Eds.), Proc. SPIE 6184, pp. 618410-1–12, 2006.

[13] F. Rinaldi, J.M. Ostermann, A. Kroner, M.C. Riedl, and R. Michalzik, "760 nm high-performance VCSEL growth and characterization", in *Micro-Optics, VCSELs, and Photonic Interconnects II: Fabrication, Packaging, and Integration*, H. Thienpont, M.R. Taghizadeh, P. Van Daele, J. Mohr (Eds.), Proc. SPIE 6185, pp. 61850X-1–7, 2006.

[14] H. Roscher, P. Gerlach, F.N. Khan, A. Kroner, M. Stach, A. Weigl, and R. Michalzik, "Toward more efficient fabrication of high-density 2-D VCSEL arrays for spatial redundancy and/or multi-level signal communication", in *Micro-Optics, VCSELs, and Photonic Interconnects II: Fabrication, Packaging, and Integration*, H. Thienpont, M.R. Taghizadeh, P. Van Daele, J. Mohr (Eds.), Proc. SPIE 6185, pp. 61850V-1–12, 2006.

[15] W. Schwarz, I. Kardosh, F. Rinaldi, and R. Michalzik, "Cavity optimization of electrically pumped VECSELs", in Proc. *Semiconductor and Integrated Optoelectronics Conf., SIOE 2006*, paper 40. Cardiff, Wales, UK, April 2006.

[16] M. Stach, F. Rinaldi, M. Chandran, S. Lorch, and R. Michalzik, "Monolithically integrated GaAs-based transceiver chips for bidirectional optical data transmission", *Electron. Lett.*, vol. 42, no. 12, pp. 716–718, 2006.

[17] M. Stach, F. Rinaldi, M. Chandran, S. Lorch, and R. Michalzik, "Bidirectional optical interconnection at Gb/s data rates with monolithically integrated VCSEL–MSM transceiver chips," *IEEE Photon. Technol. Lett.*, vol. 18, pp. 2386–2388, 2006.

[18] M. Stach, M. Chandran, F. Rinaldi, S. Lorch, I. Kardosh, H. Roscher, P. Gerlach, and R. Michalzik, "Monolithically integrated transceiver chips for bidirectional optical interconnection", in *Micro-Optics, VCSELs, and Photonic Interconnects II: Fabrication, Packaging, and Integration*, H. Thienpont, M.R. Taghizadeh, P. Van Daele, J. Mohr (Eds.), Proc. SPIE 6185, pp. 61850Q-1–6, 2006.

[19] M. Stach, F. Rinaldi, M. Chandran, S. Lorch, and R. Michalzik, "Bidirectional optical data transmission over multimode fiber with monolithically integrated transceiver chips", in Proc. *7th International Conf. on Optical Technologies, Optical Sensors*

& Measuring Techniques, OPTO 2006, pp. 99–102. Nürnberg, Germany, May/June 2006.

[20] M. Stach, F. Rinaldi, A. Gadallah, S. Lorch, I. Kardosh, P. Gerlach, and R. Michalzik, "1 Gbit/s bidirectional data transmission over 100 m graded-index glass optical fiber with monolithically integrated transceiver chips", in Proc. *32nd Europ. Conf. on Opt. Commun., ECOC 2006*, vol. 3, pp. 493–494. Cannes, France, Sept. 2006.

[21] M. Stach, F. Rinaldi, S. Lorch, and R. Michalzik, "Novel optoelectronic components for bidirectional optical Gbit/s computer networks" (in German: "Neuartige optoelektronische Komponenten für bidirektionale optische Gbit/s-Computernetzwerke"), in Proc. *9th Workshop on Optics in Computing Technology, ORT 2006*, pp. 13–19. Siegen, Germany, Oct. 2006.

[22] M. Stach, F. Rinaldi, S. Lorch, and R. Michalzik, "Gbit/s-range bidirectional optical data transmission at 850 nm wavelength for automotive and in-house networks based on novel transceiver chips and PCS or graded-index glass fibers" (in German: "Bidirektionale optische Datenübertragung im Gbit/s-Bereich bei 850 nm Wellenlänge für Automotive- und Inhaus-Netze basierend auf neuartigen Transceiver-Bauelementen sowie PCS-Fasern oder Gradientenindex-Glasfasern"), *13th ITG Symposium on Communication Cable Networks*, Köln, Germany, Dec. 2006. In *ITG-Fachbericht Kommunikationskabelnetze*, vol. 197, pp. 163–166, 2006.

[23] T. Wunderer, P. Brückner, B. Neubert, F. Scholz, M. Feneberg, F. Lipski, M. Schirra, and K. Thonke, "Bright semipolar GaInN/GaN blue light emitting diode on side facets of selectively grown GaN stripes", *Appl. Phys. Lett.*, vol. 89, pp. 041121-1–3, 2006.

[24] M. Arizaleta Arteaga, H.J. Unold, J.M. Ostermann, R. Michalzik, M. López-Amo, H. Thienpont, K. Panajotov, "Investigation of polarization properties of VCSELs subject to optical feedback from an extremely short external cavity", in *Micro-Optics, VCSELs, and Photonic Interconnects II: Fabrication, Packaging, and Integration*, H. Thienpont, M.R. Taghizadeh, P. Van Daele, J. Mohr (Eds.), Proc. SPIE 6185, pp. 61850Z-1–9, 2006.

[25] M. Arizaleta Arteaga, H.J. Unold, J.M. Ostermann, R. Michalzik, H. Thienpont, and K. Panajotov, "Investigation of polarization properties of VCSELs subject to optical feedback from an extremely short external cavity—part I: theoretical analysis", *IEEE J. Quantum Electron.*, vol. 42, no. 2, pp. 89–101, 2006.

[26] M. Arizaleta Arteaga, H.J. Unold, J.M. Ostermann, R. Michalzik, H. Thienpont, and K. Panajotov, "Investigation of polarization properties of VCSELs subject to optical feedback from an extremely short external cavity—part II: experiments", *IEEE J. Quantum Electron.*, vol. 42, no. 2, pp. 102–107, 2006.

[27] M. Feneberg, F. Lipski, R. Sauer, K. Thonke, T. Wunderer, B. Neubert, P. Brückner, and F. Scholz, "Piezoelectric fields in GaInN/GaN quantum wells on different crystal facets", *Appl. Phys. Lett.*, vol. 89, pp. 242112-1–3, 2006.

[28] M. Feneberg, M. Schirra, B. Neubert, P. Brückner, F. Scholz, R. Sauer, and K. Thonke, "Spatially resolved cathodoluminescence, photoluminescence, electroluminescence, and reflectance study of GaInN quantum wells on non-(0001) GaN facets", *phys. stat. sol. (b)*, vol. 243, no. 7, pp. 1619–1624, 2006.

[29] E. Müller, D. Gerthsen, P. Brückner, F. Scholz, Th. Gruber, and A. Waag, "Probing the electrostatic potential of charged dislocations in n-GaN and n-ZnO epilayers by transmission electron holography", *Phys. Rev. B*, vol. 73, no. 24, pp. 245316-1–9, 2006.

[30] G.M. Prinz, A. Ladenburger, M. Feneberg, M. Schirra, S.B. Thapa, M. Bickermann, B.M. Epelbaum, F. Scholz, K. Thonke, and R. Sauer, "Photoluminescence, cathodoluminescence, and reflectance study of AlN layers and AlN single crystals", *Superlattices and Microstructures*, vol. 40, no. 4–6, pp. 513–518, 2006.

[31] A.A. Sirenko, A. Kazimirov, S. Cornaby, D.H. Bilderback, B. Neubert, P. Brückner, F. Scholz, V. Shneidman, and A. Ougazzaden, "Microbeam high angular resolution x-ray diffraction in InGaN/GaN selective-area-grown ridge structures", *Appl. Phys. Lett.*, vol. 89, pp. 181926-1–3, 2006.

[32] J. Wöllenstein, M. Braun, H. Böttner, S. Hartwig, A. Lambrecht, A. Peter, J. Ostermann, F. Rinaldi, and R. Michalzik, "On oxygen spectroscopy using surface-emitting lasers", (in German: "Zur Sauerstoffspektroskopie mit oberflächenemittierenden Lasern"), in Proc. *Sensoren und Messsysteme 2006, 13. ITG-/GMA-Fachtagung*, pp. 503–506. Freiburg, Germany, Mar. 2006.

Ulm University | Institute of Optoelectronics | Annual Report 2006

ulm university universität ulm

Ulm University
Institute of Optoelectronics
Albert-Einstein-Allee 45
89081 Ulm | Germany